A Thesis Submitted for the Degree of PhD at the University of Warwick

Permanent WRAP URL:

http://wrap.warwick.ac.uk/110215

Copyright and reuse:

This thesis is made available online and is protected by original copyright.

Please scroll down to view the document itself.

Please refer to the repository record for this item for information to help you to cite it.

Our policy information is available from the repository home page.

For more information, please contact the WRAP Team at: wrap@warwick.ac.uk
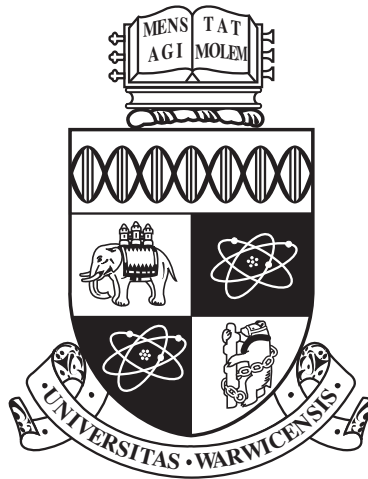
Rare events in optical fibers

by

Antonino Savojardo

Submitted to the University of Warwick for admission to

the degree of

Doctor of Philosophy

Department of Physics

September 2018

THE UNIVERSITY OF

WARWICK

Contents

Acknowledgments

Declarations

I declare that the content of this thesis is original work except where referenced within the text and has not been submitted as part of any other degree or qualification. Chapters 1 and 2 provide introductory information gathered from the literature as referenced.

Chapters 3, 4 , 5, 6 and 7 are based on the paper

- M. Eberhard, **A. Savojardo**, A. Maruta, and R. A. Römer, Rogue wave generation by inelastic quasi-soliton collisions in optical fibers, Optics Express 25 (23), 28086 (2017).

Results in chapter 8 are not published. Chapter 9 is based on the paper

- **A. Savojardo**, M. Eberhard, R. A. Römer, Dispersion map induced energy transfer between solitons in optical fibers, arXiv: 1710.07.15.

The entirety of the work was conducted under the supervision of Prof. Rudolf A. Römer and the content of the chapters highlighted above was performed in collaboration with the indicated authors.

Abstract

This thesis examines the topic of rogue waves and interacting quasi-solitons in optical fibers. We demonstrate a simple cascade mechanism that drives the formation and emergence of rogue waves in the generalized non-linear Schrödinger equation with third-order dispersion. Such generation mechanism is based on inelastic collisions of quasi-solitons and is well described by a resonant-like scattering behavior for the energy transfer in pair-wise quasi-soliton collisions. Our theoretical and numerical results demonstrate a threshold for rogue wave emergence and the existence of a period of reduced amplitudes — a "calm before the storm" — preceding the arrival of a rogue wave event. Using long time window simulations we observe the statistics of rogue waves in optical fibers with an unprecedented level of detail and accuracy, unambiguously establishing the long-ranged character of the rogue wave probability density function over seven orders of magnitude. The same cascade mechanism also generates rogue waves in the generalized non-linear Schrödinger equation with Raman term.

To comprehend the physics governing rogue wave formation, we propose an experimental setup where soliton amplification is induced without third order dispersion or Raman term. In an optical fiber with anomalous dispersion, we replace a small region of the fiber with a normal dispersion fiber. We show that solitons colliding in this region are able to exchange energy. Depending on the relative phase of the soliton pair, we find that the energy transfer can lead to an energy gain in excess of 20% for each collision. A sequence of such events can be used to enhance the energy gain even further, allowing the possibility of considerable soliton amplification.

Abbreviation

List of Figures

VI

Introduction

Figure 1: The Great Wave off Kanagawa. The painting depicts a rogue wave threatening boats off the coast of the town of Kanagawa. The image was painted by the Japanese artist Katsushika Hokusai between 1829 and 1833.

Optical "rogue" waves are rare and very high intensity pulses of light that occur in optical devices such as communication fibers [1–6]. They appear suddenly and can cause transmission errors and damage in optical communication systems [7]. Indeed, the physics governing their dynamics is very similar to "monster" or "freak" waves on the Earth's oceans, which are known to harm shipping [8–10]. This link between seemingly unconnected physical effects is not surprising when one recalls that the generalized nonlinear Schrödinger equation models the dynamics of waves propagat-

ing in optical fibers as well as in deep oceans [11–14]. Hence the physics of rogue waves is of fundamental as well as very applied interest. It is therefore important to characterize rogue wave generation, dynamics and, if possible, predictability [15]. Rogue waves are quantitatively described with the help of their probability density function [2, 5, 6]. This statistical curve generally has a typical "L-shaped" profile [2, 5, 6], characterizing the occurrence of many small events as well as, in the horizontal part of the "L", some very rare and extremely powerful events. Its statistical signature has been experimentally observed and numerically reproduced. However, what drives the formation of this "L"-shaped probability is not yet clear [16]. Possible mechanisms could be linear focusing of wave superpositions [17–21] and wave amplification due to inelastic scattering [22–25]. In this last scenario the largest solitons collide multiple times with the smaller ones increasing their energy in most of the cases. Such pulses will have accumulated most of the energy in the system and have become rogue waves.

In this thesis we want to ascertain quantitatively whether inelastic scattering is indeed sufficient to generate rogue waves of the required exceptionally high peak powers. We will propose an effective model for rogue wave formation where solitons are able to exchange energy during collision process. We will also suggest an experiment to clarify the physics underlining the collision-induced soliton energy transfer.

Chapter 1 gives an overview of the basic ideas necessary to understand how light propagates in nonlinear optical fibers. In chapter 2, we discuss some experimental and numerical results regarding rare events in optical systems. We will also see how the generalized nonlinear Schrödinger equation can describe optical rogue waves. Our first results on rogue wave statistics and dynamics are presented in chapter 3. Those results were obtained by a massive parallel simulation of nonlinear optical fibers. In chapter 4 we show that the generalized nonlinear Schrödinger equation has soliton-like solution and we introduce the quasi-soliton approximation. Chapter 5 shows that during a two quasi-soliton collision energy is transferred from one pulse to the other. An approximation is also proposed for the collision-induced energy gain. In chapter 6 and 7 we present a cascade model that produces rogue waves without the need to integrate the full generalized nonlinear Schrödinger equation. The model is based on the previews results found for quasi-soliton propagation and interaction in the nonlinear Schrödinger equation with third order dispersion. The Raman term is another important correction to the nonlinear Schrödinger equation, its role in rogue wave formation is explored in chapter 8. Here we show that the

cascade model can describe rogue waves also when the Raman term is considered. Finally, in chapter 9 we propose an experimental setup to study collision-induced soliton amplification. In this setup, energy transfer from one pulse to the other does not require a third order dispersion or Raman term. Such numerical experiment gives some insights on the physics governing rogue wave formation.

Part I Background

Chapter 1

Nonlinear fiber optics

This first introductory chapter provides an overview of the basic ideas necessary to understand how light propagates in nonlinear optical fibers. Section 1.1 introduces optical fibers and theirs properties. In section 1.2 we derive the basic equation that governs the propagation of optical pulses, the generalized nonlinear Schrödinger equation. Energy conservation for the optical field is discussed in section 1.3. In section 1.4 we explain how solitons can be generated experimentally. Finally, section 1.5 is devoted to the split-step Fourier method, the standard approach used to solve numerically the optical field propagation equation.

1.1 Optical fibers

Optical fibers are flexible and transparent cables made of glass or plastics. Their most common use is in optical communication to transmit signals of light over long distances. Optical fibers typically consists of a transparent core surrounded by a cladding layer. The core index of refraction n_1 is higher than the cladding index of refraction n_c because of this difference light is trapped in the core and fibers can be used as a waveguides. Figure 1.1 shows the cross-section and refractive-index profile for an optical fiber [26].

Light that travels inside an optical fiber consists of an electromagnetic field that oscillates in the plane perpendicular to the direction of propagation. A particular pattern of the electromagnetic field is called transverse mode. Fibers that support a single mode are called single-mode fibers (SMFs) whereas fibers that support multiple modes are called multi-mode fibers (MMFs). Single-mode fibers are usually cheaper and better at retaining the accuracy of light signals than multi-mode fibers. Indeed,
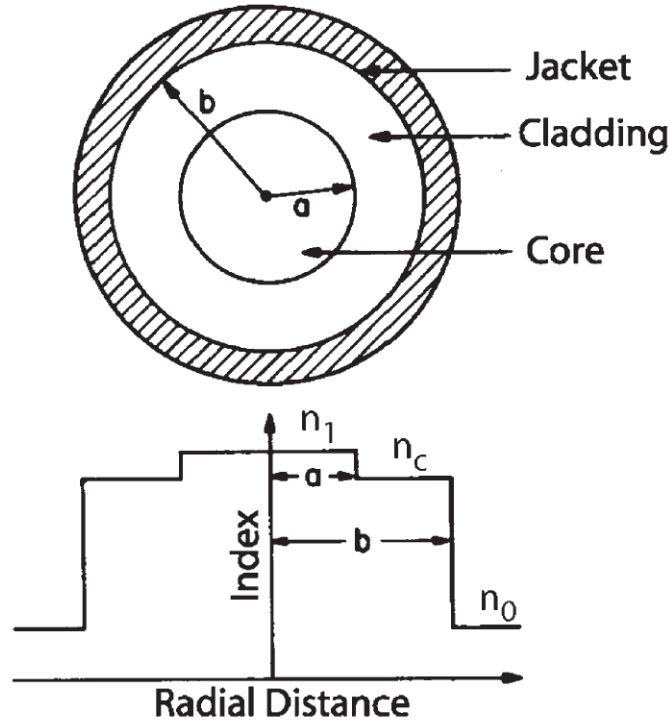
Figure 1.1: Cross-section and refractive-index profile for an optical fiber (image from [26]).

MMFs are reliable for communication lengths up to $\sim$ 600m while SMFs have an upper limit of $\sim$ 2Km [26]. For these reasons, SMFs are preferred to MMFs in optical communication. Given their more widespread application, we will use the term optical fiber to refer to a SMF.

1.2 Light propagation in optical fibers

In this section we introduce the generalized nonlinear Schrödinger equation which describes the propagation of optical pulses in nonlinear fibers.

1.2.1 Nonlinear effects in optical fibers

Some optical material properties respond non-linearly to intense electric fields. This produces optical effects that are not observed in linear devices [26]. Examples of such nonlinear effects are [26]

- Raman effect: a loss of energy exhibited by some of the photons scattered in

a nonlinear medium. The effect depends on the molecules that cause it, and therefore can be used in spectroscopic analysis.

- Frequency doubling: a process in which two photons with the same frequency are combined to generate a new photon with twice the frequency of the initial ones.

- Kerr effect: a change in the refractive index of a material in response to an applied electric field. The difference in index of refraction, is given by $\triangle n = \lambda K |E|^2$ where λ is the wavelength of the light, K is the Kerr constant, and E is the electric field. The effect allows to control the amount of light transmitted through a nonlinear material, therefore can be used to build optical switches.

Nonlinear effects in optical fibers can be explained using the Maxwell's equations [26]

$$\nabla \times \bar{E} = -\frac{\partial \bar{B}}{\partial t}, \tag{1.1a}$$

$$\nabla \times \bar{H} = \bar{J} + \frac{\partial \bar{D}}{\partial t}, \tag{1.1b}$$

$$\nabla \cdot \bar{D} = \rho_f, \tag{1.1c}$$

$$\nabla \cdot \bar{B} = 0, \tag{1.1d}$$

where $\bar{E}$ and $\bar{H}$ are the electric and magnetic field vectors, $\bar{D}$ and $\bar{B}$ are the electric and magnetic flux densities, $\bar{J}$ is the current density vector and ρ_f is the free charge density. The flux densities $\bar{D}$ and $\bar{B}$ are related to the electric and magnetic fields through the relations

$$\bar{D} = \epsilon_0 \bar{E} + \bar{P}, \tag{1.2a}$$

$$\bar{B} = \mu_0 \bar{H} + \bar{M}, \tag{1.2b}$$

where ϵ_0 is the vacuum permittivity, μ_0 is the vacuum permeability, and $\bar{P}$ and $\bar{M}$ are the electric and magnetic polarizations. The wave equation that describes light propagation can be obtained considering that in an optical fiber $\bar{J} = 0$, $\bar{M} = 0$ and $\rho_f = 0$. The Maxwell's equations under such conditions yield to the wave equation

$$\nabla^2 \bar{E} - \frac{1}{c^2} \frac{\partial^2 \bar{E}}{\partial t^2} = \mu_0 \frac{\partial^2 \bar{P}}{\partial t^2}, \tag{1.3}$$

where c is the speed of light given by the relation $c^2 = 1/\mu_0 \epsilon_0$. The properties of a medium are described by the polarization vector $\bar{P}$. In an optical fiber $\bar{P}$ responds non-linearly to an electric field $\bar{E}$, and can be written as a sum of two terms [26]

$$\bar{P} = \bar{P}_L + \bar{P}_{NL}, \tag{1.4}$$

where

$$\bar{P}_L(\bar{r}, t) = \epsilon_0 \int_{-\infty}^{t} \chi_L(t - t') \bar{E}(\bar{r}, t') dt' \tag{1.5}$$

is the linear part, and

$$\bar{P}_{NL}(\bar{r}, t) = \epsilon_0 K_{NL} \bar{E}(\bar{r}, t) \int_{-\infty}^{t} R(t - t') \left| \bar{E}(\bar{r}, t) \right|^2 dt' \tag{1.6}$$

is the nonlinear part of the polarization vector. In the two equations above, χ_L is the linear susceptibility, K_{NL} is a constant that depends on the material and $R(t)$ is the nonlinear response function, normalized such that $\int_{-\infty}^{+\infty} R(t) dt = 1$. In Eq. (1.6) only the nonlinear correction up to the third order in the electric field has been considered. For highly nonlinear fibers higher order terms need to be taken into account [26].

The system of equations (1.3, 1.4, 1.5, 1.6) is not easy to handle because it is nonlinear and contains both integrals ad derivatives of the electric field. To have a model treatable analytically and numerically it is necessary to make several simplifying approximations.

1.2.2 Generalized nonlinear Schrödinger equation

The generalized nonlinear Schrödinger equation (gNLSE) is an approximation for Eqs. (1.3, 1.4, 1.5, 1.6) that allows to describe pulses of light inside an optical fibers. The gNLSE can be derived under the assumptions [26]

1. Light propagates along the z direction and the electric field has a constant polarization along the x direction.

2. The electric field is quasi-monochromatic, i.e., the spectral width $\triangle\omega$ is much smaller that the carried frequency ω_0.

3. For the previous two assumptions and the cylindrical symmetry of fibers, the electric field can be written as

$$\bar{E}(\bar{r}, t) = \hat{x} F(x, y) u(z, t) e^{i\beta_0 z - i\omega_0 t}, \tag{1.7}$$

where β_0 is the carried wave number and $u(z, t)$ is the pulse envelope (or optical field), which describes the variation of the electric field along the z direction and the time t. $F(x, y)$ describes the variation of the electric field along the x and y directions and it is usually approximated by a Gaussian distribution

$$F(x, y) \simeq \exp[-(x^2 + y^2)/w^2], \tag{1.8}$$

where the width parameter w is determined experimentally.

4. P_{NL} is a small perturbation to P_L , i.e.

$$P_{NL} \ll P_L. \tag{1.9}$$

5. The linear part of the dispersion $\beta_L(\omega)$ can be expanded in a Taylor series around the carrier frequency ω_0 as

$$\beta_L(\omega) = \frac{n_L(\omega)\omega}{c} = \beta_0 + \beta_1(\omega - \omega_0) + \frac{1}{2}\beta_2(\omega - \omega_0)^2 + \frac{1}{6}\beta_3(\omega - \omega_0)^3 + \dots \tag{1.10}$$

where

$$n_L(\omega) = \sqrt{1 + \text{Re}[\chi_L(\omega)]} \tag{1.11}$$

is the linear part of the refractive index.

6. The loss $\alpha(\omega)$ can be expanded in a Taylor series around the carrier frequency ω_0 as

$$\alpha(\omega) = \frac{\omega}{n_L(\omega)c}\text{Im}[\chi_L(\omega)] = \alpha_0 + \alpha_1(\omega - \omega_0) + \dots \quad . \tag{1.12}$$

7. The nonlinear term γ, defined as

$$\gamma(\omega) = \frac{K_{NL}}{2n_L(\omega)}\frac{\omega}{c}\frac{\int\int_{-\infty}^{\infty}|F(x, y)|^4 dx dy}{\int\int_{-\infty}^{\infty}|F(x, y)|^2 dx dy}, \tag{1.13}$$

9

can also be expanded around the carrier frequency ω_0

$$\gamma(\omega) = \gamma_0 + \gamma_1(\omega - \omega_0) + \ldots \quad . \tag{1.14}$$

8. $u(z,t)$ is assumed to be a slowly varying function of z, i.e., the second derivative $\partial^2 u/\partial^2 z$ is neglected under the assumption

$$\left| \frac{\partial^2 u}{\partial z^2} \right| \ll \left| \beta_0 \frac{\partial u}{\partial z} \right|. \tag{1.15}$$

As we will see later a pulse with power P has wave number $k \sim \frac{\gamma_0 P}{2}$ and amplitude $\sqrt{P}$, thus $\frac{\partial u}{\partial z} \sim \sqrt{P}\frac{\gamma_0 P}{2}$ and $\frac{\partial^2 u}{\partial z^2} \sim \sqrt{P}\left(\frac{\gamma_0 P}{2}\right)^2$. Therefore the above condition is equivalent to $\frac{\gamma_0 P}{2} \ll \beta_0$. Typical values for the nonlinear term and the carried wave number in optical communication fibers are [26] $\gamma_0 \sim 0.01 \text{ W}^{-1}\text{m}^{-1}$ and $\beta_0 \sim \frac{2\pi}{\lambda_0} = 2\pi \cdot 10^6 \text{m}^{-1}$, where λ_0 is the carried wave length. With these numbers approximation (1.15) is valid for powers $P \ll 4\pi \cdot 10^8 \text{W}$.

Using Eqs. (1.3, 1.4, 1.5, 1.6) and the above assumptions we can derive the generalized nonlinear Schrödinger equation for the pulse envelope $u(z,t)$ to be

$$\begin{aligned} \frac{\partial u}{\partial z} + \frac{1}{2}\left(\alpha_0 + i\alpha_1 \frac{\partial}{\partial t}\right)u - i\sum_{n=1}^{\infty} \frac{i^n \beta_n}{n!}\frac{\partial^n u}{\partial t^n} &= \\ i\left(\gamma_0 + i\gamma_1 \frac{\partial}{\partial t}\right)\left(u(z,t)\int_0^{\infty} R(t')\left|u(z,t-t')\right|^2 dt'\right)&. \end{aligned} \tag{1.16}$$

1.2.3 Generalized nonlinear Schrödinger equation for wide pulses

For pulses that last more than $100\,\text{fs}$ the nonlinear response $R(t)$ of the medium can be considered almost instantaneous [26]. In the integral part of Eq. (1.16), we can therefore use the approximation

$$|u(z,t-t')|^2 \approx |u(z,t)|^2 - t'\frac{\partial |u(z,t)|^2}{\partial t}. \tag{1.17}$$

From experimental measurements we also have $\alpha_1 \approx 0$ and $\gamma_1 \approx \gamma_0/\omega_0$ [26]. Thus Eq. (1.16) can be simplified as

$$\frac{\partial u}{\partial z} + \frac{\alpha}{2}u + i\frac{\beta_2}{2}\frac{\partial^2 u}{\partial t^2} - \frac{\beta_3}{6}\frac{\partial^3 u}{\partial t^3} = i\gamma\left(|u|^2 u + \frac{i}{\omega_0}\frac{\partial}{\partial t}(|u|^2 u) - T_R u\frac{\partial|u|^2}{\partial t}\right), \qquad (1.18)$$

where we have dropped the subscript 0 for the parameters α and γ. To derive Eq. (1.18) we used the transformation $t \to t - \beta_1 z$ and therefore the time variable t is measured in the frame of reference moving with the pulse group velocity (the group velocity is $v_g = \left(\frac{d\beta}{d\omega}\right)^{-1}_{\omega=\omega_0} = \frac{1}{\beta_1}$). The Raman term T_R is defined as

$$T_R = \int_0^\infty R(t)\, t\, dt, \qquad (1.19)$$

and it is responsible for a pulse self-frequency shift, a linear change of the pulse frequency with the propagation distance [27]. The parameter β_3 in Eq. (1.18) is called third order dispersion (TOD) term. Its main effect is to induce a pulse to radiate energy [28]. The term $1/\omega_0$ is responsible for the phenomenon of self-steepening, an asymmetry in the pulse shape [29]. The term α causes a pulse to lose energy in form of heat. The transmitted power over a distance z is approximately $P_T = P_I e^{-\alpha z}$ [26], where P_I is the input power.

The parameters in Eq. (1.18) depend on the type of optical fiber, typical values for optical communication fibers are [26] $\alpha \sim 10^{-4}-10^{-3}\text{m}^{-1}$, $\beta_2 \sim \pm\left(10^{-4} - 10^{-2}\right)\text{ps}^2\text{m}^{-1}$, $\beta_3 \sim 10^{-6} - 10^{-4}\text{ps}^3\text{m}^{-1}$, $\gamma \sim 10^{-3} - 10^{-2}\text{W}^{-1}\text{m}^{-1}$, $\omega_0 \sim 10^3\text{THz}$ and $T_R \sim 10^{-4} - 10^{-3}\text{ps}$.

1.2.4 Nonlinear Schrödinger equation and solitons

The Raman term, self-steepening and TOD can be neglected for pulses of width $T \gg T_R$, $1/\omega_0$ and $|\beta_3/\beta_2|$. Considering propagation distances of few hundred meters the loss α can also be disregarded. Under such conditions Eq. (1.18) is further simplified as

$$\frac{\partial u}{\partial z} + i\frac{\beta_2}{2}\frac{\partial^2 u}{\partial t^2} = i\gamma|u|^2 u. \qquad (1.20)$$

Eq. (1.20) is called the nonlinear Schrödinger equation (NLSE), and can be solved analytically [30, 31] for a single pulse if the intensity goes to a constant value (zero or a finite number) for $t \to \pm\infty$. The solution depends on the sign of β_2. For $\beta_2 < 0$

we have bright-solitons with pulse envelope

$$u(z,t) = \sqrt{P}\,\text{sech}\left[\frac{t - v^{-1}z}{T}\right]\exp\left[i\left(\frac{\beta_2}{2}\Omega^2 + \frac{\gamma P}{2}\right)z - i\Omega t\right], \qquad (1.21a)$$

whereas for $\beta_2 > 0$ we have dark-solitons with pulse envelope

$$u(z,t) = \sqrt{P}\tanh\left[\frac{t - v^{-1}z}{T}\right]\exp\left[i\left(\frac{\beta_2}{2}\Omega^2 + \gamma P\right)z - i\Omega t\right]. \qquad (1.21b)$$

The term $T = \sqrt{|\beta_2|/\gamma P}$ is the pulse width, P is the peak power, $v^{-1} = \beta_2\Omega$ is the inverse of the pulse velocity and Ω is the frequency shift. In Fig. 1.2 we show the intensities $|u|^2$ corresponding to Eq. (1.21a) and Eq. (1.21b), as function of the variable $t' = t - v^{-1}z$. As we can see the two solutions behave differently. Around $t' = 0$ a bright soliton has a localized increase of intensity while a dark soliton has a localized reduction of intensity compared to the background. A bright soliton can be seen as a peak of light whereas a dark soliton is a pulse of "darkness" within a continuous wave.

The soliton solutions Eq. (1.21a) and Eq. (1.21b) can be found solving Eq. (1.20) in the following way. We write the optical field as

$$u(z,t) = \psi(t - \beta_2\Omega z)\exp\left[iKz - i\Omega t\right], \qquad (1.22)$$

where ψ is a real function and K is a constant. Then, we insert Eq. (1.22) into Eq. (1.20) and get the equation

$$\frac{\beta_2}{2}\frac{d^2\psi}{d\xi^2} + \left(K - \frac{\beta_2}{2}\Omega^2\right)\psi - \gamma\psi^3 = 0, \qquad (1.23)$$

where the new variable ξ is defined as $\xi = t - \beta_2\Omega z$. Integrating Eq. (1.23) in ψ and using the relation $\int\frac{d^2\psi}{d\xi^2}d\psi = \frac{1}{2}\left(\frac{d\psi}{d\xi}\right)^2$, we get the differential equation

$$\frac{\beta_2}{2}\left(\frac{d\psi}{d\xi}\right)^2 + \left(K - \frac{\beta_2}{2}\Omega^2\right)\psi^2 - \frac{\gamma}{2}\psi^4 = 0, \qquad (1.24)$$

which can be written in the integral form
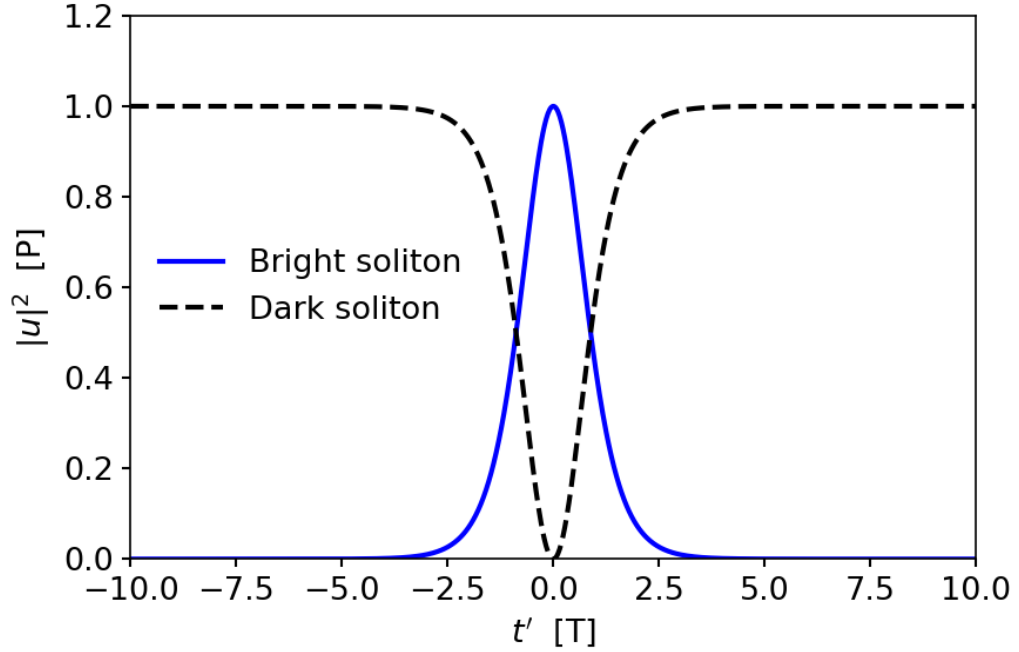
Figure 1.2: Intensity $|u(t')|^2$ as function of the time $t' = t - v^{-1}z$ for a bright soliton (full blue line) and a dark soliton (dashed black line) corresponding to Eq. (1.21a) and Eq. (1.21b) respectively. The intensity is represented in peak power unit P, and the time in pulse width unit T.

$$\xi = \int \frac{d\psi}{\sqrt{\frac{\gamma\psi^4 - (2K - \beta_2\Omega^2)\psi^2}{\beta_2}}} = \begin{cases} T \operatorname{sech}^{-1}\left(\frac{\psi}{\sqrt{P}}\right) & \text{for } \beta_2 < 0 \\ T \tanh^{-1}\left(\frac{\psi}{\sqrt{P}}\right) & \text{for } \beta_2 > 0 \end{cases}. \tag{1.25}$$

Inverting Eq. (1.25) we have a bright-soliton solution for $\beta_2 < 0$, otherwise, for $\beta_2 > 0$ we get a dark-soliton.

Generally, solitons are defined as localized waves that travel in space or time without changing their shape [26, 32]. In the literature [26, 32] the term "soliton", without any further connotation, refers to bright-solitons. In this manuscript we will use the same convention.

1.3 Energy conservation

The energy of the optical field $u(z, t)$ is defined as

$$E(z) = \int\limits_{-\infty}^{+\infty} |u(z,t)|^2 dt \tag{1.26}$$

and it is a conserved quantity for both Eq. (1.18) and Eq. (1.20). Thus $\partial E / \partial z = 0$ at every point z. The energy conservation can be easily proved for the NLSE. We start differentiating the intensity $|u(z,t)|^2$ with respect to the space variable z

$$\frac{\partial |u|^2}{\partial z} = u^* \frac{\partial u}{\partial z} + u \frac{\partial u^*}{\partial z}, \tag{1.27}$$

using Eq. (1.20) and its complex conjugated we obtain

$$\frac{\partial |u|^2}{\partial z} = -i \frac{\beta_2}{2} \left(u^* \frac{\partial^2 u}{\partial t^2} - u \frac{\partial^2 u^*}{\partial t^2} \right) = -i \frac{\beta_2}{2} \frac{\partial}{\partial t} \left(u^* \frac{\partial u}{\partial t} - u \frac{\partial u^*}{\partial t} \right). \tag{1.28}$$

Integrating in the time variable we get

$$\frac{\partial E}{\partial z} = \int\limits_{-\infty}^{+\infty} \frac{\partial |u|^2}{\partial z} dt = -i \frac{\beta_2}{2} \left[u^* \frac{\partial u}{\partial t} - u \frac{\partial u^*}{\partial t} \right]_{-\infty}^{+\infty} = 0, \tag{1.29}$$

where we have used the fact that for $t \to \pm\infty$ we expect the optical field to be constant and therefore $\partial u / \partial t = \partial u^* / \partial t = 0$.

For a single bright-soliton described by Eq. (1.21a) the energy can be calculated analytically and its value is $E = 2PT$. When multiple pulses are present in an optical fiber, we can define the energy E_i of pulse i, integrating the intensity in an interval $[t_i - \tau, t_i + \tau]$

$$E_i = \int\limits_{t_i-\tau}^{t_i+\tau} |u(z,t)|^2 dt, \tag{1.30}$$

where t_i is the time corresponding to peak power of pulse i and τ is typically chosen larger than $3T$. The total energy of the optical field defined in Eq. (1.26) is always conserved, whereas, the one pulse energy defined in Eq. (1.30) can change with z, for example when a pulse radiates energy because of a perturbation to Eq. (1.20). Solitons do not radiate dispersive waves or exchange energy with others solitons, i.e., solitons are stable pulses and always collide elastically [26]. As we will see in the later chapters there are soliton-like pulses, called quasi-solitons, that can have

inelastic collisions and energy is transferred from on pulse to another [22–25].

1.4   Soliton generation

Optical solitons have not only been predicted analytically but also observed experimentally [33] and used for optical communication [34]. From practical point of view, a single soliton can be created using a semiconductor laser that converts an electric signal into a light signal [34]. Once the pulse of light is generated it can be launched into an optical fiber.

A train of solitons can be produced using the so called modulation instability effect [34]. In the process a continuous-wave radiation of light plus a small noise are launched into a nonlinear fiber with anomalous dispersion ($\beta_2 < 0$). After a certain distance the optical field is spontaneously modulated and bright solitons are created. Supercontinuum generation is the effect of modulation instability observed in the frequency domain. It consists in a broadening of the intensity spectrum from an initial narrow-band input wave [35, 36]. Note that modulation instability is theoretically predicted for a system extended on an infinite time window, but in practice it is also observed in systems with finite time window [34].

Modulation instability and supercontinuum generation are both important in the early stages of rogue wave generation [2, 5, 6]. Theirs effect on rogue wave formation will be discussed in more details in chapters 2 and 3.

1.5   Split-Step Fourier Method

The gNLSE can be solved analytically only in some specific cases, when this is not possible numerical methods are used instead. A common numerical technique utilized to solve Eq. (1.18) is the split-step Fourier method [26, 37–39]. To understand the method we need to rewrite (1.18) in the form

$$\frac{\partial u}{\partial z} = \left(\hat{L} + \hat{N} \right) u, \qquad (1.31)$$

where $\hat{L}$ and $\hat{N}$ are the linear and nonlinear operators defined as

$$\hat{L} = -\frac{\alpha}{2} - i\frac{\beta_2}{2}\frac{\partial^2}{\partial t^2} + \frac{\beta_3}{6}\frac{\partial^3}{\partial t^3}, \qquad (1.32)$$

$$\hat{N} = i\gamma \left(|u|^2 + \frac{i}{\omega_0 u} \frac{\partial}{\partial t} (|u|^2 u) - T_R \frac{\partial |u|^2}{\partial t} \right). \qquad (1.33)$$

When the optical field $u(z,t)$ propagates for a small distance h the exact solution of Eq. (1.31) is given by

$$u(z+h,t) = \exp\left[\left(\hat{L} + \hat{N} \right) h \right] u(z,t). \qquad (1.34)$$

In the split-step Fourier method the previous equation is approximated with

$$u(z+h,t) \simeq \exp\left(\hat{L}h \right) \exp\left(\hat{N}h \right) u(z,t), \qquad (1.35)$$

i.e., the linear and nonlinear operators are assumed to act independently on $u(z,t)$. Eq. (1.35) can be numerically solved applying the fast Fourier transform to the optical field. The split-step Fourier method solution is

$$u(z+h,t) = \hat{F}^{-1} \left\{ \exp\left(\hat{L}(\omega)h \right) \hat{F} \left[\exp\left(\hat{N}h \right) u(z,t) \right] \right\}, \qquad (1.36)$$

where

$$\hat{L}(\omega) = -\frac{\alpha}{2} + i\frac{\beta_2}{2}\omega^2 + i\frac{\beta_3}{6}\omega^3 \qquad (1.37)$$

is the Fourier transform of the linear operator (1.32), while $\hat{F}$ and $\hat{F}^{-1}$ are the fast Fourier transform operator and its inverse. Note that the nonlinear operator $\hat{N}$ is an ordinary complex function therefore can be directly applied to the optical field without further transformations. In comparison to the discrete Fourier transform, the fast Fourier transform has the advantage of reducing the number of operations to calculate n Fourier coefficients from order n^2 to order $n\ln(n)$.

To estimate the error committed when we factorize Eq. (1.34) we need to look at the Baker-Campbell-Hausdorff formula for two non-commuting operators

$$\exp\left(\hat{L}h \right) \exp\left(\hat{N}h \right) = \exp\left[\hat{L}h + \hat{N}h + \frac{1}{2}(\hat{L}\hat{N} - \hat{N}\hat{L})h^2 + O(h^3) \right]. \qquad (1.38)$$

Eq. (1.38) shows that the split-step Fourier method is accurate to the order h^2. The typical length scale for a pulse of power P is $(\gamma P)^{-1}$ thus convergence is guarantied choosing $h \ll (\gamma P)^{-1}$, usually h is taken in the range $10^{-4} - 10^{-3}(\gamma P)^{-1}$ [26, 40]. Note that the use of the fast Fourier transform imposes periodic boundary conditions

on the optical field, hence to guaranty numerical stability, the temporal window has to be chosen at least 10 times the pulse width [26]. Selecting the appropriate time window and step, the fast Fourier transform algorithm makes the split-step Fourier method up to two orders of magnitude faster than most finite-difference approaches [41]. For this reason, the method is considered the standard scheme to find numerical solutions of the gNLSE. The numerical results presented in this manuscript, that involve the use of the gNLSE, have been obtained using the split-step Fourier method.

Summary

In this chapter, we introduced optical fibers and the concepts and tools that we are going to use in the next chapters. The main points of the chapter are:

- Optical fibers are flexible and transparent cables made of glass or plastics used to transmit signals of light over long distances. The response of an optical fiber becomes nonlinear for intense electric fields.

- The propagation of optical pulses in a nonlinear fibers is described by the generalized nonlinear Schrödinger equation (gNLSE). For wide pulses such equation is given by

$$\frac{\partial u}{\partial z} + \frac{\alpha}{2}u + i\frac{\beta_2}{2}\frac{\partial^2 u}{\partial t^2} - \frac{\beta_3}{6}\frac{\partial^3 u}{\partial t^3} = i\gamma\left(|u|^2 u + \frac{i}{\omega_0}\frac{\partial}{\partial t}(|u|^2 u) - T_R u\frac{\partial |u|^2}{\partial t}\right).$$

- For pulses of width larger than 5ps and propagation distances of few kilometers, the gNLSE is simplified into the nonlinear Schrödinger equation (NLSE)

$$\frac{\partial u}{\partial z} + i\frac{\beta_2}{2}\frac{\partial^2 u}{\partial t^2} = i\gamma|u|^2 u.$$

- Solitons are defined as localized waves that travel in space or time without changing their shape. The NLSE equation has bright and dark soliton solutions given respectively by

$$u(z,t) = \sqrt{P}\,\mathrm{sech}\left[\frac{t - v^{-1}z}{T}\right]\exp\left[i\left(\frac{\beta_2}{2}\Omega^2 + \frac{\gamma P}{2}\right)z - i\Omega t\right]$$

and

$$u(z,t) = \sqrt{P}\tanh\left[\frac{t - v^{-1}z}{T}\right]\exp\left[i\left(\frac{\beta_2}{2}\Omega^2 + \gamma P\right)z - i\Omega t\right].$$

17

- In the gNLSE equation the total energy, defined as

$$E = \int\limits_{-\infty}^{+\infty} |u(z,t)|^2 dt,$$

   is conserved along z. A single pulse energy is not always conserved.

- The gNLSE can be solved numerically using the split-step Fourier method, the solution is

$$u(z+h,t) = \hat{F}^{-1} \left\{ \exp\left(\hat{L}(\omega)h\right) \hat{F} \left[\exp\left(\hat{N}h\right) u(z,t) \right] \right\}.$$

In the following chapter, we will discuss the concept of rogue waves in optical fibers, the main object of this work.

Chapter 2

Rogue waves in optical fibers

In this second introductory chapter, we discuss some experimental and numerical results gathered from the literature regarding rare events in optical systems. Section 2.1 introduces rogue waves. In section 2.2 we examine experimental results by Solli et al. [42] on optical rogue waves. Finally, section 2.3 considers numerical results by Taki et al. [43] on extreme events generated when the third-order dispersion term is added to the NLSE.

2.1   Introduction to rogue waves

Historically, reports of "monster" or "freak" waves [8–10] on the Earth's oceans have been seen largely as sea men's tales [44, 45]. However, the recent availability of reliable experimental observations [44, 46–49] has proved their existence and shown that these "rogues" are indeed rare events [50], governed by long tails in their probability density function [51], and hence associated with very large wave amplitudes [14, 52]. Optical rogue waves are the optical analog of oceanic rogue waves, they are rare and very high intensity pulses of light that occur in optical devices such as communication fibers. They appear suddenly and can cause transmission errors and damage in optical communication systems [7]. It is therefore important to characterize rogue wave generation, dynamics and, if possible, predictability. As both deep water waves in the oceans and optical waves in fibers can be described by similar generalized non-linear Schrödinger equations [11–14] they both show rogue waves (RWs) and long-tail statistics [51, 53, 54]. The case of RW generation in optical fibers during super-continuum generation has been observed experimentally [42, 55–61] and numerically [1, 43, 62–69].
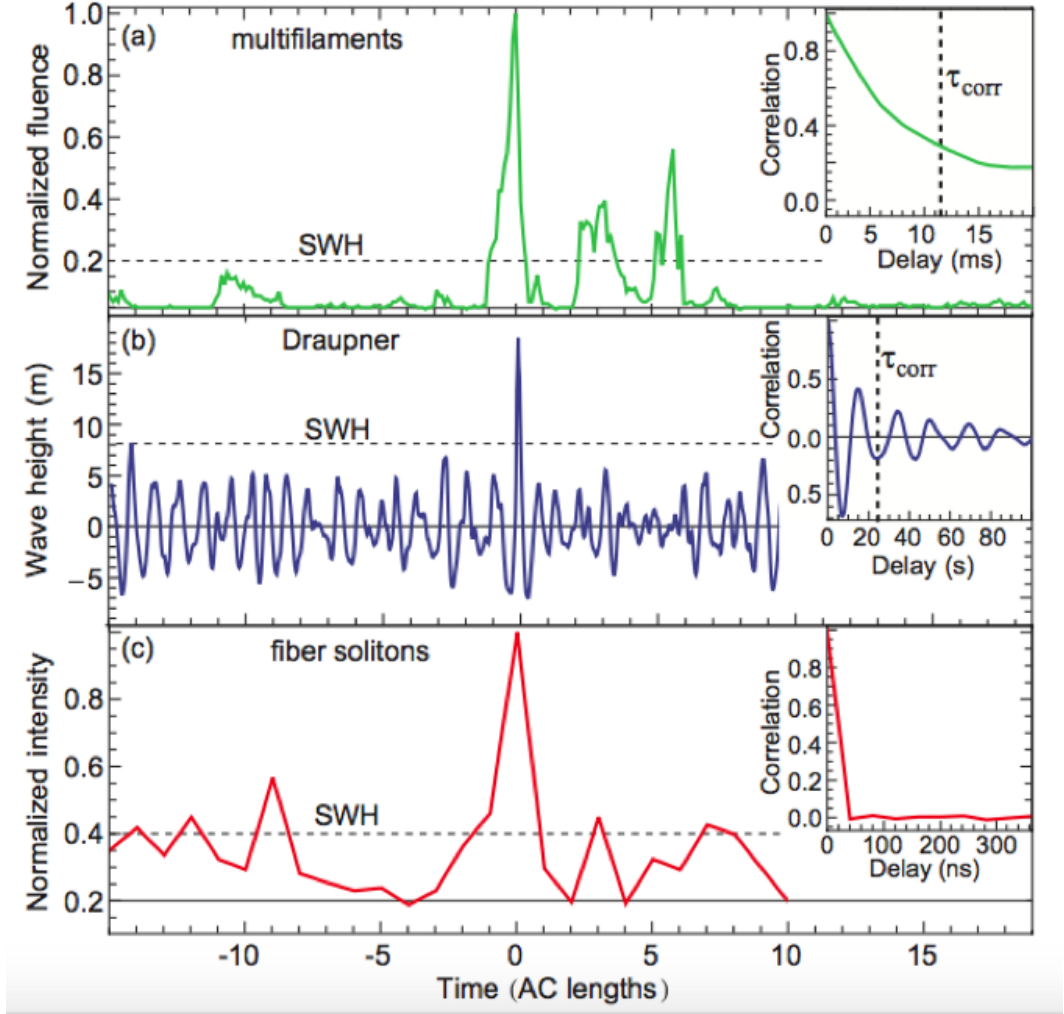
Figure 2.1: Examples of rogue events (a) in multifilament dynamics, (b) the oceanographic context (Draupner data set), and (c) soliton dynamics in a nonlinear fiber. Abscissae in (a) and (b) have been rescaled to equal units in terms of autocorrelation width. Solid lines: long-term averages. Dashed horizontal lines: significant wave height (SWH) (image from [15]).

Recently, experimental data of long tails in the probability density function (PDF) have been collected [42, 70, 71], as well as intensities and time correlations in various wave phenomena with RW occurrence [15]. RWs and long-tailed PDFs have also been found during high power femtosecond pulse filamentation in air [72], in non-linear optical cavities [73] and in the output intensity of optically injected semiconductors laser [74], mode-locked fiber lasers [75, 76], Raman fiber lasers [77] and fiber Raman amplifiers [7]. Fig. 2.1 shows real data intensities and time correlations [15] for three

different systems (a) a multiple filamentation in a gas cell, (b) ocean waves recorded on the Draupner oil platform and (c) a nonlinear optical fiber. In the figure SWH indicates the significant wave height defined as the average of the largest third of waves in a record. Although the correlation time differ from system to system, in all three cases we can find events that exceed the SWH. There is not agreement on how to define exactly a rogue wave. One possibility is to considered a wave rogue when its height is more than twice the SWH [15]. Another possibility is to call rogue only events that are observed on the long tail part of the PDF [5, 78].

Independently of the exact definition, rogue waves appear to be a real phenomenon. Despite the experimental evidence, it still remains largely unknown how they emerge [5, 79, 80] and theoretical explanations range from high-lighting the importance of the non-linearity [52, 81–83] to those based on short-lived linear superpositions of quasi-solitons during collisions [17, 18].

2.2 Experimental results for optical rogue waves

Optical rogue waves are created in supercontinuum generation, a nonlinear effect in which a broad spectrum is developed from a narrow-band input wave [35, 36]. In the process a continuous-wave radiation of light is launched into a nonlinear fiber with anomalous dispersion ($\beta_2 < 0$). After a broadening of the spectrum the optical field is spontaneously modulated and solitons are created.

Rogue waves in a nonlinear optical fibers were observed for the first time in 2007 by Solli et al. [42]. In the experiment, pulses created during supercontinuum generation gave rise to the L-shaped statistics. The histograms of the intensity showed heavy-tailed statistics with rogue events reaching intensities of 30–40 times the average value. Fig. 2.2 shows intensities and associated histograms for a time window containing roughly 15000 pulses [42]. The plot includes results for three different average power levels of 0.8 mW, 3.2 mW and 12.8 mW. In the experiment a real-time digital oscilloscope was used to measure a large number of events in a single shot, this allowed to characterize rogue waves. The measurements highlighted three results:

1. Large intensity values occur rarely, yet more frequently than expected from an exponential statistics, that is, rogue wave statistics is sub-exponential (L-shaped PDF).
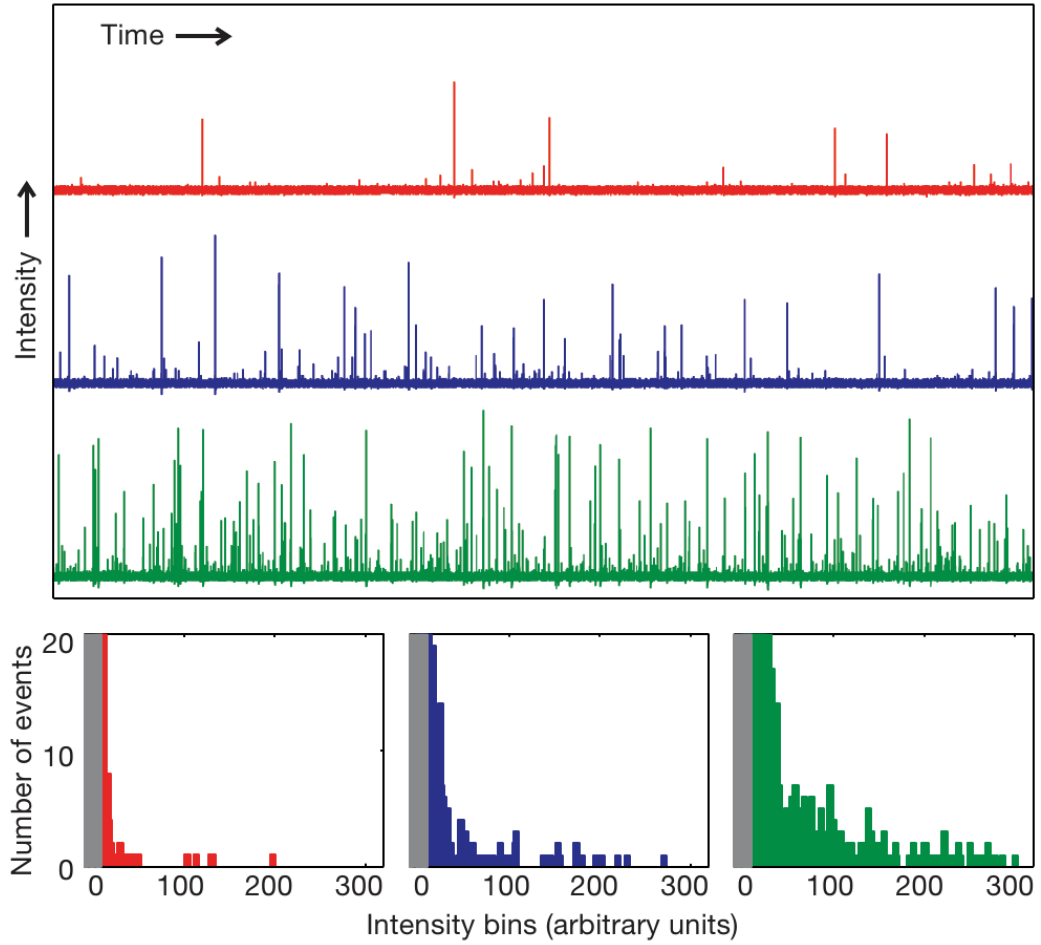
Figure 2.2: Intensities for a time window containing roughly 15000 pulses and associated "L" shaped histograms for average power levels 0.8 mW (red), 3.2 mW (blue) and 12.8 mW (green) (image from [42]).

2. The fraction of rare events can be increased by raising the power of the input wave.

3. Rogue waves are rare, high power, soliton-like pulses.

Since optical rogue waves are real events that occur in communication fibers, a theoretical description has both practical an fundamental interest. Considering that the generalized nonlinear Schrödinger equation describes pulses in nonlinear optical fibers, it make sense to use this equation to model optical rogue waves [84]. Note that for the standard NLSE the PDF of $|u|$ is a Rayleigh distribution and therefore the PDF of the intensity $|u|^2$ is exponential [14], that is why the NLSE without extra

terms is not sufficient to describe rogue waves. In the next sections we will discuss numerical results obtained solving the gNLSE.
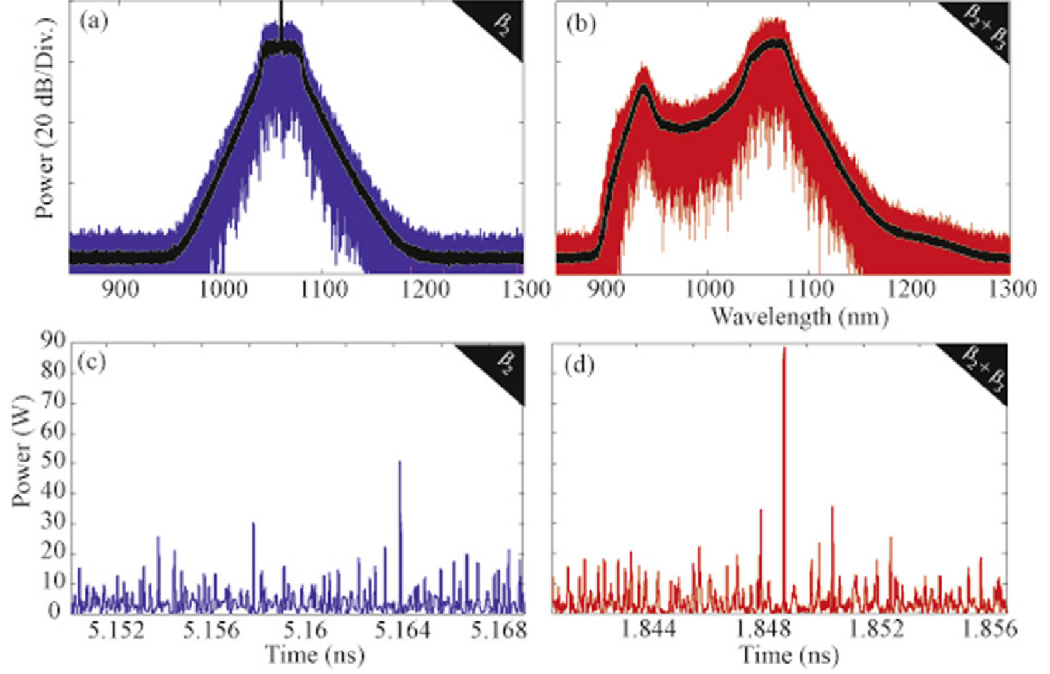
Figure 2.3: (a) Power spectrum as function of the wavelength and (c) instant power (i.e. the intensity $|u(z,t)|^2$) as function of time, taking into account only the second-order dispersion β_2. (b) Power spectrum and (d) instant power when the third-order dispersion β_3 is added to the simulation. The black solid lines correspond to the average spectra (image from [43]).

2.3 Generating optical rogue waves with third-order dispersion term

Taki et al. [43] studied rogue wave formation numerically using the generalized non-linear Schrödinger equation. Particularly the authors investigated the TOD contribution, i.e., they considered the gNLSE in the form

$$\partial_z u + \frac{i\beta_2}{2}\partial_t^2 u - \frac{\beta_3}{6}\partial_t^3 u - i\gamma|u|^2 u = 0, \tag{2.1}$$

with second order dispersion $\beta_2 = -2.6 \cdot 10^{-28}\text{s}^2\text{m}^{-1}$, third order dispersion $\beta_3 = 3.5 \cdot 10^{-41}\text{s}^3\text{m}^{-1}$, nonlinear coefficient $\gamma = 10\text{W}^{-1}\text{Km}^{-1}$ and a fiber length of 400m. To simulate the effect of supercontinuum generation, a plane wave of 10W plus a

23
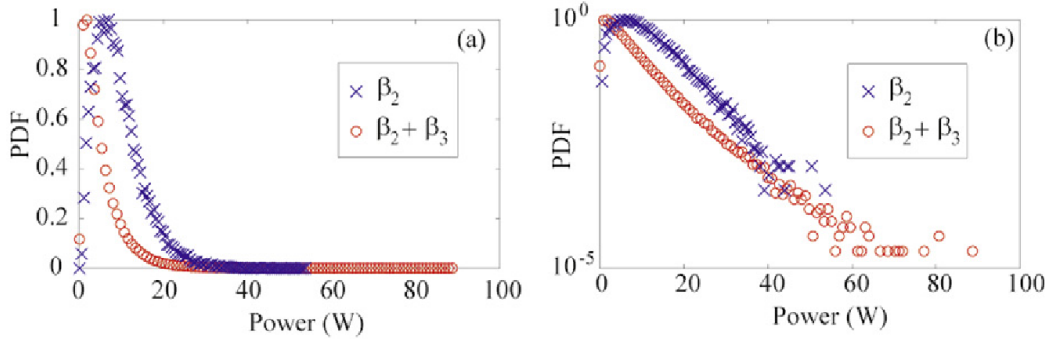
Figure 2.4: (a) PDFs corresponding to Fig. 2.3, as function of the peak power (i.e. the maximum intensity of the single soliton). The data are calculated with only β_2 (blue crosses) and with both β_2 and β_3 (red circles). (b) Same PDFs than in (a) in logarithmic scale. The PDFs are not normalized to 1 (image from [43]).

small Gaussian noise was chosen as initial condition. The authors found that the TOD term influences both the spectra and the PDF statistics of the system and consequently the RW appearance.

The spectra resulting from the integration of Eq. (2.1) are shown in Fig. 2.3. In Fig. 2.3 (a) only β_2 is taken into account, in Fig. 2.3 (b) both β_2 and β_3 are considered. As we can see the NLSE with TOD term generates a spectrum that is wider than the pure NLSE case and asymmetric with respect to the input wavelength. The instant powers, as function of time, are plotted in Fig. 2.3 (c) and (d) respectively for the pure NLSE and the NLSE with TOD case. Although Fig. 2.3 (c) and (d) look similar, the addition of β_3 term creates more powerful events.

The probability density functions of the peak powers are displayed in Fig. 2.4, in (a) linear and (b) logarithmic scales. The PDF generated by the pure NLSE has super-exponential tails, whereas when the TOD term is considered, the PDF has a hint of sub-exponential tails and above ~ 45W rare events are more likely than when only β_2 is considered. Note that a direct comparison between the PDFs in Fig. 2.2 and the ones in Fig. 2.4 is not possible, since Solli et al. [42] calculated the PDFs of the intensity whereas Taki et al. [43] show the PDFs of the peak power. Note, moreover that in both cases the distributions are not normalized to 1. The idea of using the gNLSE to describe rogue waves seems promising but Taki et al. [43]. PDFs have low accuracy on the tails, the more important region for rare events. To obtain better statistics requires more events, i.e. a larger time window of integration. Moreover it is not clear whether or not integrating over distances longer than 400m will produce

more powerful rogue waves.

Summary

In this chapter, we introduced optical rogue waves (RWs). We looked at Solli et al. [42] experimental results and we discussed Taki et al. [43] numerical results. The main lessons learned from these previous results are:

- Optical rogue waves are rare, high power, soliton-like pulses.

- Rogue waves have L-shaped probability density function.

- Optical rogue waves can be described by the generalized nonlinear Schrödinger equation. Particularly Taki et al. [43] could generate RWs using the gNLSE with third order dispersion term

$$\partial_z u + \frac{i\beta_2}{2}\partial_t^2 u - \frac{\beta_3}{6}\partial_t^3 u - i\gamma|u|^2 u = 0.$$

- To obtain good RW statistics from the numerical integration of the gNLSE, requires large time windows and distances of propagation.

In the next chapter, we will show how to deal with this last point and present some rogue wave results obtained from a massive parallel simulation of the gNLSE.

Part II Results

Chapter 3

Massive parallel simulation of rogue waves

As seen in the preceding chapter the generalized nonlinear Schrödinger equation can describe optical RWs. In this chapter we present results obtained by a massive parallel simulation of nonlinear optical fibers. In section 3.1 we discuss the advantages of a massive parallel integration of the gNLSE for RW statistics. The calculated probability density functions are shown in section 3.2. The role of the TOD term, on supercontinuum generation, is examined in section 3.3. Finally, in section 3.4 we consider a representative example for the propagation of the optical field in a short time range and extrapolate some insights on how RWs are generated.

3.1 Massive parallel integration of the gNLSE

The results of Taki et al. [43] show that the gNLSE with TOD produces RWs. Despite this achievement, the PDFs presented have low accuracy on the tails, the more important region for rare events. Furthermore at the distance of 400m, the fiber length used for the simulation, RWs are not fully developed. Results similar to Taki et al. [43] have been reported previously in the literature [62–65] although no high precision PDFs and no clear L-shaped statics has been given.

To have a better PDF statistics requires to simulate an adequate number of events, i.e. to integrate over a long time window, and to follow RW evolution demands integration over long distances. A single machine simulation cannot satisfies both conditions in a reasonable run time. Indeed to simulate a system with ~ 1000 pulses
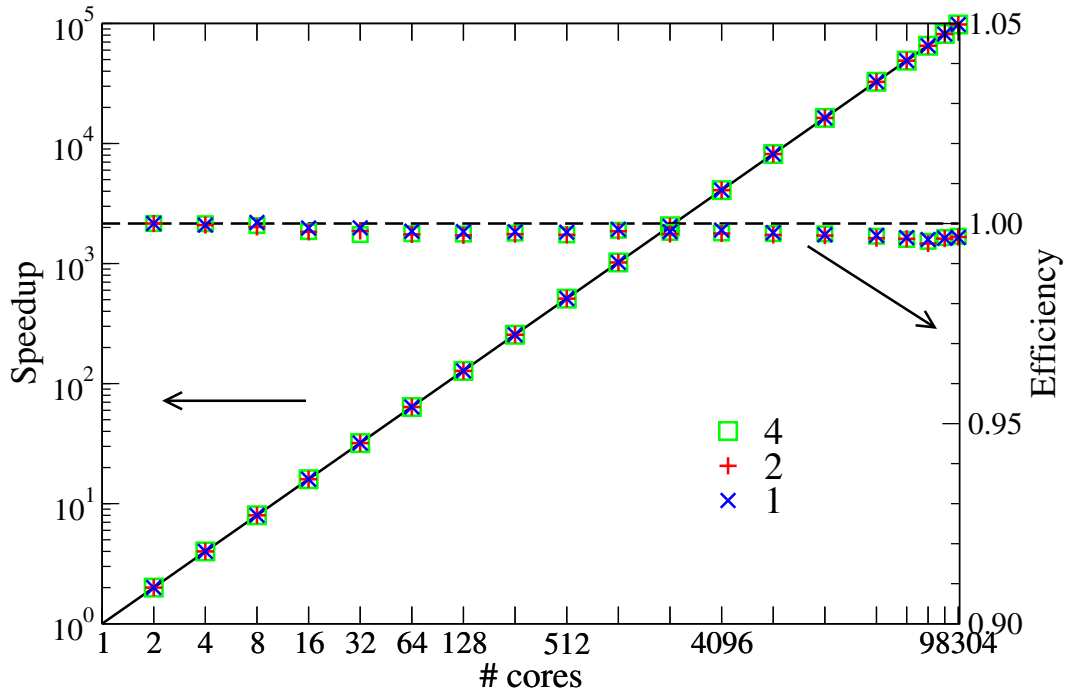
Figure 3.1: Parallel speedup (left axis) and efficiency (right axis) curves for the parallel implementation of the split-step Fourier method for the gNLSE. Runs for 3 different computational loads, each double in work size, are shown by different symbols with the solid line showing perfect linear scaling while the dashed line indicating 100% efficiency. The arrows indicate the corresponding axes. The computations were performed on the BlueGene/Q of the Hartree Centre.

that propagates for 1.5Km requires ~ 1 day on a single processor [40], and as we will see later a good RW statistics is obtained when the number of pulses is larger than 10^7. This is equivalent to ~ 30 years run time on a single processor. Therefore we used a massive parallel numerical procedure [40] to integrate the gNLSE with TOD. An implementation of the split-step Fourier algorithm based on the overlap/save method [85] was used to integrate Eq. (2.1) with 2^{31} intervals of $\Delta t = 1.8$fs and hence long time windows up to 3.865×10^6ps and 1.5 kilometers in propagation distance [40]. The overlap/save method is a numerical algorithm that allows the parallelization of the fast Fourier transform (FFT). The idea is to compute the FFT of short segments on different machines and then concatenate the segments together to obtain the FFT of the full time window [85].

We assumed periodic boundary conditions in time and, as usual, a coordinate frame moving with the group velocity. We parallelized the fast Fourier transform part of the code to take advantage of high-performance computing machines. In Fig. 3.1,
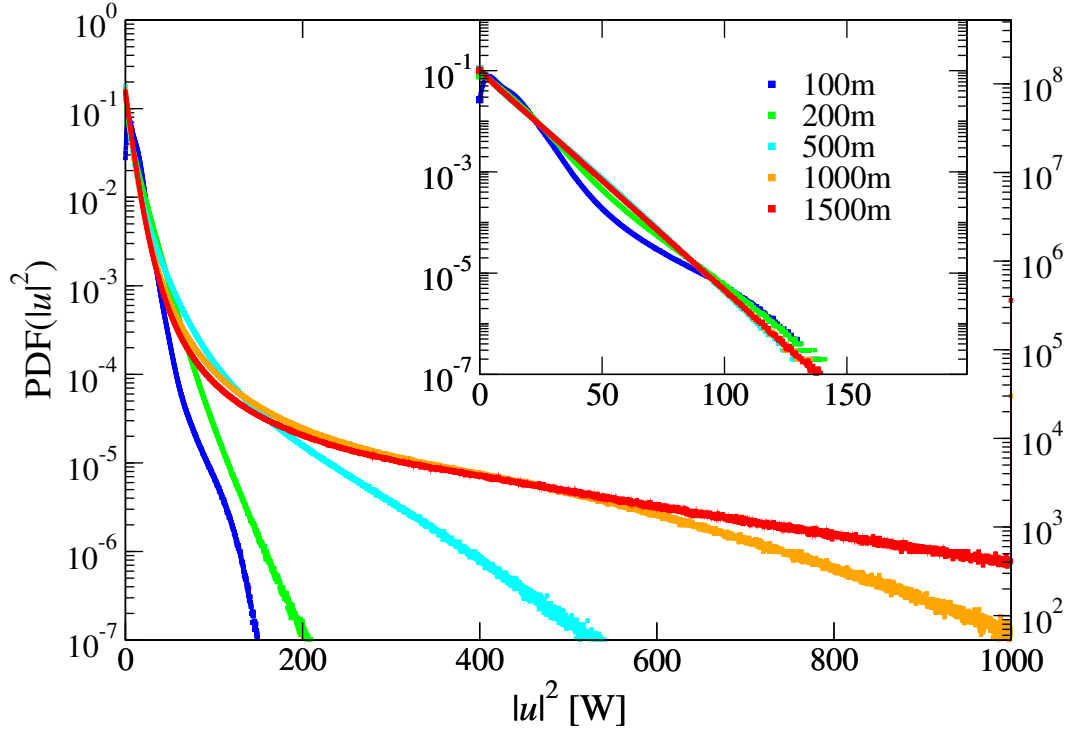
Figure 3.2: PDFs of the intensity $|u|^2$ from the gNLSE Eq. (2.1) with $\beta_3 = 2.64 \times 10^{-42}\text{s}^3\text{m}^{-1}$ using a large time window of $\Delta t = 3.865 \times 10^6\text{ps}$. The PDFs have been computed at distances $z = 100\text{m}, 200\text{m}, 500\text{m}, 1000\text{m}$ and 1500m. The left vertical axis denotes the values of the normalized PDF while the right vertical axis gives the event count per bin. The inset shows results for $\beta_3 = 0$.

we show the speedup and efficiency of a test run on the 98k cores at the Hartree Centre. The results show linear scaling and nearly 100% efficiency.

We start the simulations with a continuous wave of $P_0 = 10\text{W}$ power. For the fiber, we assume the parameters $\beta_2 = -2.6 \times 10^{-28}\text{s}^2\text{m}^{-1}$, $\beta_3 = 2.64 \times 10^{-42}\text{s}^3\text{m}^{-1}$ and $\gamma = 0.01 \text{ W}^{-1}\text{m}^{-1}$. Due to the modulation instability, we observe, after seeding with a small 10^{-3}W Gaussian noise, a break-up into individual pulses within the first 100m of the simulation, then rogue waves start to appear. The PDF of $|u|^2$ is computed as the simulation progresses. Throughout the simulation, we check that the energy (1.26) remains conserved.

3.2 Probability density functions

The PDF for the complete set of $\gtrsim 17 \times 10^6$ pulses propagating over 1500m is shown in Fig. 3.2 for selected distances using a highly-optimised, massively parallel and

29

linearly-scaling numerical procedure [40]. After 100m, the PDF exhibits a roughly exponential distribution as seen in Fig. 3.2. With $\beta_3 = 0$ this exponential PDF remains stable from this point onwards (cp. inset). However, with $\beta_3 \neq 0$ the inelastic collision of soliton like pulses leads to an ever increasing number of high-energy RWs. After 500m, a clear deviation from the exponential distribution of the $\beta_3 = 0$ case has emerged and beyond 1000m, the characteristic L-shape of a fully-developed RW PDF has formed. The PDFs in Figs. 3.2 then continue to evolve towards higher peak powers.

3.3 Spectra

In Chapter 2 we saw that optical rogue waves are created during supercontinuum generation, a broadening of the power spectrum from a narrow-band input wave [35, 36]. In this section we look at the spectra generated by our numerical integration of Eq. (2.1). In Fig. 3.3 (a) and (b) we show the power spectra $|u(\omega)|^2$ as function of the frequency ω, respectively for $\beta_3 = 0$ and $\beta_3 = 2.64 \times 10^{-42} \text{s}^{-4}\text{m}^{-1}$. The spectra are displayed for various distances z up to 1500m. The much broader spectrum for $\beta_3 \neq 0$ shows how the TOD has led to wave excitation across a broad range of frequencies. This is directionally related to the higher intensity observed in the PDFs, indeed the most powerful pulses will have wider spectra. Fig. 3.3 (b) also shows an asymmetry in the spectra, particularly we can see a peak between the frequencies 200ps^{-1} and 400ps^{-1}. This peak is related to a presence of radiation in the optical field background [28] and corresponds to the inversion of sign in the dispersion $(\beta(\omega) = \frac{\beta_2}{2}\omega^2 + \frac{\beta_3}{6}\omega^3)$ that occurs at $\omega = -3\beta_2/\beta_3 \simeq 300\text{ps}^{-1}$. Note that in the Fig. 3.3 the spectra are plotted only in the frequency range $[-800, +800]\text{THz}$ but the actual range of integration is $\left[-\frac{\pi}{\triangle t}, +\frac{\pi}{\triangle t}\right] \simeq [-1750, +1750]\text{THz}$ according to the value used for $\triangle t$.

3.4 Rogue wave trajectories

In Fig. 3.4, we show a representative example for the propagation of $u(z, t)$ in a short 15ps time range out of the full 3.865×10^6 ps. A small initial noise leads to differences in the pulse powers and velocities and hence to eventual collisions of neighbouring pulses. We call these soliton like pulses quasi-solitons because although they are localized their energy is not conserved. In the enlarged trajectory plots of

Figs. 3.4(b) and 3.4(c), we see that for $\beta_3 = 0$ the solitons interact elastically and propagate on average with the group velocity of the frame. However, for finite β_3 in Fig. 3.4(c), most collisions are *inelastic* and one quasi-soliton, with higher energy, moves through the frame from left to right due to its higher energy and group velocity mismatch compared to the frame. It collides in rapid succession with the other quasi-solitons traveling, on average, at the frame velocity. In almost all cases, energy is transferred from the quasi-soliton with less energy to the one with more energy leading to a cascade of incremental gains for the more powerful quasi-soliton. This pattern is visible throughout Fig. 3.4(a) where initial differences in power of quasi-solitons become exacerbated over time and larger and larger quasi-solitons emerge. These accumulate the energy of the smaller ones to the point that the smaller ones eventually vanish into the background. In addition, the group velocity of a quasi-soliton with TOD is dependent on the power of the quasi-soliton [26]. Thus, the emerging powerful quasi-solitons feature a growing group velocity difference to their peers and this increases their collision rate leading to even stronger growth. This can clearly be seen from Fig. 3.4(a) where larger-energy quasi-solitons start to move sideways as their velocity no longer matches the group velocity of the frame after they have acquired energy from other quasi-solitons due to inelastic collisions. Indeed, the relatively few remaining, soliton-like pulses at 1500m can have peak powers exceeding 1000W. They are truly self-sustaining rogues that have increased their power values by successive interactions and energy exchange with less powerful pulses.

Fig. 3.4 shows how rogue waves are created by a cascade of incremental energy gains. In the next chapters we will see that it is possible to implement this cascade mechanism into an effective model that produces PDFs directly without the need for integrating the gNLSE. Such model requires to understand the nature of quasi-solitons and how they interact, therefore we will dedicate the next two chapters to these topics then we will go in detail into the effective cascade model.
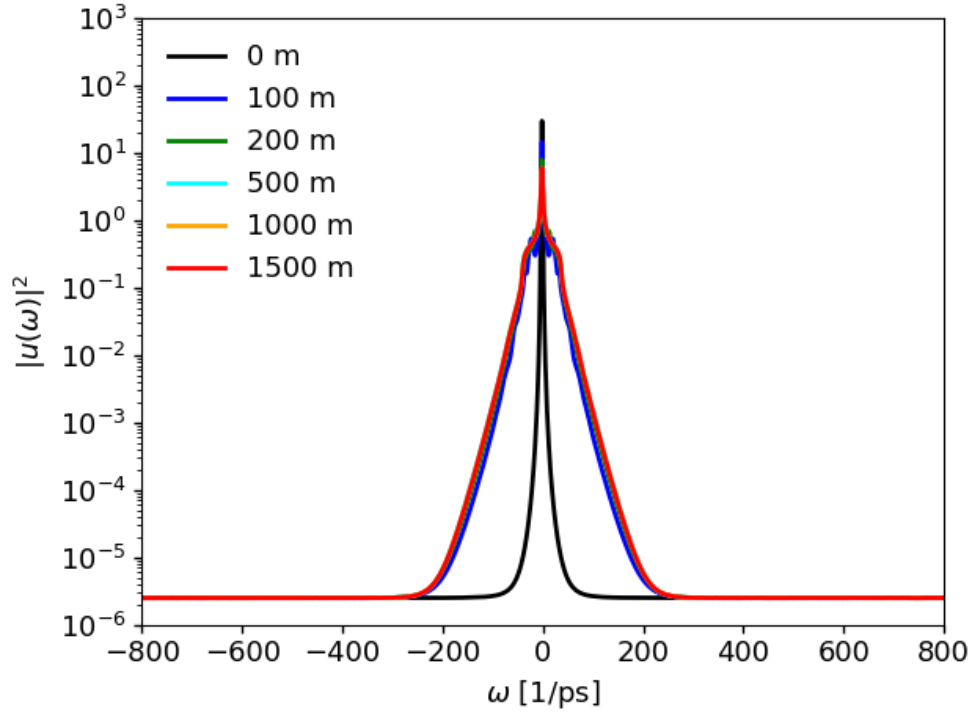
(a)
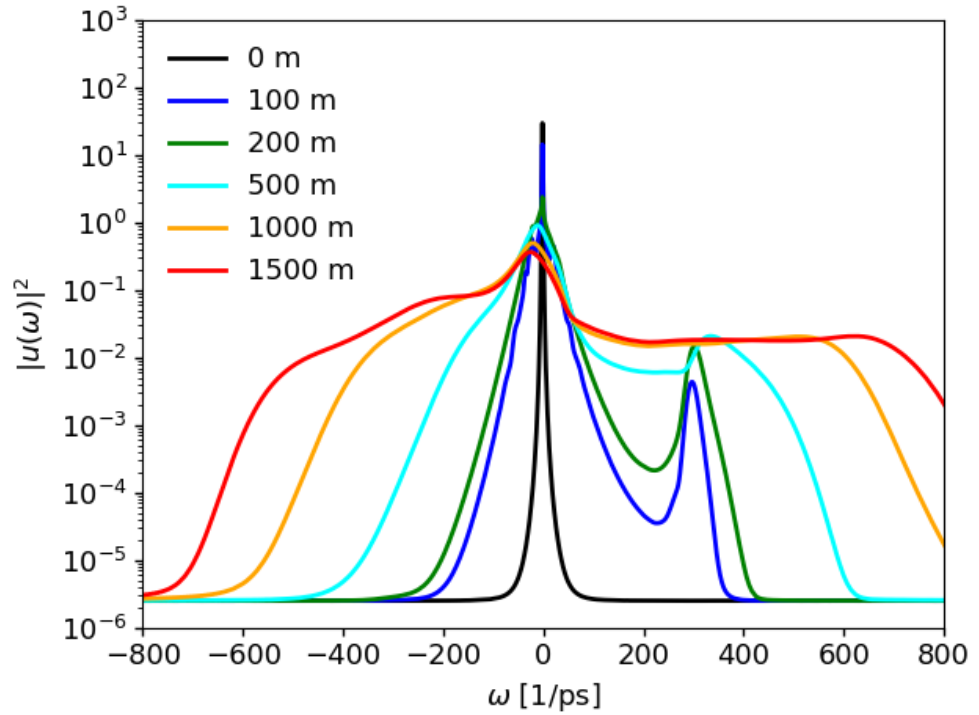
(b)

Figure 3.3: (a) Spectrum $|u(\omega)|^2$ as function of the frequency ω for $\beta_3 = 0$. The results are displayed at distances $z = 100$m, 200m, 500m, 1000m and 1500m. (b) Spectrum $|u(\omega)|^2$ for $\beta_3 = 2.64 \times 10^{-42}$s^{-4}m^{-1} at the same distances as in (a).
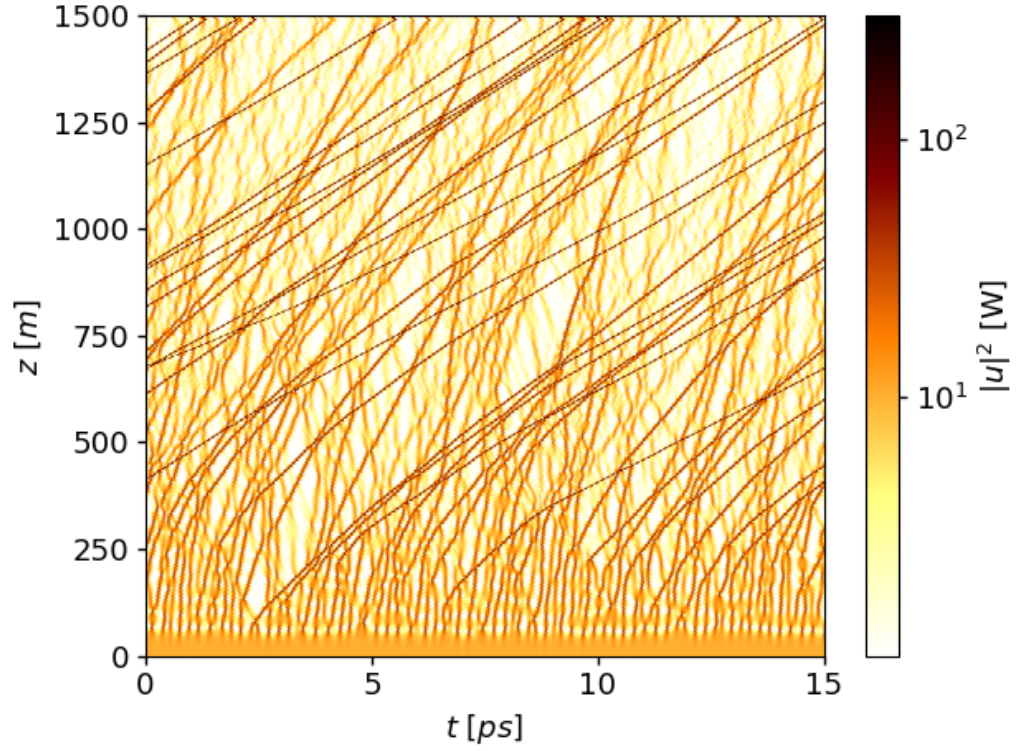
(a)
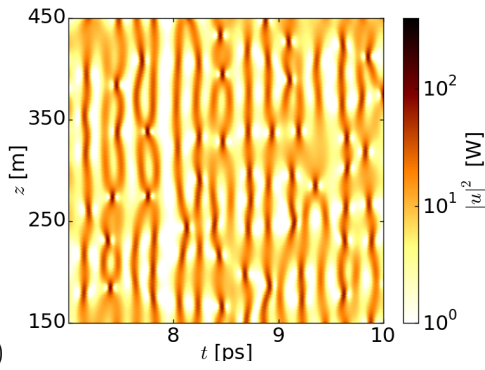
(b)
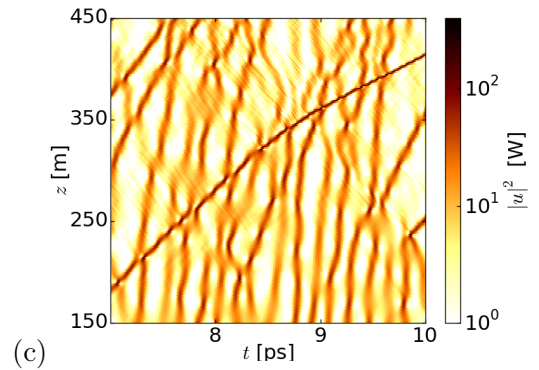
(c)

Figure 3.4: (a) Intensity $|u(z,t)|^2$ for $\beta_3 = 2.64 \times 10^{-42} \mathrm{s}^3 \mathrm{m}^{-1}$ of the gNLSE Eq. (2.1) as function of the time t and distance z in a selected time frame of $\Delta t = 15$ps and distance range $\Delta z = 1.5$km. (b) $|u|^2$ with $\beta_3 = 0$ for a zoomed-in distance and time region, (c) $|u|^2$ with β_3 value as in (a) for a region of (a) with Δt and Δz chosen identical to (b).

Summary

In this chapter, we presented numerical results from our massive parallel simulation of the generalized nonlinear Schrödinger equation. The main points of the chapter are:

- Using a parallel implementation of the split-step Fourier algorithm we can integrate the gNLSE with more than 17×10^6 pulses propagating over 1500m.

- The gNLSE with TOD generates clear L-shaped PDFs. Longer space distances of integration produce heavier tails in the PDFs.

- The gNLSE with TOD term β_3 generates asymmetric and wider spectra that when $\beta_3 = 0$. The asymmetry is related to the presence of radiation in the background whereas the broadening is due to the higher intensity observed in the PDFs.

- Looking at the propagation of the optical field $u(z,t)$, it seems that rogue waves are created by a cascade of incremental energy gains.

In the following chapter, we will introduce the concept of quasi-soliton and derive some analytical approximations that will be used in later chapters.

Chapter 4

Quasi-solitons in a $\beta_3 \neq 0$ medium

In this chapter we show that the gNLSE has soliton-like solutions. Section 4.1 introduces the quasi-soliton approximation. The difference between dark and bright quasi-solitons is considered in section 4.2. Finally, in section 4.3 we discuss a decomposition into soliton–radiation for the gNLSE.

4.1 Quasi-solitons approximation

In chapter 1 we saw that the NLSE has a soliton solution. In the case of the gNLSE with TOD (2.1), the solution can be approximated with a soliton-like pulse [26, 86]

$$u(z,t) = \sqrt{P} \, \text{sech}\left[\frac{t-q}{T}\right] \exp\left[i\left(\frac{\beta_2}{2}\Omega^2 + \frac{\beta_3}{6}\Omega^3 + \frac{\gamma P}{2}\right)z - i\Omega t - iC\frac{t^2}{2T^2}\right]. \quad (4.1)$$

In Eq. (4.1) P, T and C represent the amplitude, duration and chirp. The other two parameters are the temporal shift q of the pulse envelope and the frequency shift Ω of the pulse spectrum. The unknown parameters can be found using the momentum method [26, 87, 88]. The idea is to treat the optical pulse as a particle with momenta

$$\begin{aligned}
T^2 &= \frac{12}{\pi^2 E} \int_{-\infty}^{+\infty} (t-q)^2 |u|^2 dt, & C &= \frac{i6}{\pi^2 E} \int_{-\infty}^{+\infty} (t-q)\left(u^*\frac{\partial u}{\partial t} - u\frac{\partial u^*}{\partial t}\right) dt, \\
q &= \frac{1}{E} \int_{-\infty}^{+\infty} t |u|^2 dt, & \Omega &= \frac{i}{2E} \int_{-\infty}^{+\infty} \left(u^*\frac{\partial u}{\partial t} - u\frac{\partial u^*}{\partial t}\right) dt,
\end{aligned} \quad (4.2)$$

where the energy E is defined as usual by Eq. (1.26). In (4.2) T measures how far a pulse is spread out, C represents the time dependence of the instantaneous frequency (the temporal derivative of the phase), q is the average position in time of the pulse intensity and Ω is the average frequency of the power spectrum.

Using Eqs. (2.1, 4.1, 4.2) we obtained the distance-dependence of the parameters

$$
\frac{dT}{dz} = (\beta_2 + \beta_3\Omega)\frac{C}{T}, \qquad\qquad \frac{dC}{dz} = \left(\frac{4}{\pi^2} + C^2\right)\frac{(\beta_2 + \beta_3\Omega)}{T^2} + \frac{4\gamma P}{\pi^2},
$$
$$
\frac{dq}{dz} = \beta_2\Omega + \frac{\beta_3}{2}\Omega^2 + \frac{\beta_3}{6T^2}\left(1 + \frac{\pi^2}{4}C^2\right), \quad \frac{d\Omega}{dz} = 0.
$$
$$(4.3)$$

The equations can be solved for $C = 0$, resulting in

$$
u(z,t) = \sqrt{P}\,\mathrm{sech}\left[\frac{t - v^{-1}z}{T}\right]\exp\left[i\left(\frac{\beta_2}{2}\Omega^2 + \frac{\beta_3}{6}\Omega^3 + \frac{\gamma P}{2}\right)z - i\Omega t\right], \qquad (4.4)
$$

with T and v^{-1} given by

$$
v^{-1} = \beta_2\Omega + \frac{\beta_3}{2}\Omega^2 + \frac{\beta_3}{6T^2}, \qquad\qquad (4.5)
$$

$$
T = \sqrt{\frac{|\beta_2 + \beta_3\Omega|}{\gamma P}}. \qquad\qquad (4.6)
$$

The TOD changes the soliton shape, particularly the pulse width T and group velocity v are modified by the β_3 term.

Numerically solving Eq. (2.1), with initial conditions given by Eq. (4.4, 4.5, 4.6), we can see the limitations of our approximation. In Fig. 4.1 we show the intensities $|u(z,t)|^2$, of a soliton ($\beta_3 = 0$) and a quasi-soliton ($\beta_3 = 2.64 \times 10^{-42}\mathrm{s}^3\mathrm{m}^{-1}$), as function of the time t for various distances. The simulation parameters are $\beta_2 = -2.6 \times 10^{-28}\mathrm{s}^2\mathrm{m}^{-1}$, $\gamma = 0.01$ W^{-1}m^{-1}, $P = 100$W and $\Omega = -10$THz. In Fig. 4.1 (a) and (c) we can see the soliton propagation, respectively in linear and logarithmic scale. As expected the soliton moves in space and time without changing its shape. Fig. 4.1 (b) and (d) display the quasi-soliton intensity, respectively in linear and logarithmic scale. Unlike the previous case, the pulse radiate energy as dispersive wave and its peak power decreases. This process slows down with the distances and the quasi-soliton radiates less and less energy. Fig. 4.1 highlights that approximation (4.4) (used as initial condition) roughly describes the peak part of quasi-solitons but
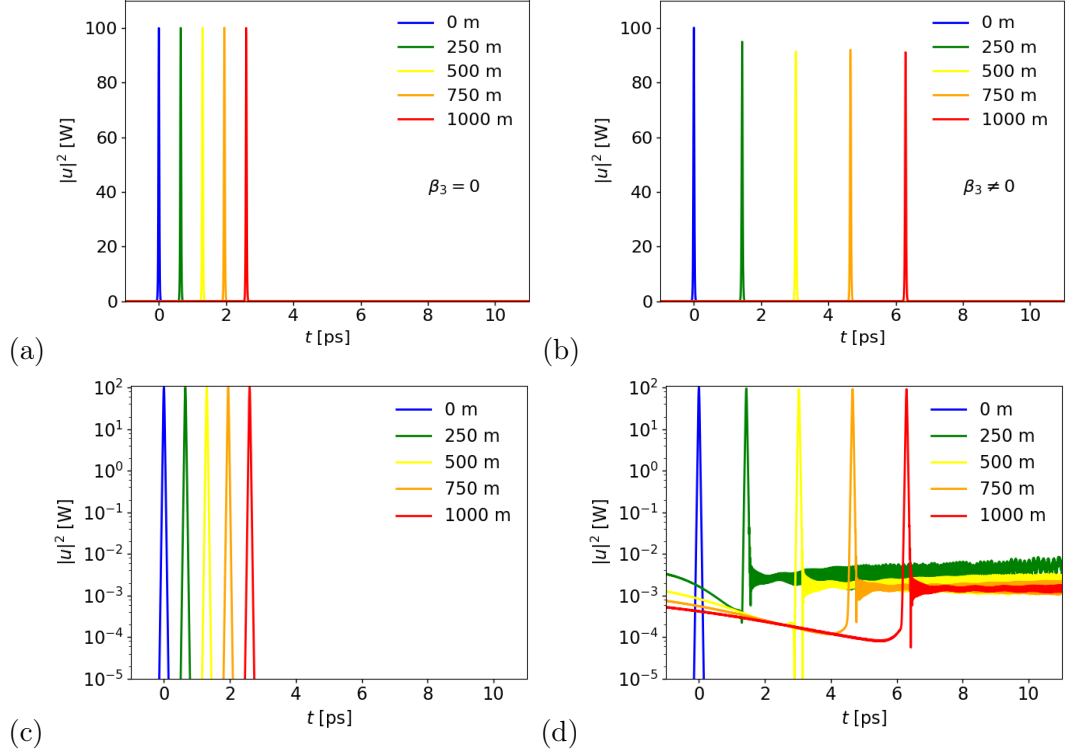
Figure 4.1: (a) Intensity $|u(z,t)|^2$ as function of the time t for gNLSE with $\beta_3 = 0$. The Intensity has been computed at distances $z = $ 0m, 250m, 500m, 750m and 1000m. (b) Intensity as function of time for $\beta_3 = 2.64 \times 10^{-42} \mathrm{s}^3 \mathrm{m}^{-1}$ and same distances used in (a). Figures (c) and (d) show respectively the same results of (a) and (b) in logarithmic scale.

fails to describe the process of energy emission.

Fig. 4.2 (a) and (b) illustrate the spectra of the same soliton and quasi-soliton shown in Fig. 4.1. The spectra are similar close to the frequency shift $\omega = \Omega$ and differ faraway from this value. The quasi-soliton spectrum deviates from a soliton spectrum between the frequencies $200\mathrm{ps}^{-1}$ and $400\mathrm{ps}^{-1}$. Here we see a second peak generated by the radiation in the optical field background [28]. This peak corresponds to the inversion of sign in the dispersion $(\beta(\omega) = \frac{\beta_2}{2}\omega^2 + \frac{\beta_3}{6}\omega^3)$ that occurs at $\omega = -3\beta_2/\beta_3 \simeq 300\mathrm{ps}^{-1}$. As we can see, the radiation peak has actually a higher value than $\omega = -3\beta_2/\beta_3$, this can be understood as a recoil effect to stabilize the soliton. Indeed the soliton peak, in order to be more stable, moves away from the critical frequency towards lower frequencies, but because the average frequency is conserved, the radiation peak compensates this change moving towards higher frequencies.
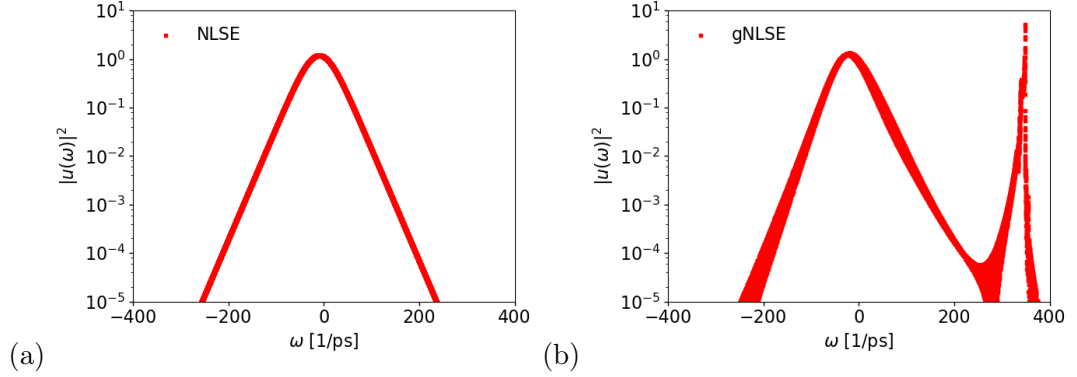
Figure 4.2: Spectrum $|u(\omega)|^2$ as function of the frequency ω at $z = 1000$m for (a) $\beta_3 = 0$ and (b) $\beta_3 = 2.64 \times 10^{-42} \text{s}^3\text{m}^{-1}$.

4.2 Dark and bright quasi-solitons

Until now we have discussed bright quasi-solitons supported by Eq. (2.1). The same equation sustains also dark quasi-solitons. The type of solution depends on the value of the frequency shift Ω. Let's write the optical field as

$$u(z,t) = U(z,t)e^{iKz - i\Omega t}, \tag{4.7}$$

where $K = \frac{\beta_2}{2}\Omega^2 + \frac{\beta_3}{6}\Omega^3$ is the pulse wave number. Replacing Eq. (4.7) into Eq. (2.1) we obtain

$$\partial_z U + K'\partial_t U + \frac{i\beta_2^*}{2}\partial_t^2 U - \frac{\beta_3}{6}\partial_t^3 U - i\gamma|U|^2 U = 0. \tag{4.8}$$

The previous equation is similar to Eq. (2.1). The term proportional to $K' = \beta_2\Omega + \frac{\beta_3}{2}\Omega^2$ can be eliminated using the transformation $t \to t - K'z$. The effective second order dispersion

$$\beta_2^* = \beta_2 + \beta_3\Omega \tag{4.9}$$

determines the type of quasi-soliton. For $\beta_2^* < 0$ the solution of Eq. (4.8) is a bright quasi-soliton (see Fig. 4.1 (b) and (d)), for $\beta_2^* > 0$ we get a dark quasi-soliton. The sign of β_2^* depends on the frequency shift, with critical value given by $\Omega^* = -\frac{\beta_2}{\beta_3}$. When $\Omega > -\frac{\beta_2}{\beta_3}$ and $\beta_3 \ll \beta_2^*$, Eq. (2.1) has the approximated dark quasi-soliton solution
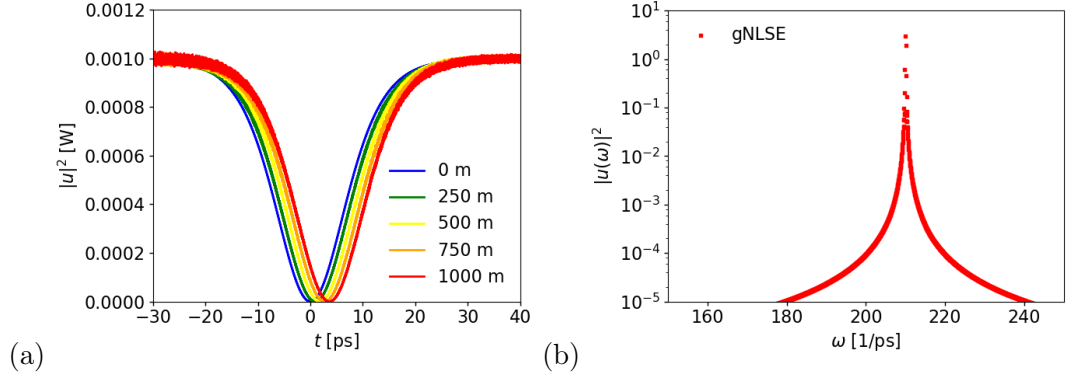
Figure 4.3: (a) Dark quasi-soliton intensity $|u(z,t)|^2$ as function of the time t for distances $z = 0$m, 250m, 500m, 750m and 1000m and $\beta_3 = 2.64 \times 10^{-42}$s^{3}m^{-1}. (b) Spectrum $|u(\omega)|^2$, corresponding to (a), as function of the frequency ω at $z = 1000$m.

$$u(z,t) = \sqrt{P}\,\tanh\left[\frac{t - K'z}{T}\right]\exp[i\left(K + \gamma P\right)z - i\Omega t]\,, \qquad (4.10)$$

with T given by Eq. (4.6). Fig. 4.3 (a) and (b) show a dark quasi-soliton intensity as function of the time t and the corresponding spectrum as function of the frequency ω. The result are obtained numerically solving Eq. (2.1) with initial conditions given by Eq. (4.10). The quasi-soliton frequency shift is $\Omega = 210$THz and the initial power is $P = 10^{-3}$W. We chose such a small value because higher powers lead to instability of the dark soliton. Indeed Eq. (4.10) is not exact solution of Eq. (2.1) therefore a reshaping radiation is emitted during the pulse propagation, because dark pulses are not localized such radiation is emitted across the full simulation time window. For this reason dark solitons are less stable than bright solitons.

4.3 Decomposition soliton – radiation

In section 4.1 we saw that bright quasi-solitons have a soliton and a radiation part. In this section we will find a differential equation for each of the two parts. We start writing the optical field as a sum of two terms

$$u(z,t) = [S(z,t) + R(z,t)]\,e^{iKz - i\Omega t}, \qquad (4.11)$$

where S is the soliton part and R is the radiation part. The oscillatory term $e^{iKz - i\Omega t}$ reflects the fact that our quasi-soliton has frequency shift Ω and wave number $K = \frac{\beta_2}{2}\Omega^2 + \frac{\beta_3}{6}\Omega^3$. Replacing Eq. (4.11) into Eq. (2.1) we obtain a differential equation
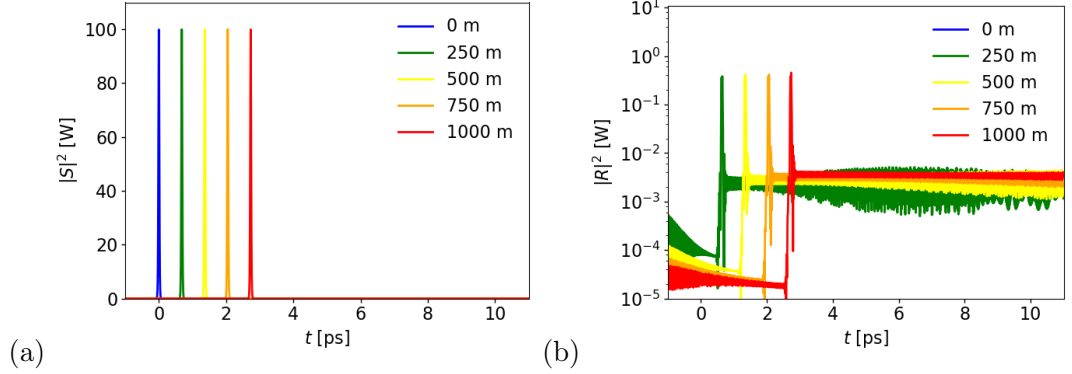
Figure 4.4: (a) Bright soliton intensity $|S(z,t)|^2$ as function of the time t for distances $z = 0$m, 250m, 500m, 750m and 1000m. (b) Radiation intensity $|R(z,t)|^2$ corresponding to (a) and generated using Eq. (4.13).

with mixed terms proportional to powers of S and R. We want an equation for each of the two quasi-soliton parts. This task is not easy because there is not criterion on how to assign each term to the corresponding equation. Akhmediev and Karlsson suggested the approximation [28]

$$\partial_z S + K' \partial_t S + \frac{i\beta_2^*}{2}\partial_t^2 S - i\gamma|S|^2 S = 0, \tag{4.12}$$

$$\partial_z R + K' \partial_t R + \frac{i\beta_2^*}{2}\partial_t^2 R - \frac{\beta_3}{6}\partial_t^3 R = \frac{\beta_3}{6}\partial_t^3 S, \tag{4.13}$$

where the soliton part does not interact with the radiation part and the term $\frac{\beta_3}{6}\partial_t^3 S$ acts as a source for R. In the above equations all the mixed terms containing both S and R have been neglected. The soliton part has the exact solution

$$S(z,t) = \sqrt{P}\,\text{sech}\left[\frac{t - K'z}{T}\right]\exp\left(i\frac{\gamma P}{2}z\right), \tag{4.14}$$

where $T = \sqrt{|\beta_2^*|/\gamma P}$. Fig. 4.4 shows (a) $|S|^2$ as function of time for various distances and (b) the corresponding radiation intensity $|R|^2$ obtained integrating numerically Eq. (4.13). The initial values of power and frequency shift are the same used in Fig. 4.1. In Fig. 4.4 (b) the $|R|^2$ value on the right side of the soliton peak at 1.5Km, is $\sim 3 \cdot 10^{-3}$W, whereas in Fig. 4.1 (d) we observe a value of $\sim 1.5 \cdot 10^{-3}$W. We have such discrepancy between the two radiation values because the energy in Eq. (4.13) is not conserved. The reason is that the source term $\frac{\beta_3}{6}\partial_t^3 S$ keeps generating more and more radiation during the pulse propagation. Indeed, in Fig. 4.1 (d) the amount

of radiation emitted by the quasi-soliton decreases with the distance, while in Fig. 4.4 (b) it increases.

We numerically tested several decompositions of Eq. (2.1) in soliton and radiation part. The test was performed comparing the spectra of the full gNLSE $|u(\omega)|^2$, calculated using Eq. (2.1), and the spectra obtained from the decompositions $|S(\omega)+R(\omega)|^2$. We found that the following coupled equations describe well a quasi-soliton and its radiation

$$\partial_z S + K'\partial_t S + \frac{i\beta_2^*}{2}\partial_t^2 S - i\gamma|S|^2 S = 2i\gamma|S|^2 R + i\gamma S^2 R^*, \qquad (4.15)$$

$$\partial_z R + K'\partial_t R + \frac{i\beta_2^*}{2}\partial_t^2 R - \frac{\beta_3}{6}\partial_t^3 R - i\gamma|R|^2 R = \frac{\beta_3}{6}\partial_t^3 S + 2i\gamma|R|^2 S + i\gamma R^2 S^*. \quad (4.16)$$

In the above equations we still have $\frac{\beta_3}{6}\partial_t^3 S$ as source term for the radiation, but now the two optical fields are linearly coupled with each other. The same type of coupling was suggested by Karpman and Solov'ev [22] for a two soliton systems, that is for $\beta_3 = 0$, when no radiation is involved in the process. Fig. 4.5 (a) displays the comparison between the two spectra $|u(\omega)|^2$ and $|S(\omega)+R(\omega)|^2$. As we can see there is a good agreement between the two results considering that the Eqs. (4.15, 4.16) are an approximation (linear decomposition) of Eq. (2.1). In Fig. 4.5 (b) we show the intensity $|u(z,t)|^2$ as function of time for different distances. The corresponding soliton $|S(z,t)|^2$ and radiation $|R(z,t)|^2$ intensities are shown respectively in Fig. 4.5 (c) and (d).

Although the soliton-radiation decomposition is an interesting results we do not have an analytical solution for Eq. (4.15) and Eq. (4.16). On the other hand, the quasi-soliton approximation Eq. (4.4, 4.5, 4.6) does not describe the radiation part but it is a good description of the peak propagation. We observe that the radiation part is more than 4 orders of magnitude smaller than the soliton part, therefore for the purpose of our work we will use the simple quasi-soliton approximation (4.4).
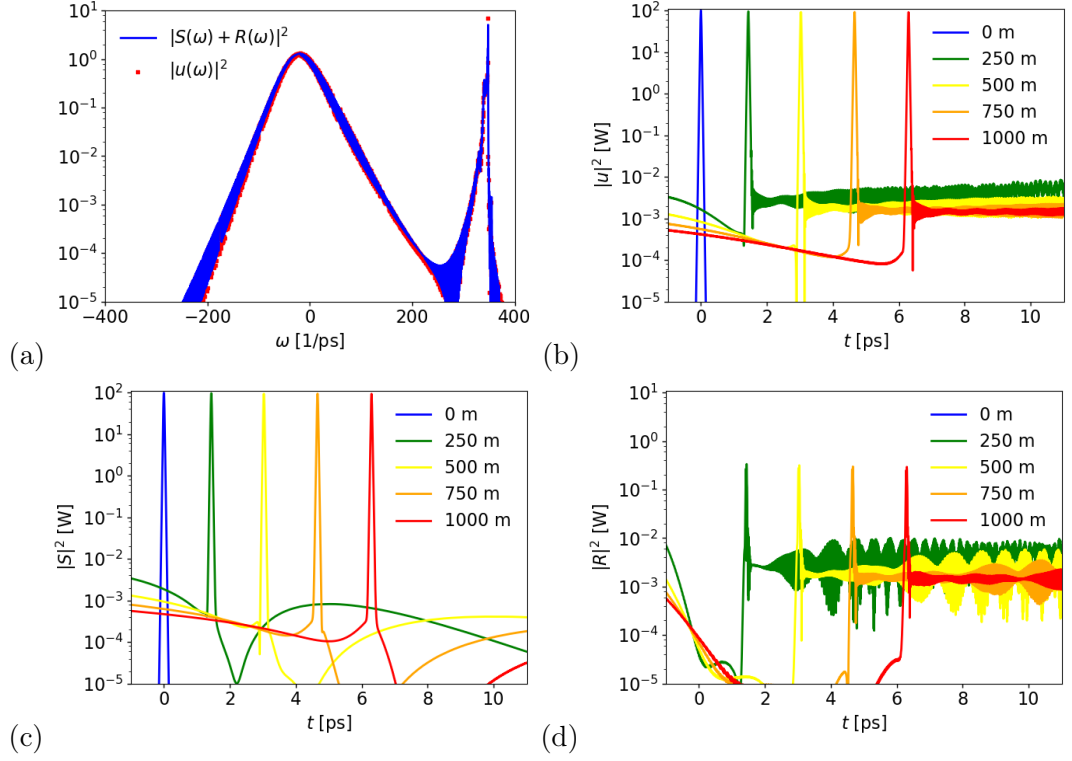
Figure 4.5: (a) Comparison between the spectra $|u(\omega)|^2$ and $|S(\omega) + R(\omega)|^2$. (b) Intensity $|u(z,t)|^2$ as function of time t for distances $z = 0$m, 250m, 500m, 750m and 1000m. (c) Soliton $|S(z,t)|^2$ and (d) radiation $|R(z,t)|^2$ intensities corresponding to (b).

Summary

In the this chapter, we introduced the concept of a quasi-soliton and derived an analytical approximation based on the momentum method. The key points of the chapter are:

- The gNLSE with TOD has soliton-like solutions called quasi-solitons. The optical field of such pulses can be approximated by

$$u(z,t) = \sqrt{P}\, \text{sech}\left[\frac{t - v^{-1}z}{T}\right] \exp\left[i\left(\frac{\beta_2}{2}\Omega^2 + \frac{\beta_3}{6}\Omega^3 + \frac{\gamma P}{2}\right)z - i\Omega t\right],$$

with $T = \sqrt{\frac{|\beta_2 + \beta_3\Omega|}{\gamma P}}$ and $v^{-1} = \beta_2\Omega + \frac{\beta_3}{2}\Omega^2 + \frac{\beta_3}{6T^2}$.

- The main difference between a soliton and a quasi-soliton is that the later radiates energy during its propagation.

- The gNLSE with TOD sustains both bright and dark quasi-solitons. Whether the solution is a bright or dark quasi-soliton depends on the sign of the effective second order dispersion $\beta_2^* = \beta_2 + \beta_3 \Omega$.

- It is possible to decompose the gNLSE with TOD in soliton and radiation part of a quasi-soliton. The radiation part is much smaller than the soliton part.

In the next chapter, we will discuss the interaction between two quasi-solitons, an important ingredient for rogue wave generation.

Chapter 5

Interacting quasi-solitons

Energy gain is an important concept for rogue wave generation. In this chapter we consider the interaction between two quasi-solitons, particularly we focus on the energy transfer during the scattering process. Section 5.1 presents some numerical results for the collision of two quasi-solitons. In section 5.2 we discuss an attempt to calculate analytically the energy transfer using a two quasi-soliton decomposition of the gNLSE. Finally, in section 5.3 we show that a functional form of the energy transfer can be found using some general assumptions on the interaction.

5.1 Two quasi-soliton scattering

In this section we study the two quasi-soliton scattering in a β_3 medium. Eq. (2.1) is numerically solved with an initial condition consisting of two pulses

$$u\left(z,t\right) = \sqrt{P_1}\mathrm{sech}\left(\frac{t-t_1}{T_1}\right)e^{-i\Omega_1(t-t_1)} + \sqrt{P_2}\mathrm{sech}\left(\frac{t-t_2}{T_2}\right)e^{-i\Omega_2(t-t_2)+i\phi}. \quad (5.1)$$

The two waves have a relative phase difference ϕ, and are characterized by power P_i, temporal shift t_i and frequency shift Ω_i for each pulse $i = 1, 2$. From these initial conditions we can calculate their inverse velocity $v_i^{-1} = \beta_2\Omega_i + \frac{\beta_3}{2}\Omega_i^2 + \frac{\beta_3}{6T_i^2}$ and period $T_i = \sqrt{\frac{|\beta_2+\beta_3\Omega_i|}{\gamma P_i}}$.

In Fig. 5.1 we show an example of scattering between two quasi-solitons. The initial conditions for both collisions have been chosen to be identical apart from the relative phase between the two quasi-solitons, in Fig. 5.1(a) $\phi = 0.27\pi$ whereas in Fig. 5.1(b) $\phi = 1.13\pi$. For both cases an earlier quasi-soliton with initially large power (200W) is met by a later, initially weak pulse (50W). Clearly, the collision of these two
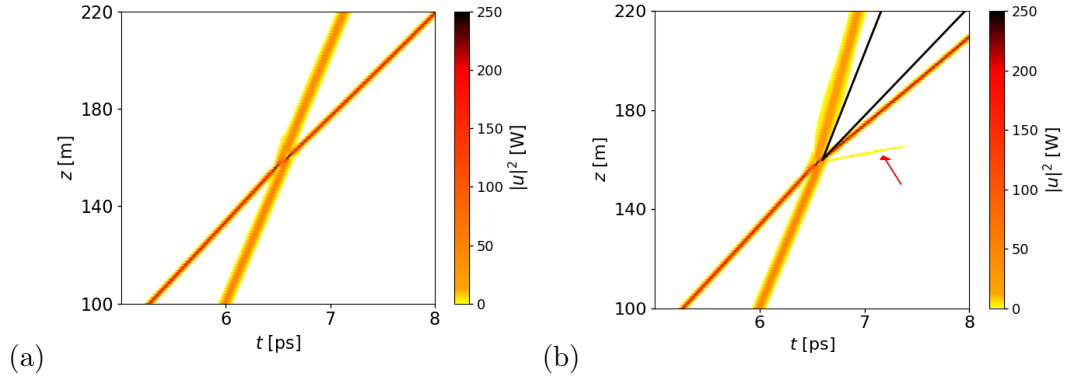
Figure 5.1: Intensities $|u(z,t)|^2$ of the scattering between two quasi-solitons for $\beta_3 = 2.64 \times 10^{-42} \text{s}^3\text{m}^{-1}$. The phase difference ϕ was chosen to correspond to (a) the minimum and (b) the maximum of $\Delta E_1/E_2(\phi)$ plotted in Fig. 5.2. The two black lines correspond to the prolongations of the initial trajectories. The red arrow indicates a dispersive wave induced by the collision.

quasi-solitons as shown in Fig. 5.1(a) is (nearly) elastic, they simply exchange their positions, while retaining their individual power. This situation retains much of the dynamics from the $\beta_3 = 0$ case. In contrast, in Fig. 5.1(b), we see that after collision three pulses emerge: an early, much weaker quasi-soliton ($\sim 24\text{W}$), a later very high power quasi-soliton ($\sim 245\text{W}$), and a final, very weak and dispersive wave ($\sim 0.002\text{W}$) — the collision is highly inelastic. We note that this process is similar to what was described in Refs.[22–25] for other NLSE variants. We emphasize that although the dispersive wave is fundamental for the energy transfer, its peak power is more than 4 orders of magnitude smaller than the soliton powers.

Systematically studying many of such collisions, we find that the relative energy transfer as function of the phase difference ϕ can be modeled quite accurately with the formula

$$\frac{\Delta E_1}{E_2} = A \sin^2\left(\frac{\phi - \phi_o}{2}\right), \tag{5.2}$$

where ΔE_1 is the amount of energy absorbed by the larger quasi-soliton, E_2 is the energy of the smaller quasi-soliton, ϕ_0 is the phase difference for which the gain has a minimum and the parameter A is the maximum value for the ratio $\Delta E_1/E_2$. In order to determine the energy transfer we estimate the individual pulse energies in the gNLSE via $\int_{\Delta t} |u(z,t)|^2 dt$ with $\Delta t = 1\text{ps}$ symmetric with respect to the maximum peak power. The parameter A depends on the two quasi-soliton initial

values P_1, Ω_1, P_2, Ω_2 and on the fiber characteristics β_2, β_3, γ . In Fig. 5.2, we show that agreement between Eq. (5.2) and the numerical simulations is indeed remarkably good. Such agreement improves when the difference $|v_1^{-1} - v_2^{-1}|$ increases, moreover the parameter A decreases with $|v_1^{-1} - v_2^{-1}|$ (A is the amplitude of the curves in Fig. 5.2). Although Eq. (5.2) has a simple dependence in ϕ, we do not know the dependence of A on the two quasi-soliton initial values and on the fiber characteristics. An explanation for the functional form of Eq. (5.2) will be given in section (5.3).
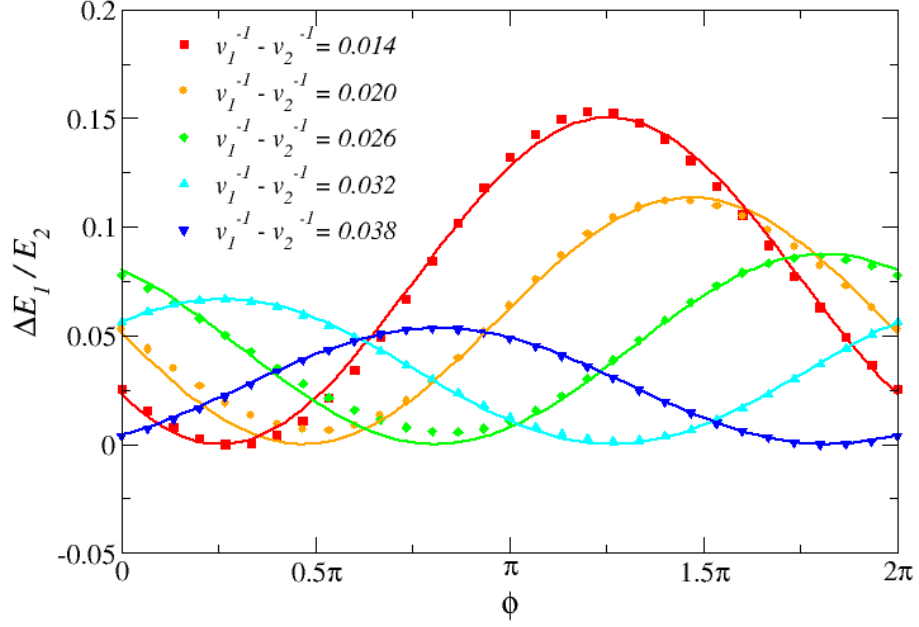
(a)
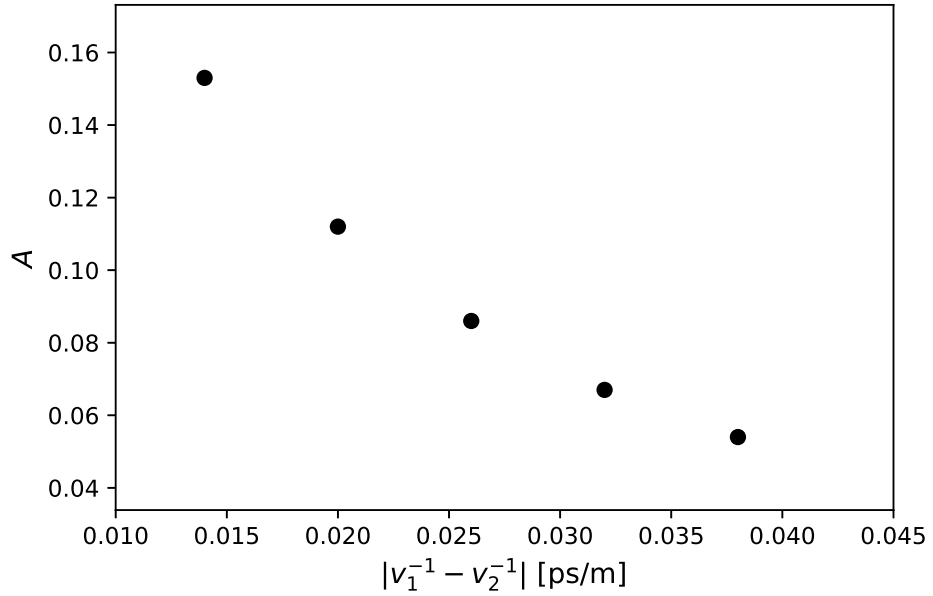
(b)

Figure 5.2: (a) $\Delta E_1/E_2(\phi)$ for various choices of initial speeds. The data points represents results obtained integrating the gNLSE (2.1) while the lines denote the fit (5.2). The red squares correspond to the energy transfer for the scattering displayed in Fig. 5.1. (b) Amplitude A of $\Delta E_1/E_2(\phi)$ as function of $|v_1^{-1} - v_2^{-1}|$.

47

5.2 Two quasi-soliton decomposition

In the following sections we discuss possible approaches to calculate the energy transfer analytically. To start with, we attempted to calculate the energy transfer ΔE_1 in the two quasi-soliton scattering by decomposing Eq. (2.1) into two coupled differential equations

$$\partial_z u_1 + i\tfrac{\beta_2}{2}\partial_t^2 u_1 - \tfrac{\beta_3}{6}\partial_t^3 u_1 - i\gamma|u_1|^2 u_1 = 2i\gamma|u_1|^2 u_2 + i\gamma u_1{}^2 u_2^*, \qquad (5.3a)$$

$$\partial_z u_2 + i\tfrac{\beta_2}{2}\partial_t^2 u_2 - \tfrac{\beta_3}{6}\partial_t^3 u_2 - i\gamma|u_2|^2 u_2 = 2i\gamma|u_2|^2 u_1 + i\gamma u_2{}^2 u_1^*, \qquad (5.3b)$$

where u_1 and u_2 are partial fields and the total optical field is given by $u = u_1 + u_2$. Karpman and Solov'ev [22] suggested a similar decomposition for a two soliton system at $\beta_3 = 0$. The idea is to write an equation for the variation of intensity $|u_1|^2$ in the form

$$\partial_z |u_1|^2 = \mathcal{G}(\beta_2, \beta_3, \gamma, P_1, \Omega_1, P_2, \Omega_2; z, t, \phi), \qquad (5.4)$$

where the function $\mathcal{G}$ represents the rate of variation. From such equation the energy transfer can be calculated as [89]

$$\Delta E_1 = \int \mathcal{G}(\beta_2, \beta_3, \gamma, P_1, \Omega_1, P_2, \Omega_2; z, t, \phi) dz dt. \qquad (5.5)$$

Unfortunately such approach does not work because after the collision the two quasi-solitons mix in the optical fields u_1 and u_2, and the mixing depends on the initial phase difference ϕ and on the other quasi-soliton parameters, that is, the partial fields u_1 and u_2 do not represent the physical pulses.

Figs. 5.3 (a) and (b) show the intensity $|u|^2$ as function of time t at distance 100m and 220m corresponding, respectively, to the elastic and inelastic scattering displayed in Fig. 5.1. In the same figure we plot the results obtained now integrating Eqs. (5.3a) and (5.3b). The intensity of the first field $|u_1|^2$ is shown in Fig. 5.3 for (c) the elastic and (d) the inelastic case. Fig. 5.3 (e) and (f) illustrate the intensity of the second field $|u_2|^2$ corresponding to the same cases of (c) and (d) respectively. As we can see for the elastic case, after the collision, the two quasi-solitons simply exchange their position in the optical fields u_1 and u_2. In the full inelastic scattering, after the

collision, both solitons go into the field u_1. We emphasize that the mixing depends on the quasi-soliton parameters in a non trivial way.
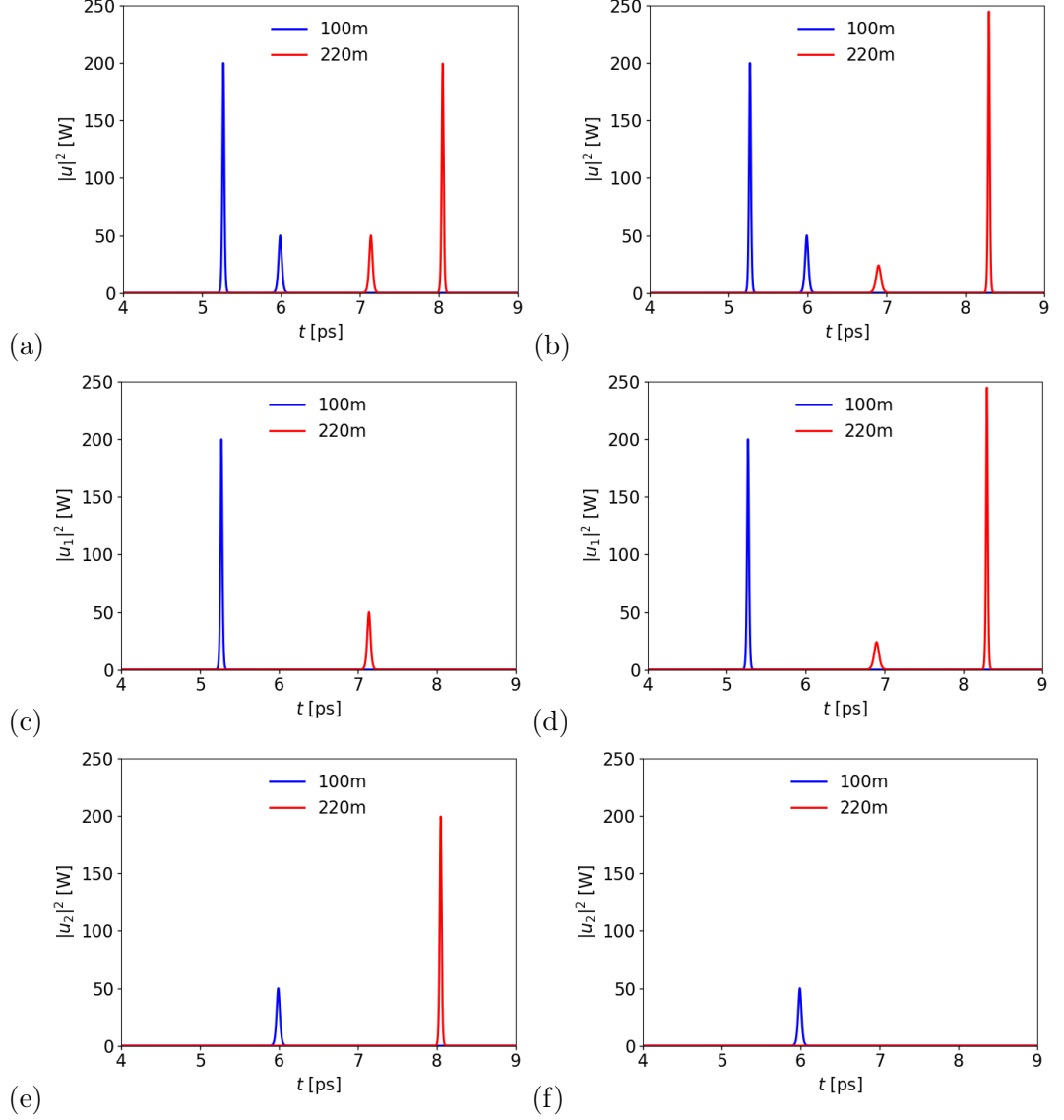
Figure 5.3: (a+b) Intensity $|u|^2$ as function of time t at distance 100m and 220m. The phase difference ϕ was chosen to correspond to (a) the minimum and (b) the maximum of $\Delta E_1 / E_2(\phi)$ plotted in Fig. 5.2. (c+d) Intensity $|u_1|^2$ for (c) elastic and (d) inelastic scattering. (e+f) Intensity $|u_2|^2$ for (e) elastic and (f) inelastic scattering.

We tried other decompositions beside (5.3a) and (5.3b) but all of them where un-

successful. For example we tried the decomposition

$$\partial_z u_1 + i\frac{\beta_2}{2}\partial_t^2 u_1 - \frac{\beta_3}{6}\partial_t^3 u_1 = i\gamma|u_1 + u_2|^2 u_1, \tag{5.6a}$$

$$\partial_z u_2 + i\frac{\beta_2}{2}\partial_t^2 u_2 - \frac{\beta_3}{6}\partial_t^3 u_2 = i\gamma|u_1 + u_2|^2 u_2, \tag{5.6b}$$

but in this case the two quasi-soliton scattering was always elastic, with no energy transfer independently of the initial phase difference. We also tried to invert the interaction in Eqs. (5.3a) and (5.3b), that is

$$\partial_z u_1 + i\frac{\beta_2}{2}\partial_t^2 u_1 - \frac{\beta_3}{6}\partial_t^3 u_1 - i\gamma|u_1|^2 u_1 = 2i\gamma|u_2|^2 u_1 + i\gamma u_2^2 u_1^*, \tag{5.7a}$$

$$\partial_z u_2 + i\frac{\beta_2}{2}\partial_t^2 u_2 - \frac{\beta_3}{6}\partial_t^3 u_2 - i\gamma|u_2|^2 u_2 = 2i\gamma|u_1|^2 u_2 + i\gamma u_1^2 u_2^*. \tag{5.7b}$$

This attempt was one of the worst because the numerical integration reaches instability after few meters of propagation. The two pulses lose completely their initial soliton shape and are dispersed in the background.

Although the decomposition approach fails to describe the two quasi-soliton scattering, Eq. (5.5) is completely general and can give some insights on the energy transfer problem.

5.3 Semi-analytical solution

In this section we will give a semi-analytical solution for the problem of two quasi-soliton energy transfer. In Fig. 5.2 we observe an energy transfer due to inelastic scattering. This energy *gain* of quasi-soliton 1 from quasi-soliton 2, can be written as

$$\Delta E_1 = \int \mathcal{G}(\beta_2, \beta_3, \gamma, P_1, \Omega_1, P_2, \Omega_2; z, t, \phi)dzdt, \tag{5.8}$$

where we have not made any assumption on the type of interaction $\mathcal{G}$. It is convenient to study the scattering in the center of mass of the two quasi-solitons, therefore we

50

use the new variables $s = t - z/v_1$, $w = t - z/v_2$. Then (5.8) becomes

$$\Delta E_1 = \frac{1}{\mid v_1^{-1} - v_2^{-1} \mid} \int \mathcal{G} \left(\beta_2, \beta_3, \gamma, P_1, \Omega_1, P_2, \Omega_2; s, w, \phi \right) ds dw. \qquad (5.9)$$

Eq. (5.9) suggests that a large difference between the (inverses of the) v_i results in a reduced energy gain for the larger quasi-soliton in agreement with the results shown in Fig. 5.2. The same figure also shows the importance of ϕ for the energy transfer. Fourier-expanding (5.9), we can write

$$\frac{\Delta E_1}{E_2} = \frac{1}{\mid v_1^{-1} - v_2^{-1} \mid} \sum_{n=0}^{\infty} \epsilon_{\beta_2, \beta_3, \gamma, P_1, \Omega_1, P_2, \Omega_2}(n) \cos \left[n(\phi - \phi_0) \right], \qquad (5.10)$$

where $\epsilon(n)$ are Fourier coefficients (we suppress indices for a moment) and ϕ_0 is the phase difference for which the gain has a minimum (as we will see later from Eq. (5.12)). The value of the phase ϕ_0, can in principle be calculated imposing that the two quasi-solitons have initial phase difference ϕ so that at the point of collision (z_0, t_0) the total phase difference is $\pi/2$ (no interference), that is

$$\phi_0 + \left[\frac{\beta_2}{2} \left(\Omega_2^2 - \Omega_1^2 \right) + \frac{\beta_3}{6} \left(\Omega_2^3 - \Omega_1^3 \right) + \frac{\gamma}{2} \left(P_2 - P_1 \right) \right] z_0 - \Omega_2 (t_0 - t_2) + \Omega_1 (t_0 - t_1) = \frac{\pi}{2}, \quad (5.11)$$

but because the superposition of the two pulses is non-linear the above formula does not predict the correct value of ϕ_0.

In order to calculate the energy transfer we approximate Eq. (5.10) with just the first two coefficients $n = 0,\ 1$. These two coefficients are related; the larger quasi-soliton always gains energy ($\Delta E_1 > 0$), hence $\epsilon(0) \geq |\epsilon(1)|$ and because for a certain ϕ the energy gain is zero, we have $\epsilon(0) = -\epsilon(1)$. Thus we can write

$$\frac{\Delta E_1}{E_2} \simeq \frac{\epsilon_{\beta_2, \beta_3, \gamma, P_1, \Omega_1, P_2, \Omega_2}}{|v_1^{-1} - v_2^{-1}|} \sin^2 \left(\frac{\phi - \phi_o}{2} \right), \qquad (5.12)$$

where we have used $1 - \cos(\phi) = 2 \sin^2 \left(\frac{\phi}{2} \right)$ and defined $\epsilon = 2\epsilon(0)$. The value of ϵ is yet undetermined while the dependence on the group velocities and the phase difference it is clear. As shown in Fig. 5.2, Eq. (5.12) provides an excellent description of the energy gain in pair-wise quasi-soliton collisions. The value of ϵ will be determined numerically in the following chapter, particularly we will study the dependence on the β_3 term. We will also show how approximation (5.12) is sufficient to generate RWs in a many quasi-soliton system. Indeed, once we know the shape

of every quasi-soliton (4.4) and how they interact (5.12), the dynamic of the system can be implemented and the PDFs can be calculated without the need of integrating the gNLSE.

Summary

In this chapter, we discussed the interaction between quasi-solitons in the gNLSE with TOD. We also derived a semi-analytical approximation to describe the energy transfer from one pulse to another. The main points of the chapter are:

- In contrast to standard solitons, quasi-solitons exchange energy when they collide. The amount of energy transfer depends on the initial phase difference between the two waves and on the other pulse parameters.

- The gNLSE with TOD can be decomposed in two equations with partial fields u_1 and u_2. Unfortunately, the partial fields u_1 and u_2 do not represent the physical pulses.

- The energy transfer during the two quasi-soliton collision can be approximated by

$$\frac{\Delta E_1}{E_2} \simeq \frac{\epsilon_{\beta_2,\beta_3,\gamma,P_1,\Omega_1,P_2,\Omega_2}}{|v_1^{-1} - v_2^{-1}|} \sin^2\left(\frac{\phi - \phi_o}{2}\right),$$

  where the the function $\epsilon_{\beta_2,\beta_3,\gamma,P_1,\Omega_1,P_2,\Omega_2}$ is to be calculated.

In the following chapter, we will make use of the results on quasi-soliton propagation and interaction to implement a cascade model that is able to generate rogue waves without the need to integrate the full gNLSE.

Chapter 6

Cascade model

In chapter 3 we discussed how the gNLSE with TOD generates RWs. In this chapter we present a cascade model that produces rogue waves without the need to integrate the full gNLSE. The model is based on the previews results found for quasi-soliton propagation and interaction. Section 6.1 introduces the cascade model with its main assumptions. In section 6.2 we discuss the initial conditions given as input for the cascade model. Section 6.3 is dedicated to the calculation of the effective coupling constant in the two quasi-soliton interaction and its dependence on the β_3 term. Finally, in section 6.4 we show the traces and PDFs generated by the cascade model and compare them with the gNLSE results.

6.1 The model

It still remains largely unknown how RWs emerge [5, 79, 80]. The results from the gNLSE in the presence of a TOD term [90, 91] suggest that quasi-solitons are created by modulation instability, then they exchange energy through inelastic scattering. Based on this observation we can now replace the full numerical integration of the gNLSE with a cascade model (CM) that tracks the collisions between quasi-solitons. The key points of such a model are

1. We assume a number of pulses, generated by modulation instability, according to the distribution of peak power

$$\rho(P) = bP_0^{-b}(P)^{b-1} \exp\left[-\left(\frac{P}{P_0}\right)^b\right], \qquad (6.1)$$

where P_0 and b are parameters fitted on the real distribution generated using the gNLSE.

2. For every quasi-soliton with index q the pulse speed is given by the pulse peak power, according to

$$v_q^{-1} = \beta_2 \Omega_q + \frac{\beta_3}{2} \Omega_q^2 + \frac{\beta_3}{6T_q^2}, \quad (6.2)$$

where

$$T_q = \sqrt{\frac{|\beta_2 + \beta_3 \Omega_q|}{\gamma P_q}}, \quad (6.3)$$

and larger pulse powers imply larger speeds (into the same direction).

3. From the speed and separation of pulses, we compute the time until the next collision.

4. At the collision point, we compute a random phase ϕ between the pulses which determines the amount of energy transferred. This is modeled using a formula similar to the particle collision process (5.12)

$$\frac{\Delta E_1}{E_2} = \frac{\epsilon_{\text{eff}}}{|v_1^{-1} - v_2^{-1}|} \sin^2\left(\frac{\phi}{2}\right). \quad (6.4)$$

Here, ΔE_1 is the energy gain for the higher energy quasi-soliton and E_2 is the energy of the second quasi-soliton involved in the collision. The group velocities at the point of collision are v_1 and v_2. Energy is only transferred towards the larger energy pulse. In Eq. (6.4), ϵ_{eff} is an empirical cross-section coefficient, it depends on β_3 and will be justified and calculated later on from the gNLSE.

5. The process then repeats until a distance of 1500m has been reached.

6. At regular distance intervals, every pulse energy can be reassociated with a soliton pulse shape,

$$u_q(z,t) = \sqrt{P_q}\, \text{sech}\left[\frac{(t - t_q) - z/v_q}{T_q}\right] \exp[i\phi_q]. \quad (6.5)$$

All such pulse shapes are sampled with a certain temporal resolution to produce instant power values along the fiber. These values are then used to compute the
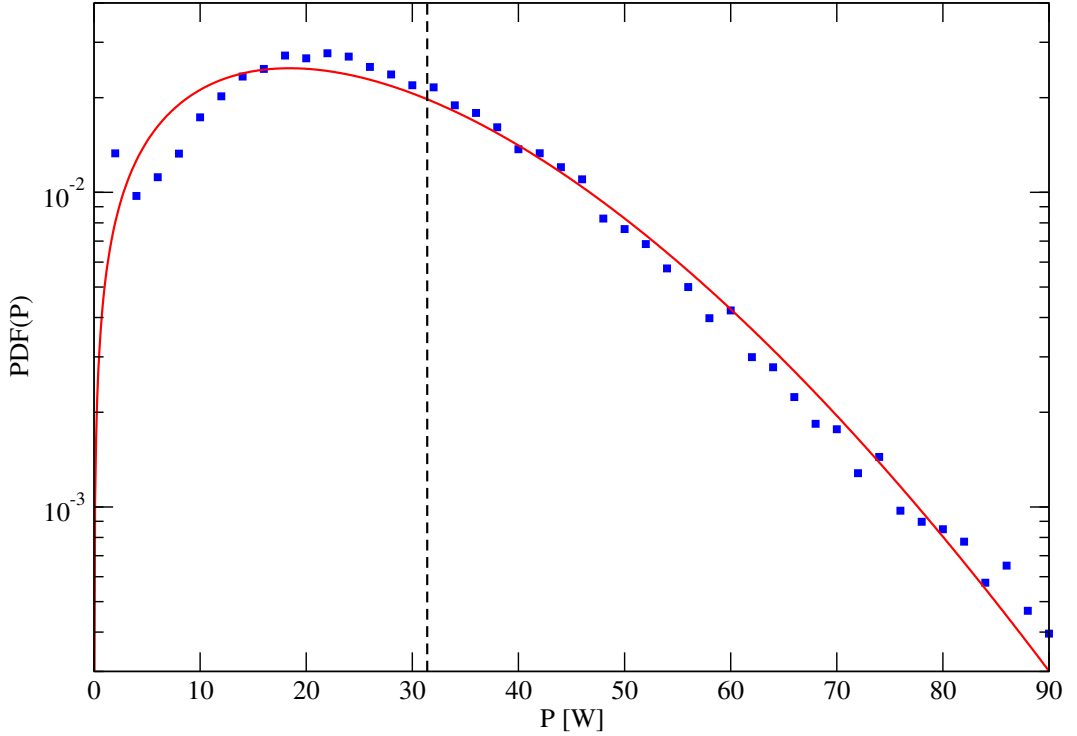
Figure 6.1: Probability density function of the peak power PDF(P) for $\beta_3 = 0$ at 1.5 km. The points (blue squares) denote the data while the solid (red) line shows the fit with Eq. (6.6). The dashed black line is at the fitted value $P_0 = 31.4$ W.

probability density function (PDF). In the following paragraphs, we will discuss the above points in more detail.

6.2 Initial conditions: PDF(P)

As initial condition for the cascade model we compute the PDF of the soliton peak power, P_q, in the gNLSE case $\beta_3 = 0$. We select a distance of $z = 1.5$km such that the system has stabilized (see inset of Fig. 3.2). We find that the resulting PDF(P_q) can be described approximately by a Weibull distribution [38]

$$\rho(P_q) = \frac{b}{P_0} \left(\frac{P_q}{P_0} \right)^{b-1} \exp \left[-\left(\frac{P_q}{P_0} \right)^b \right], \tag{6.6}$$

where $P_0 = 31.4 \pm 0.6$W and $b = 1.69 \pm 0.04$ are fitting parameters. The PDF(P_q) and its fit are shown in Fig. 6.1 . To calculate the probability distribution of the peak power we solved the NLSE and then counted all the local maxima of $|u|^2$ (see
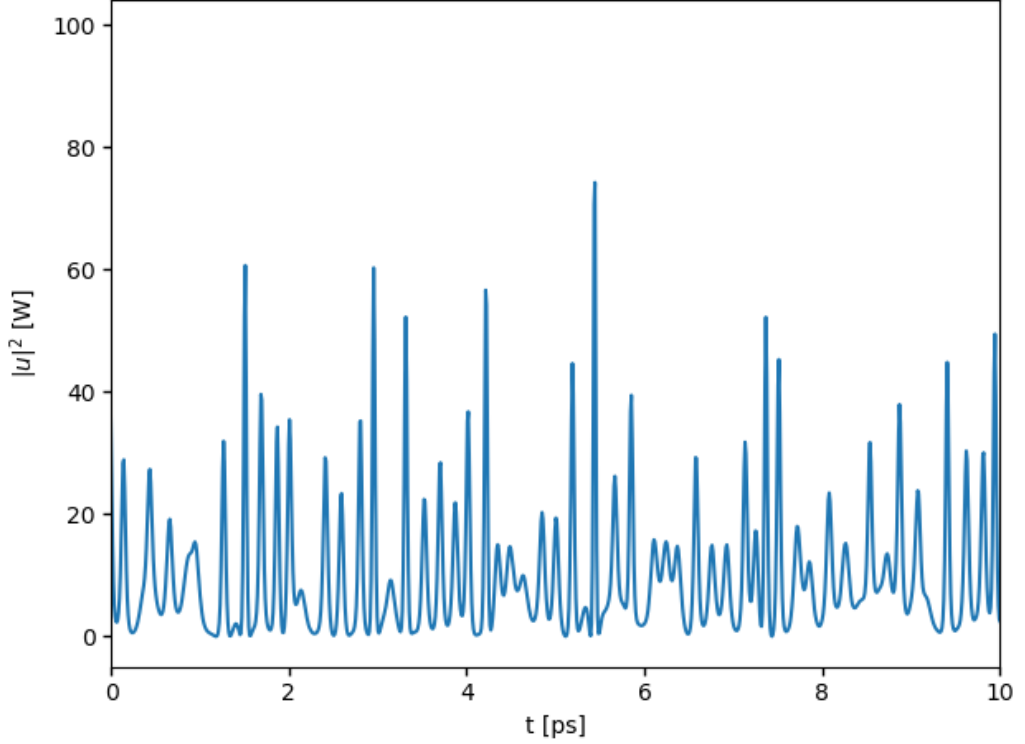
Figure 6.2: Intensity $|u|^2$ as function of time in the case $\beta_3 = 0$ at 1.5 km. The results have been generated using the NLSE.

Fig. 6.2) in bin intervals of $\triangle P = 2\mathrm{W}$. Our effective model aims to describe the soliton part of the NLSE, hence to put more emphasis on the peaks rather than the background the fit has been performed taking the log of the data and the log of the fitting function (6.6). The value P_0 can alternatively be estimated using energy conservation. Indeed we start with a continuous wave (CW) power of $P_{\mathrm{CW}} = 10\mathrm{W}$. An average time between two peaks of $\Delta T = 0.170 \pm 0.008$ ps was measured from the autocorrelation

$$\mathcal{C}_z(\tau) = \int dt' \left[|u(z,t')|^2 - \langle|u(z,t)|^2\rangle_t\right] \cdot \left[|u(z,\tau - t')|^2 - \langle|u(z,t)|^2\rangle_t\right], \qquad (6.7)$$

shown in Fig. 6.3. In the above equation $\langle\rangle_t$ denotes the time average. Hence the initial energy contained in the time window ΔT is $E_{\mathrm{init}} = P_{\mathrm{CW}}\Delta T = 1.70$ pJ. At distances when quasi-solitons have been created the average energy contained in ΔT, using Eq. (6.3) and Eq. (6.6), is
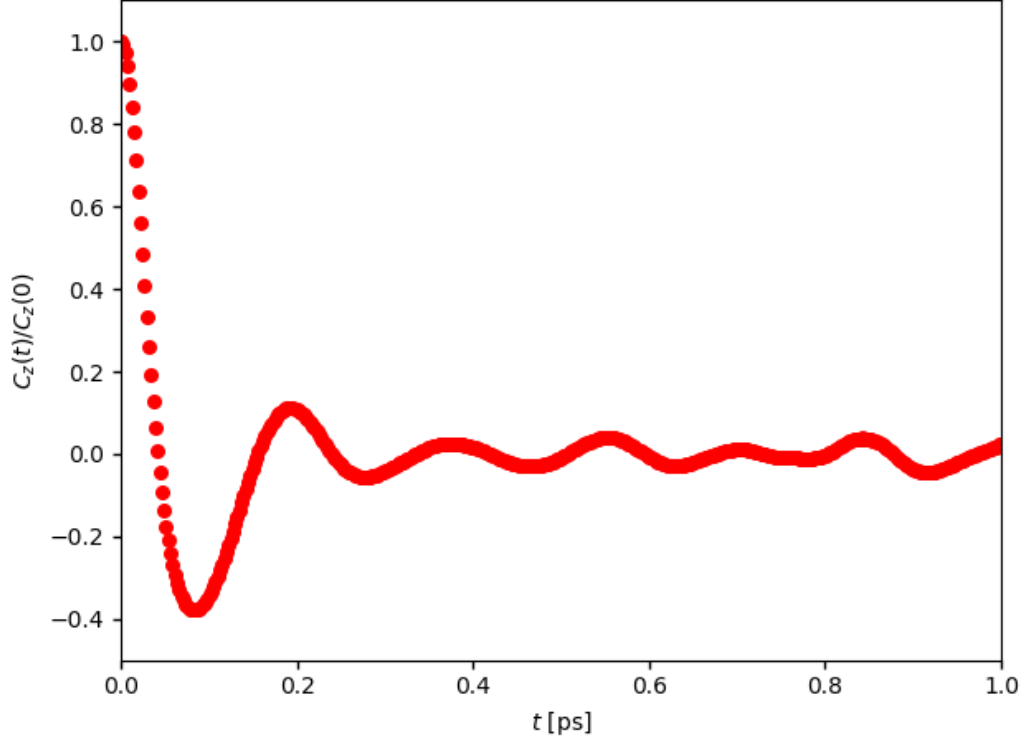
Figure 6.3: Normalized time autocorrelation $\mathcal{C}_z(t)/\mathcal{C}_z(0)$ for the NLSE in the case $\beta_3 = 0$ at 1.5 km. $\mathcal{C}_z(t)$ is calculated using Eq. 6.7.

$$E_{\text{final}} = \int_0^\infty 2P_q T_q(P_q)\rho(P_q)dP_q \simeq 1.796\sqrt{\frac{|\beta_2|P_0}{\gamma}}. \tag{6.8}$$

From energy conservation, $E_{\text{final}} = E_{\text{init}}$, we find

$$P_0 \simeq \frac{\gamma}{|\beta_2|}\left(\frac{P_{\text{CW}}\Delta T}{1.796}\right)^2 = 34 \pm 3\text{W}. \tag{6.9}$$

This is in agreement with the value $P_0 = 31.4 \pm 0.6$W found from the fit (6.6). Note that the initial conditions have been calculated from the case $\beta_3 = 0$ because for $\beta_3 \neq 0$ the previous procedure is not possible. For $\beta_3 \neq 0$ the intensity has a noisy signal of radiation in the background [28]. This radiation shows many local maxima that are wrongly counted as solitons, therefore the calculated PDF(P_q) is not exploitable to implement the CM (the CM describes the soliton part of the optical field).

6.3   Interaction: ϵ_{eff} calculation

In addition to the initial conditions for our effective model, we also need to know the amount of energy transfer in the two quasi-soliton collision. In chapter 5 we showed that most of the physics underlying the interaction can be captured by considering the simple formula (5.12). The value of ϵ is yet undetermined while the dependence on the group velocities and the phase difference it is clear. As shown in Fig. 5.2, Eq. (5.12) provides an excellent description of the energy gain in pair-wise quasi-soliton collisions. The parameter $\epsilon_{\beta_2,\beta_3,\gamma,P_1,\Omega_1,P_2,\Omega_2}$ depends on seven quantities, the individual power and frequency shift of each quasi-soliton pair and the three constants that characterize the fiber. We want to model a system of many colliding quasi-solitons as shown in Fig. 3.4(a). In order to devise a tractable model, $\epsilon_{\beta_2,\beta_3,\gamma,P_1,\Omega_1,P_2,\Omega_2}$ is replaced with an effective ϵ_{eff} that describes the average properties of the interaction. Our effective energy transfer becomes (6.4). To calculate ϵ_{eff} we choose a distance $z = 500$m. At such length, well-developed quasi-soliton pulses exist (see traces in Fig. 3.4(a)), but the situation is not yet RW dominated as shown in the PDF in Fig. 3.2. We then use a trial value for ϵ_{eff} and apply Eq. (6.4) to all quasi-soliton collisions in the cascade model and compute the PDFs. The calculation is repeated again with another trial ϵ_{eff}. For different ϵ_{eff}, we compare the PDF created from the cascade model with the PDF obtained from the gNLSE and choose ϵ_{eff} such that the agreement is best, according to criteria defined below.

Since we are interested in RWs we want that agreement to be good in the tail region of $|u|^2 > 150$W (value beyond which the PDF shows fat tails according to Fig. 3.2), for this reason we "give a weight" to the PDFs by taking their logarithm. We therefore define the relative variance

$$r(\epsilon_{\text{eff}}) = \frac{\sum_i \left[\log \text{PDF}_{\text{gNLSE}}(|u_i|^2) - \log \text{PDF}_{\text{CM}}(|u_i|^2, \epsilon_{\text{eff}})\right]^2}{\sum_i \log \left[\text{PDF}_{\text{gNLSE}}(|u_i|^2)\right]^2} \qquad (6.10)$$

and minimize it with respect to ϵ_{eff} as shown in Fig. 6.4. The ϵ_{eff} at minimum is our estimate with accuracy $\epsilon_{\text{eff}}\sqrt{r(\epsilon_{\text{eff}})}$. To further stress the link between energy transfer and β_3, in Fig. 6.5 we have plotted ϵ_{eff} calculated using this variance minimization (red line) for the different β_3 values.

As a second test, we perform a Kolmogorov-Smirnov (KS)-like two-sample test [38] between the $|u|^2$ histograms of the gNLSE and the CM. As we are looking at rare events the standard KS is not suitable to compare the tails of distributions. For this
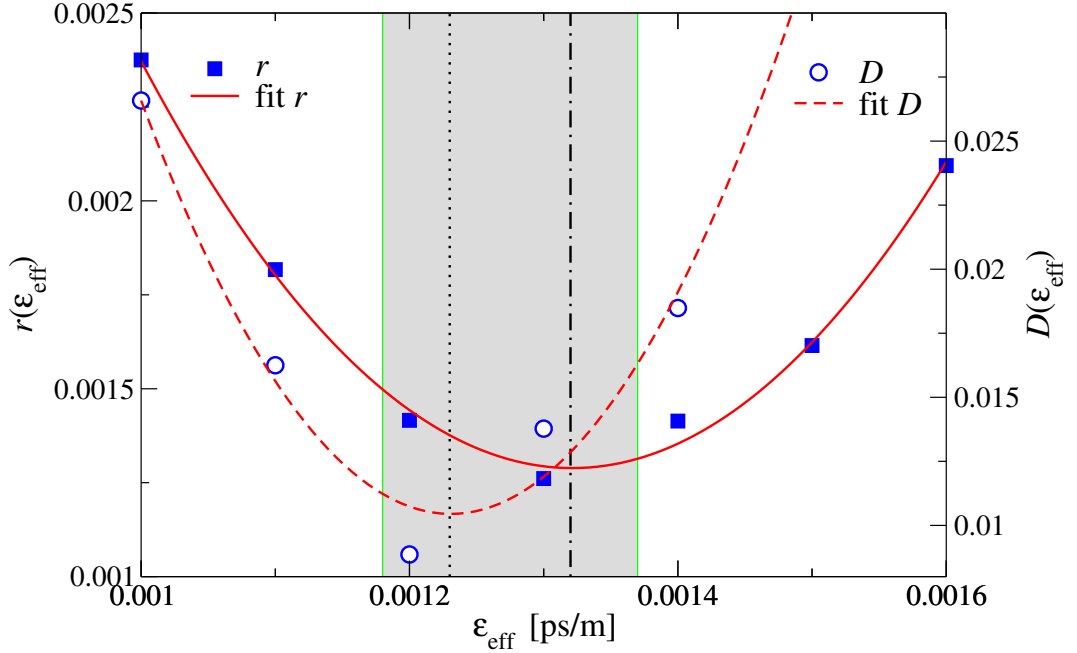
Figure 6.4: Relative variance r (filled squares) and largest difference D (open circles) calculated for different values of ϵ_{eff} at $\beta_3 = 2.64 \times 10^{-42}\mathrm{s}^3\mathrm{m}^{-1}$. Parabolic fits to the data are shown as lines. The vertical dashed-dotted line denotes the estimated $\epsilon_{\mathrm{eff}} = (1.23 \pm 0.05)\mathrm{fs/m}$ at which r is minimal, the gray region indicates the error of that estimate. The vertical dotted line denotes the estimate $\epsilon_{\mathrm{eff}} = (1.32 \pm 0.05)\mathrm{fs/m}$ from D.

purpose we renormalize the data count as $\widetilde{N}_i = \log(1 + N_i)$ with each i denoting a $|u_i|^2$ bin and overall $\widetilde{N} = \sum_{i=1}^{N_{\mathrm{bins}}} \log(1 + N_i)$. Hence the effective number of data is given by

$$\widetilde{N}_e = \frac{\widetilde{N}_{\mathrm{gNLSE}}\widetilde{N}_{\mathrm{CM}}}{\widetilde{N}_{\mathrm{gNLSE}} + \widetilde{N}_{\mathrm{CM}}}. \tag{6.11}$$

Following the KS prescription, we calculated the cumulative density functions given by

$$\mathrm{CDF}(i) = \frac{\sum_{j=1}^{i} \log(1 + N_j)}{\sum_{j=1}^{N_{\mathrm{bins}}} \log(1 + N_j)} \tag{6.12}$$

and minimize the quantity

$$D = \max_{i \in [1, N_{\mathrm{bins}}]} |\mathrm{CDF}_{\mathrm{gNLSE}}(i) - \mathrm{CDF}_{\mathrm{CM}}(i)| \tag{6.13}$$

with respect to ϵ_{eff} as shown in Fig. 6.4. As usual, with $\lambda = (\sqrt{\widetilde{N}_e} + 0.12 + 0.11/\sqrt{\widetilde{N}_e})D$, a KS-like accuracy can be given as

$$Q_{\text{KS}}(\lambda) = 2\sum_{j=1}^{\infty}(-1)^{j-1}e^{-2j^2\lambda^2}, \tag{6.14}$$

although it should no longer be interpreted probabilistically since the data count have been transformed according to $N_i \rightarrow \log(1+N_i)$. The results for ϵ_{eff} calculated using this KS-like test are also shown in Fig. 6.5 with Q_{KS} given for each β_3 value. In Fig. 6.4, we show the ϵ_{eff} dependence of the test while Fig. 6.6 displays the CDFs. We have checked that similar results for ϵ_{eff} can be obtained by using $z = 400$m and $z = 600$m as the starting point of the analysis (we observed variations of less than 4% in ϵ_{eff}). The value $z = 500$m was chosen because for smaller distances RWs are not well-developed, conversely lager distances were not used because we wanted to predict RW behavior for $z > 500$m.

Once ϵ_{eff} is determined, we use it to compute the results for the cascade model, starting at $z = 100$m and "propagating" all the way to 1500m. We emphasize the good agreement of the PDFs for $z \neq 500$m. As shown in Fig. 6.5 ϵ_{eff} depends on β_3. The transition from a regime without RWs to a regime with well pronounced RWs appears rather abrupt. RWs emerge when β_3 is large enough as shown in Fig. 6.5. Their appearance is very rapid in a short range $0.8 \lesssim \beta_3/2.64 \times 10^{-42}\text{s}^3\text{m}^{-1} \lesssim 1$. This can be understood as follows: the dispersion relation, in the moving frame, is

$$\beta(\omega) = \frac{\beta_2}{2}(\omega - \omega_0)^2 + \frac{\beta_3}{6}(\omega - \omega_0)^3. \tag{6.15}$$

The anomalous dispersion region of $\beta(\omega) < 0$, with soliton-like excitations, ends at

$$\omega_c - \omega_0 \geq -3\frac{\beta_2}{\beta_3} \tag{6.16}$$

beyond which $\beta(\omega) \geq 0$ and dispersive waves emerge, ω_c is the critical frequency at which the transition happens. From Eq. (6.3), we can estimate the typical RW spectral width as

$$2(\omega_c - \omega_0) = 2\pi\sqrt{\frac{\gamma P}{|\beta_2|}}. \tag{6.17}$$

This leads to the condition

$$\beta_3 \geq \frac{3|\beta_2|}{\pi}\sqrt{\frac{|\beta_2|}{\gamma P}} \approx 0.9 \times (2.64 \times 10^{-42})\text{s}^3\text{m}^{-1}, \tag{6.18}$$
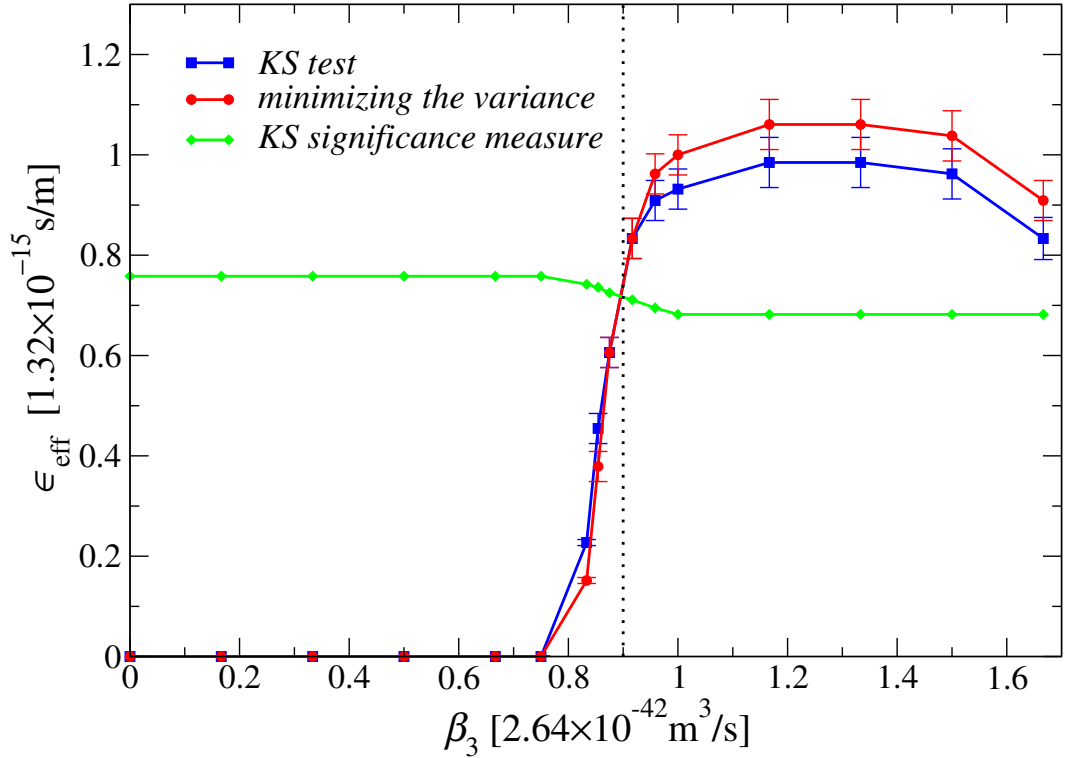
Figure 6.5: Effective coupling ϵ_{eff} values obtained comparing the PDF from the gNLSE and the cascade model at distance $z = 500$m. Results for ϵ_{eff} calculated using this variance minimization (red line), using the modified version of the KS test (blue line) and the corresponding significance (green line). The black dotted line indicates the prediction (6.18).

which is in very good agreement with the numerical result of Fig. 6.5. In Eq. (6.18) the β_3 threshold that leads to fibers supporting RWs depends on the peak power P. In deriving the numerical estimate in (6.18) we have used an initial RW power $P \sim 50$W as appropriate after about ~ 100m (see Fig. 6.2). Once such initial, and still relatively weak RWs have emerged, the condition (6.18) will remain fulfilled upon further increases in P due to quasi-soliton collisions, indicating the stability of large-peak-power RWs. Our estimation of the effective energy-transfer cross-section parameter ϵ_{eff} can of course be improved. However, we believe that Eq. (6.4) captures the essential aspects of the quasi-soliton collisions already very well.

Figure 6.6: CDFs for for the gNLSE (blue line) and for the cascade model (red line) calculated for $\beta_3 = 2.64 \times 10^{-42}\text{s}^3\text{m}^{-1}$ using the modified version of the KS test. The dashed black line at 365.75 W corresponds to the value D .
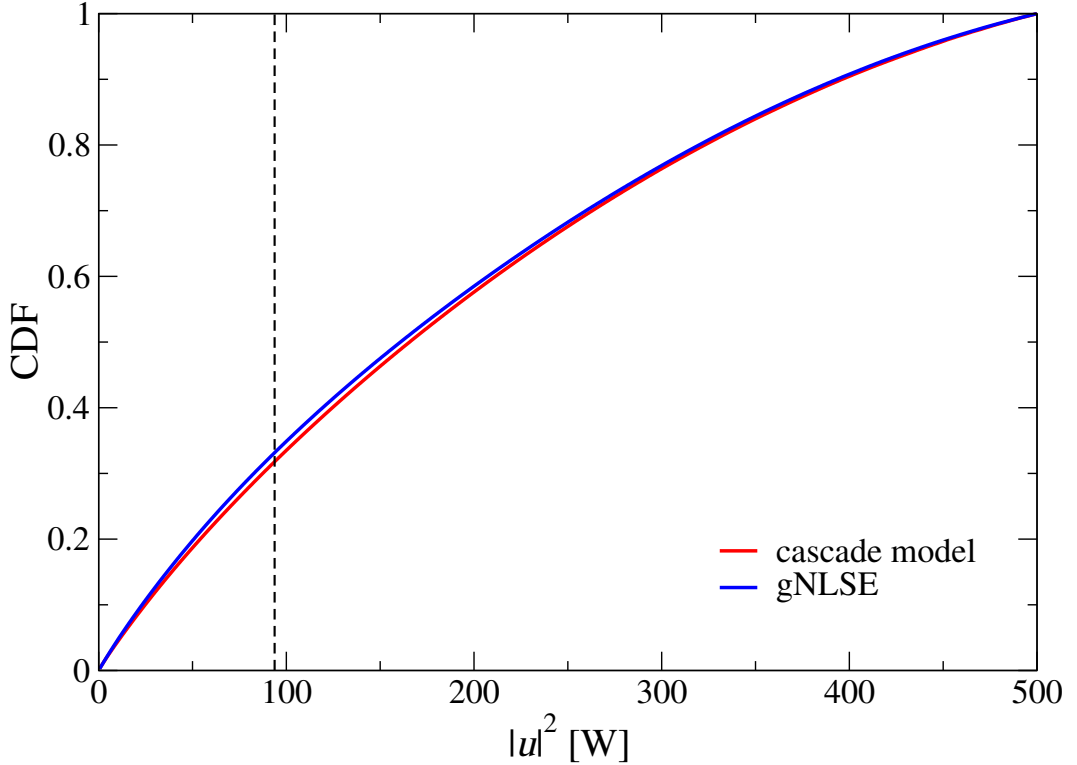
6.4 Traces and PDFs

In Fig. 6.7 we show a representative result — a selected 15ps time range out of the full $\sim 5 \times 10^6$ ps of $|u(z, t)|^2$ calculated using the cascade model. As our initial condition we generated a list of quasi-solitons by randomly choosing the power levels P_q in accordance with the statistics found in Eq. (6.6). The phases ϕ_q are drawn randomly from a uniform distribution in the interval $[0, 2\pi]$ and the frequency shifts Ω_q have been optimized, with the same procedure used for ϵ_{eff}, at the value $\Omega_q = -0.1\sqrt{\frac{\gamma P_q}{\beta_2}}$. The density of quasi-solitons is $\rho = 1/\Delta T = 5.88(\text{ps})^{-1}$, namely the inverse of the average time between two peaks observed in the correlation function ($\Delta T = 0.17\text{ps}$ is the average distance between two peaks in Fig. (6.3)). In the gNLSE quasi-solitons emerge around 100m, to mimic this the cascade model only generates data from 100m onwards. As can be seen in Fig. 6.7 the small initial differences in the pulse powers and velocities leads to eventual collisions of neighbouring pulses. Most collisions are *inelastic* and energy is transferred from the quasi-soliton with less energy

to the one with more energy leading to a cascade of incremental gains for the more powerful quasi-soliton. Initial differences in energy of quasi-solitons become exacerbated over time and larger and larger quasi-solitons emerge. These accumulate the energy of the smaller ones to the point that the smaller ones eventually vanish into the background. In addition, the group velocity of a quasi-soliton with third-order dispersion is dependent on the power of the quasi-soliton. Thus, the emerging powerful quasi-solitons feature a growing group velocity difference to their peers. This increases their collision rate but because of Eq. (6.4) the energy transfer diminishes and the process of RW formation tends to slow down. The relatively few remaining, soliton-like pulses at 1500m can have peak powers exceeding 1000W. They are truly self-sustaining rogues that have increased their power values by successive interactions and energy exchange with less powerful pulses. Solving the CM is much faster than the numerical integration of the gNLSE. Indeed, as we saw in chapter 3 solving the gNLSE for $\sim 17 \times 10^6$ pulses requires a total run time of ~ 30years $\sim 1.6 \cdot 10^7$minutes whereas for the CM we need a total run time of just $\sim 3 \cdot 10^2$minutes. The CM algorithm is a factor $\sim 5 \cdot 10^4$ faster than the split-step Fourier method, if both algorithms are run on a single machine. The reason for this huge difference is that, in the gNLSE simulation, for every step in space we need to calculate two times a fast Fourier transform ($\hat{F}$ and $\hat{F}^{-1}$) for the full time window. This requires much more time than the CM approach where we just change the energy of two solitons when they collide. Naturally the parellalized split-step Fourier algorithm can be faster than the CM algorithm if an appropiate number of processors is used.

The PDF for the complete set of $\sim 30 \times 10^6$ pulses propagating over 1500m is shown in Fig. 6.8. At 100m, the PDF shows a roughly exponential distribution. After 500m, a clear deviation from an exponential distribution has emerged and beyond 1000m, the characteristic L-shape of a fully-developed RW PDF has formed. Starting with an average power of 10W after 1.5Km there is a probability of $\sim 2 \times 10^{-6}$ to find a RW with power between 999 and 1000W.

In the inset of Fig. 6.8, we compare the long tail behavior of PDFs for the CM and gNLSE. We see that the agreement for PDFs is excellent taking into account that we have reduced the full integration of the gNLSE to only discrete collision events between quasi-solitons. The essence of the emergence of RWs in this system is very well captured by a cascade increment of quasi-soliton power due to inelastic collisions. We find that the results of the full gNLSE integration and the cascade model exhibit
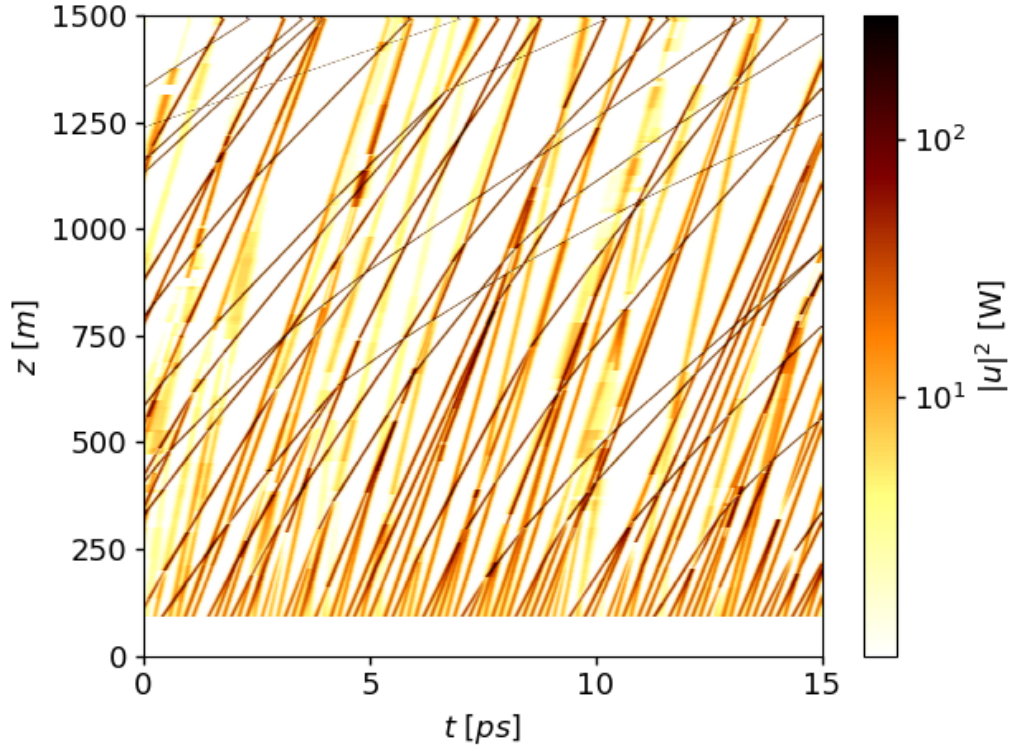
Figure 6.7: Intensity $|u(z,t)|^2$ for $\beta_3 = 2.64 \times 10^{-42}\mathrm{s}^3\mathrm{m}^{-1}$ of the effective cascade model as function of the time t and distance z in a selected time frame of $\Delta t = 15\mathrm{ps}$ and distance range $\Delta z = 1.5\mathrm{km}$. Note that we start the effective model at $z_0 = 100\mathrm{m}$ to mimic the effects of the modulation instability in the gNLSE.

the same quantitative, long-tail PDF. This agreement highlights the importance of (i) a resonance-like two-soliton scattering coupled with (ii) quasi-soliton energy exchange in giving rise to RWs.
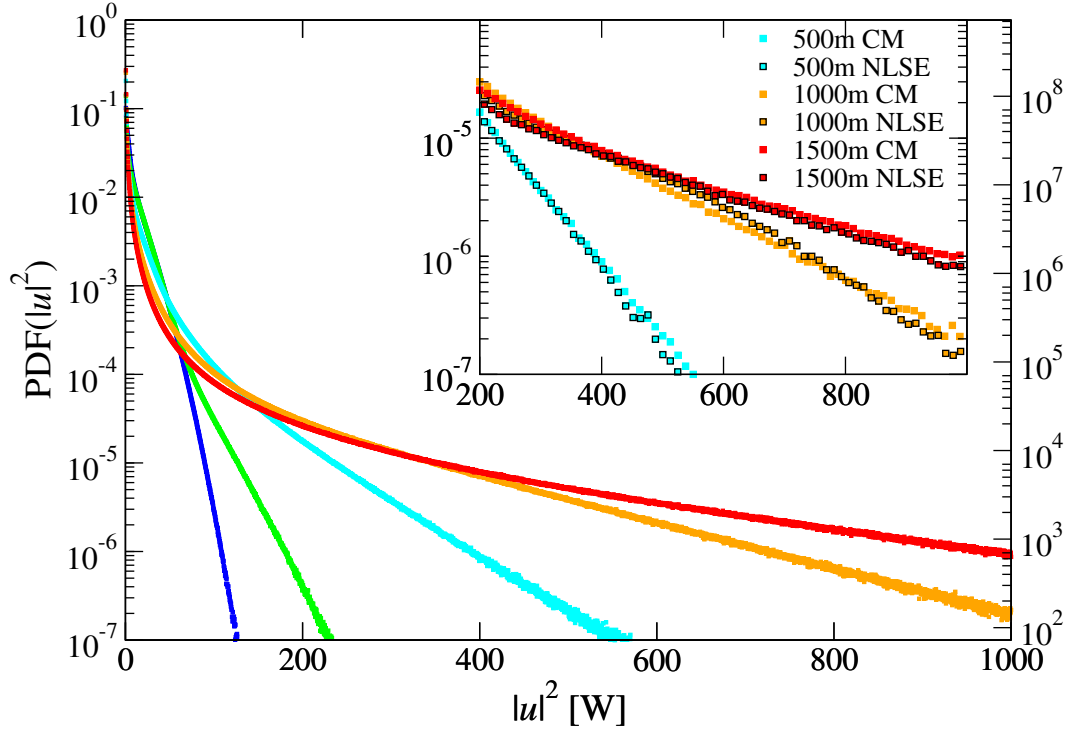
Figure 6.8: PDFs of the intensity $|u|^2$ from the the cascade model at $\beta_3 = 2.64 \times 10^{-42}\text{s}^3\text{m}^{-1}$. The PDFs have been computed at distances $z = 100\text{m}$, 200m, 500m, 1000m and 1500m. The left vertical axis denotes the values of the normalized PDF while the right vertical axis gives the event count per bin. The inset shows a comparison between the results from the gNLSE (colored lines) and the cascade model (black lines and symbol outlines) for $z = 500\text{m}$, 1000m and 1500m. Only every 50th symbol is shown.

Summary

In this chapter, we proposed a cascade model for quasi-solitons with TOD, that is able to generate RWs without the need of integrating the full gNLSE. The key points of the chapter are:

- The cascade model require initial conditions that are taken from the gNLSE integration. The initial probability density function of the peak power can be modeled as

$$\rho(P_q) = \frac{b}{P_0}\left(\frac{P_q}{P_0}\right)^{b-1}\exp\left[-\left(\frac{P_q}{P_0}\right)^b\right],$$

where $P_0 = 31.4 \pm 0.6\text{W}$ and $b = 1.69 \pm 0.04$ are fitting parameters. The initial time distance between two quasi-solitons was measured to be

65

$\Delta T = 0.170 \pm 0.008$ ps.

- The cascade model is implemented using an effective energy transfer

$$\frac{\Delta E_1}{E_2} = \frac{\epsilon_{\text{eff}}}{|v_1^{-1} - v_2^{-1}|} \sin^2\left(\frac{\phi}{2}\right),$$

where the effective coupling ϵ_{eff} is calculated numerically.

- The effective coupling ϵ_{eff} presents an abrupt transition from a regime without RWs to a regime with well pronounced RWs.

- The full gNLSE integration and the cascade model give the same quantitative long-tail PDFs.

Chapter 7

Further details and applications of the cascade model

In the previous chapter we showed that the cascade model generates rogue waves. In this chapter we present further results and details of the model. Section 7.1 is dedicated to the effect of "calm before the storm" observed in both the CM and the gNLSE. In section 7.2 we compare the autocorrelation functions of the two models. The probability to become a rogue wave, calculated using the CM, is shown in section 7.3. Finally, in section 7.4 we discuss some attempts to fit rogue wave PDFs with analytical functions.

7.1   Calm before the storm

RWs appear suddenly and can cause transmission errors and damage in optical communication systems [7]. It is therefore important to characterize RW predictability [15]. Looking more closely at the temporal vicinity of waves with particularly large power values, we find that these tend to be preceded by a time period of reduced power values. This "calm before the storm" phenomenon [15] can be observed in Fig. 7.1. In Fig. 7.1(a) we can clearly see an asymmetry in the normalized power $\langle |u(\Delta t)|^2 \rangle_{RW} / \langle |u(\Delta t)|^2 \rangle_{All}$ relative to the RW event at $\Delta t = 0$ ($\Delta t < 0$ denotes events before the RW). The average $\langle |u(\Delta t)|^2 \rangle_{RW}$ includes RWs, defined here as large power events above a threshold of 150W and also two independent simulations of the gNLSE, both with parameters as in Fig. 3.4. The value $\langle |u(\Delta t)|^2 \rangle_{All}$ is the average intensity of the full time window of integration (constant value of 10W).
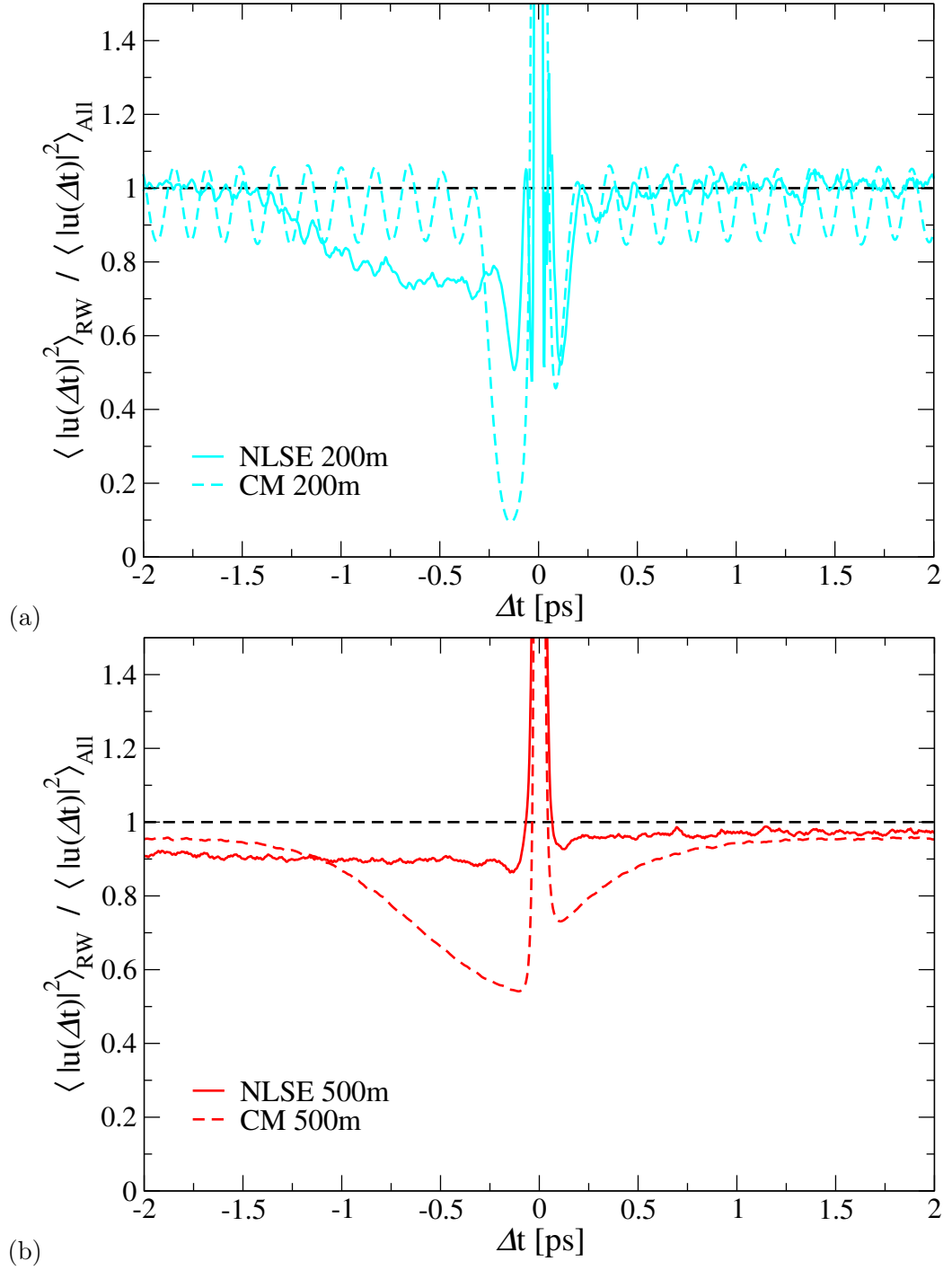
Figure 7.1: Normalized averaged powers $\langle |u(\Delta t)|^2 \rangle_{RW} / \langle |u(\Delta t)|^2 \rangle_{All}$ for times Δt in the vicinity of a RW event at $\Delta t = 0$. Panel (a) and (b) correspond to distances of 200m and 500m, respectively. Solid lines in both panels indicate averaged results for two gNLSE runs (with parameters as in Fig. 3.4), while dashed lines show the corresponding results for the cascade model. In both panels, we identify RWs as corresponding to powers equal to or larger than 150W.

The period of calm in power before the RW occurs lasts about $\Delta t = 1.5$ps at $z = 200$m. It broadens for larger distances, but an asymmetry is retained even at 500m. Physically, this effect can be understood as follows: a RW moves more slowly than the non-RW solitons. Upon interaction with a soliton, the RW gains in energy, but due to Eq. (6.3) and Eq. (6.2), slows down even more (see Fig. 3.4); the soliton, having overtaken the RW, has lost some of its energy, therefore leading to a reduction in intensity before the RW.

This finding is further supported by Fig. 7.1(b), where we note that the "calm before the storm", already observed for the gNLSE, is even clearer and more pronounced for the cascade model. We observe strong oscillations away from $\Delta t = 0$. These describe the simple quasi-soliton pulses which we used to model $u(t)$ in the cascade model. For the gNLSE, these oscillations are much less regular, although still visible. The time interval of the period of calm appears shorter in the cascade model while the amplitude reduction is stronger. We note that the apparently more regular oscillations in the cascade model at 200m is an artifact of our starting condition with solitons chosen perfectly equidistant at $z = 100$m to reproduce the same density as in the gNLSE.

We note that the "calm before the storm" phenomenon has meaning only in statistical terms, i.e. when the average over many events is taken. When a single event is consider, we can observe optical field fluctuations that create a period of calm not followed by a RW (false positives). The phenomenon therefore can not be used to predict RWs.

7.2 Autocorrelation function

The autocorrelation function is another quantity that allows to compare the CM with the gNLSE. Physically, it is a measure of how a signal correlates with a delayed copy of itself as a function of delay. It is useful in order to find repeating patterns such as periodic peaks of intensity. Indeed, the reshaping of the autocorrelation is related to the evolution of the field from a continuous wave to a peaked structure during propagation along the fiber. Results are summarized in Fig. 7.2. In Ref. [15], the authors studied RW events in three data sets, one from ocean waves and two based on optical devices. They compute, e.g., the time-series autocorrelation function $\mathcal{C}_z(\tau) = \int dt' \left[|u(z,t')|^2 - \langle |u(z,t)|^2 \rangle_t \right] \left[|u(z, \tau - t')|^2 - \langle |u(z,t)|^2 \rangle_t \right]$. In Fig. 7.2, we show $\mathcal{C}_z(\tau)$ for our gNLSE data as well as for the cascade model at various distances.
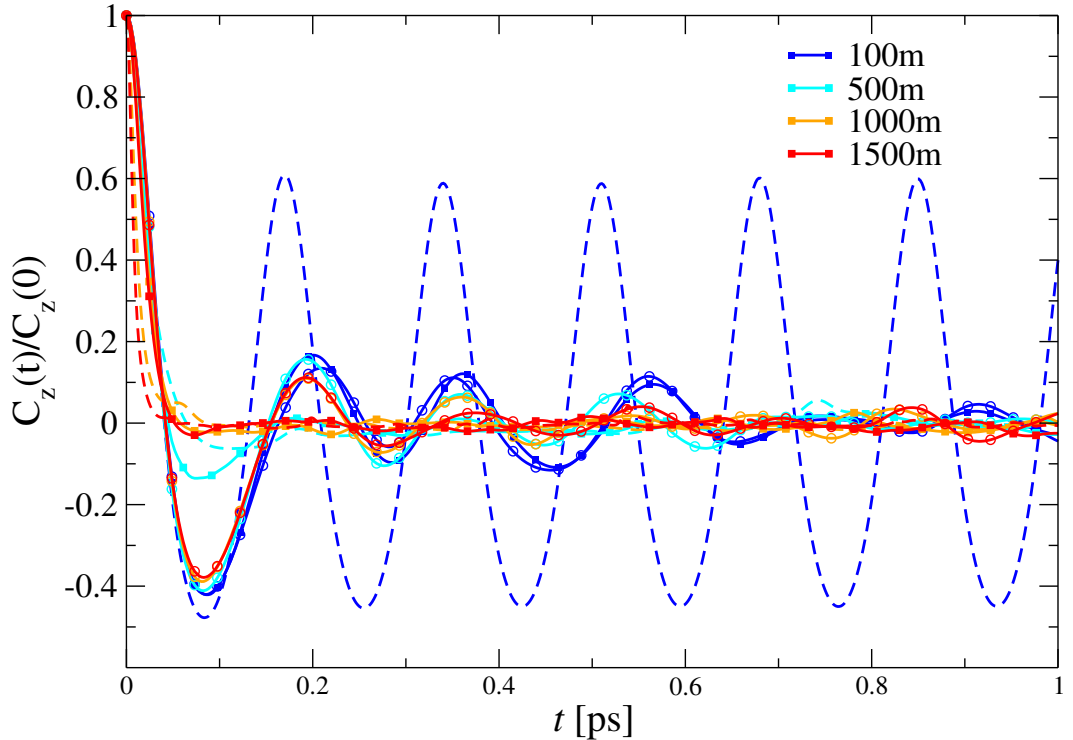
Figure 7.2: Time autocorrelation $\mathcal{C}_z(t)/\mathcal{C}_z(0)$ for the gNLSE (squares and solid lines) and for the cascade model (dashed lines) at selected z values as indicated ($\beta_3 = 2.64 \times 10^{-42} \mathrm{s}^3 \mathrm{m}^{-1}$). The circles with solid lines indicate the case $\beta_3 = 0$.

At 100m quasi-solitons are clearly correlated because of the initial conditions in both models, but from 200m onwards $\mathcal{C}_z(\tau)$ is nearly zero after a small fraction of picoseconds supporting the notion of largely independently traveling quasi-solitons that interact only when in close spatial and temporal proximity. In agreement with Ref. [15], we hence find a quick decay of $\mathcal{C}_z(t)$ after $z > 100$m which supports the notion of well-separated individual quasi-solitons (cp. Fig. 7.2). Furthermore, the agreement between gNLSE results and the cascade model is very good. Also, the correlation $\mathcal{C}_z(\tau)$ is close to what has been reported in Ref. [15].

7.3 Probability to become a rogue wave

One of the advantages of the cascade model is that we can keep track of every single quasi-soliton. For example we can look at which pulses are more likely to absorb energy from other pulses depending on their initial power. Fig. 7.3(a) shows the probability that a pulse increases its power after a certain distance z as function of
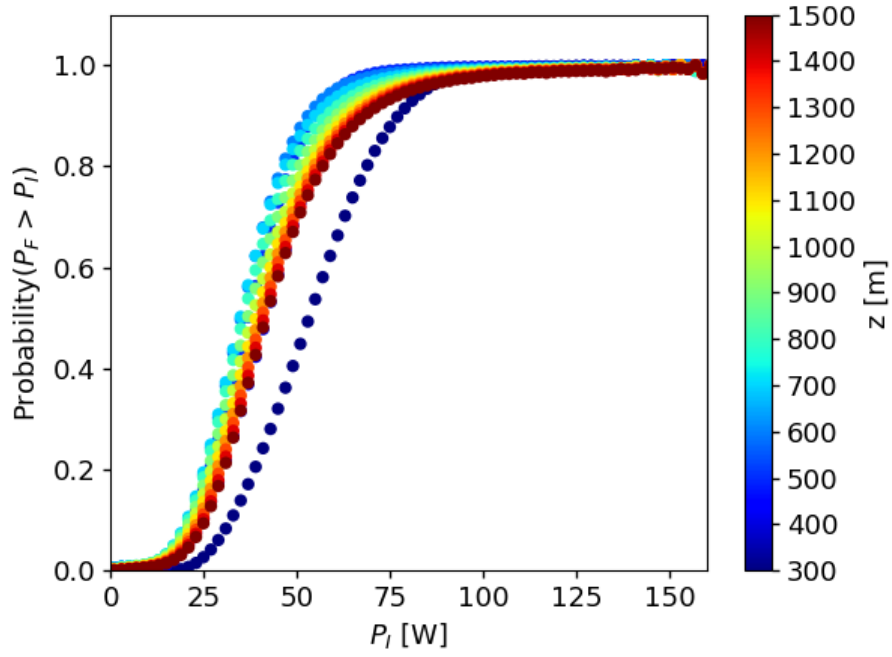
its initial power P_I measured at 100m. Such probability has a sigmoid-like shape, for low initial power it goes to zero and for high power it goes to one, at ∼44W the probability is ∼50%. The probability has been computed as

$$\text{Probability}(P_F > P_I) = \frac{N_F}{N_I}, \tag{7.1}$$

where N_I the total number of pulses with initial power in the interval $P_I \pm 1$W and N_F is the number of the ones that have increased their power after a certain distance z. The statistics has been performed with a total number of 10^9 pulses. In Fig. 7.3(b) we show the transition power P_T as function of β_3. This value corresponds to a 50% probability that a pulse increases its initial power. The power P_T grows with β_3, i.e. for large TOD only the more powerful pulses gain energy. For $\beta_3 < 0.8 \cdot 2.64 \cdot 10^{-42} \text{s}^3\text{m}^{-1}$ the effective coupling ϵ_{eff} goes to zero (see Fig. 6.5) therefore there is no energy transfer and P_T cannot be defined.

Table 7.1: Values of the coefficients a, b and F_0 needed to fit the various PDF($|u|^2$) distributions from Fig. 3.2 at three representative distances $z = 500$ m, 1000 m and 1500 m, using (W) the Weibull function of Eq. (7.2), (F) the stretched exponential of Eq. (7.4) and (P) the Pareto function as in Eq. (7.3). The reduced χ^2 value is also displayed.

Distance	Model	Fit	a [W]	$b/10^{-1}$	$F_0/10^{-3}$ [W]	χ^2
500 m	gNLSE	W	4.0 ± 0.5	4.94 ± 0.15		1
		F	9 ± 21	6 ± 3	8 ± 30	50
		P	15 ± 0.3	28 ± 2		3700
	cascade model	W	3.0 ± 0.5	4.60 ± 0.16		9
		F	12 ± 3	6.3 ± 3	6 ± 2	1060
		P	13 ± 3	26 ± 2		560
1000 m	gNLSE	W	0.9 ± 0.4	3.2 ± 0.2		4
		F	8 ± 10	47 ± 10	4 ± 5	136
		P	5.5 ± 2	15.7 ± 1.5		160
	cascade model	W	0.7 ± 0.2	3.04 ± 0.14		11
		F	11 ± 5	4.9 ± 0.4	2 ± 1	3400
		P	4.6 ± 1.5	15.1 ± 1.2		660
1500 m	gNLSE	W	0.07 ± 0.03	2.1 ± 0.1		15
		F	0.006 ± 0.001	2.1 ± 0.4	50 ± 70	240
		P	1.0 ± 0.2	10.0 ± 0.5		64
	cascade model	W	0.04 ± 0.01	1.94 ± 0.05		22
		F	0.008 ± 0.016	2.1 ± 0.3	120 ± 140	490
		P	0.55 ± 0.16	8.7 ± 0.5		6

(a)
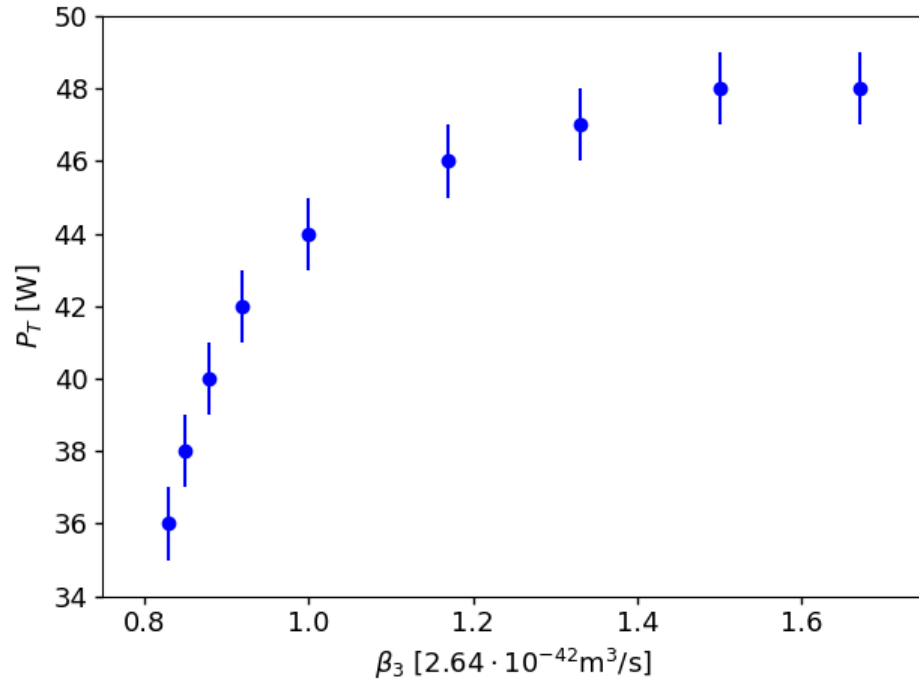
(b)

Figure 7.3: (a) Probability that a pulse increases its power after a certain distance z as function of its initial power P_I measured at 100m. The probability has been computed for $\beta_3 = 2.64 \times 10^{-42} \text{s}^3 \text{m}^{-1}$ at distances $z =$ 300m, 400m, 500m, ... , 1500m. (b) Transition power P_T that corresponds to a 50% probability that a pulse increases its power after 1500m as function of β_3.

7.4 Fitting the PDFs

In order to describe RW statistics the PDFs of Fig. 3.2 and Fig. 6.8 have been fitted with functions that typically describe L-shaped probabilities [5]. We used the Weibull function [15]

$$W(|u|^2) = ba^{-b}(|u|^2)^{b-1} \exp\left[-\left(\frac{|u|^2}{a}\right)^b\right],$$ (7.2)

and, following Ref. [64], a Pareto function

$$Q(|u|^2) = \frac{ba^b}{|u|^{2(b+1)}}.$$ (7.3)

The fits are shown in Fig. 7.4(a) for the gNLSE and Fig. 7.4(b) for the CM. Every fit has been performed taking the log of the PDF$(|u|^2)$ and the functions $W(|u|^2)$ and $Q(|u|^2)$, the resulting coefficients are in Table 7.1. Our results suggest that while a Weibull and Pareto fit are indeed possible for the tails, a systematic and consistent variation of the fitting parameters with distance traveled is not obvious. While, e.g., the PDF for 200, 500 and 1500m as shown in Fig. 3.2 appears sub-exponential in the tails, we find that the tail of the PDF for 1000m is super-exponential for $z \gtrsim 600$m. This means that typical functions, used to describe rare events, are unable to grasp the evolution of optical RW PDFs.
We also fitted the tails of PDF$(|u|^2)$ with a stretched exponential

$$F(|u|^2) = F_0 \exp\left[-\left(\frac{|u|^2}{a}\right)^b\right].$$ (7.4)

The fits are shown Fig. 7.5 from both the gNLSE and the CM. The resulting coefficients are given in Table 7.1. For all fits, the results are not convincing as documented by the rather large χ^2 values found. This hints towards a continuing development of the shape of the PDF as the propagation continues.
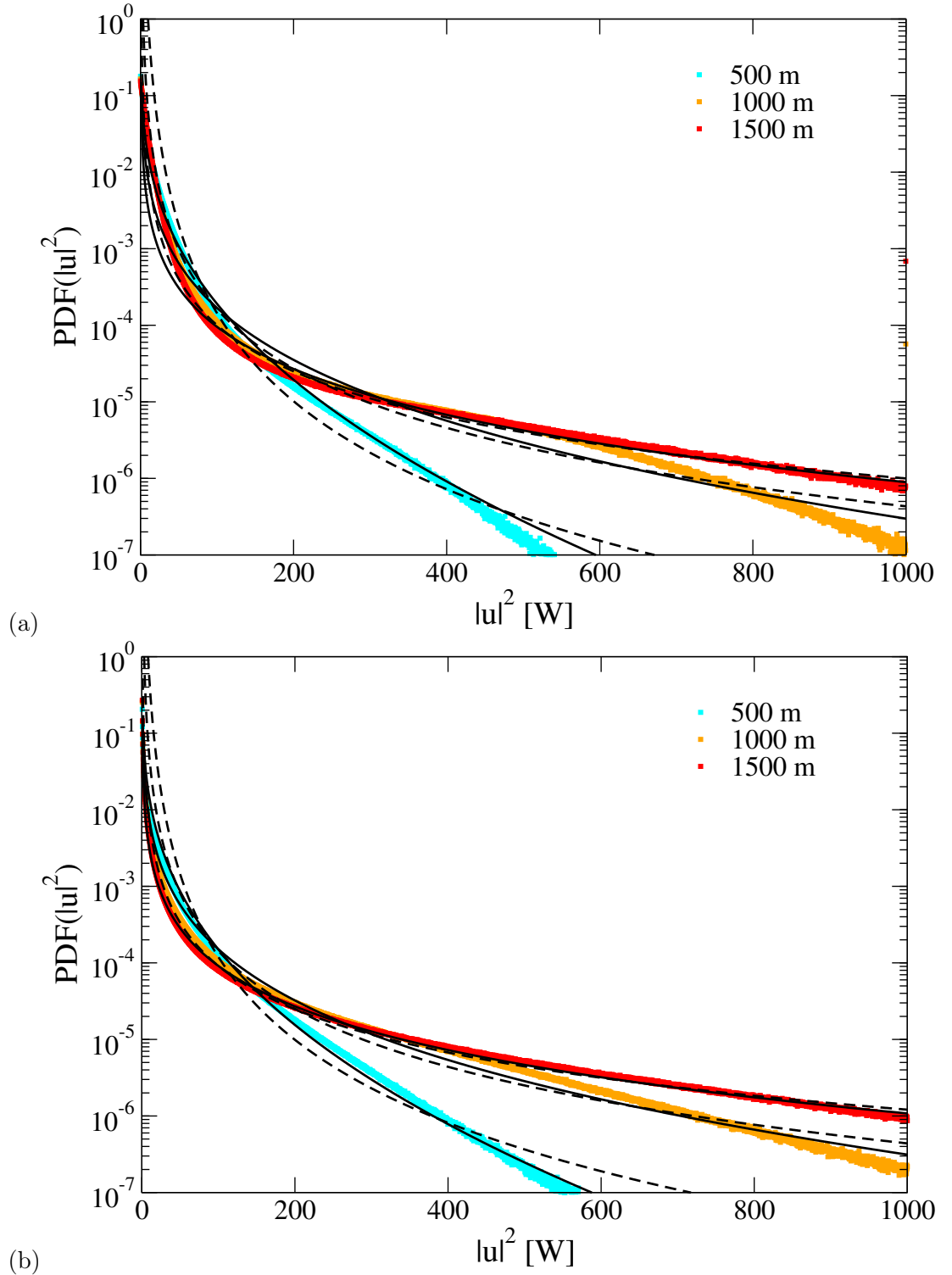
Figure 7.4: PDFs calculated for (a) the gNLSE and (b) the CM at 500, 1000 ad 1500m ($\beta_3 = 2.64 \times 10^{-42} \mathrm{s}^3 \mathrm{m}^{-1}$). The PDFs have been fitted using the Weibull function of Eq. (7.2) (full black lines) and Pareto function of Eq. (7.3) (dashed black lines).
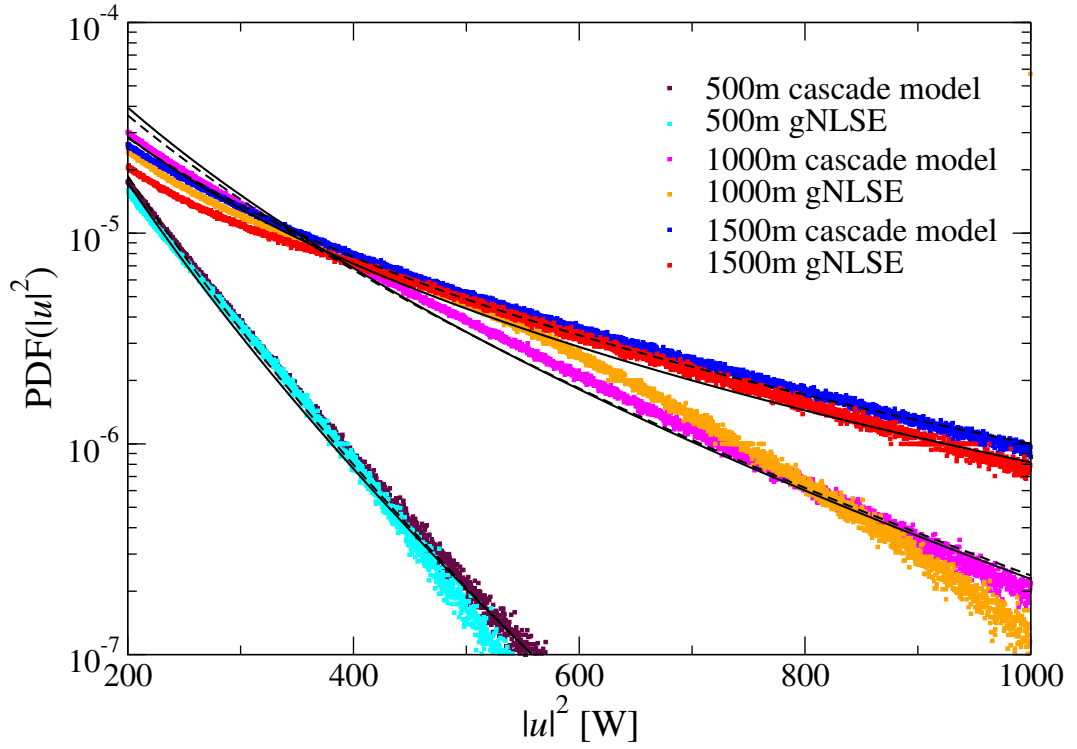
Figure 7.5: Fits for the cascade model (dashed black lines) and for the gNLSE (full black lines) PDFs using the stretched exponential of Eq. (7.4).

Summary

In this chapter, we discussed further results obtained using the cascade the model and the gNLSE. The main points of the chapter are:

- Rogue waves in both the gNLSE and the CM are preceded by a time period of reduced power values.

- After an initial reorganization quasi-solitons become uncorrelated in both the gNLSE and the CM supporting the notion that pulses interact only when in close spatial and temporal proximity.

- Using the CM we can keep track of every single quasi-soliton. We could, for example, calculate the probability that a pulse increases its power after a certain distance z as function of its initial power. Such probability has a sigmoid-like shape.

- It is possible to fit the gNLSE and CM probability density functions but the fitting parameters do not show a consistent variation with distance.

In the following chapter, we will show that the cascade model can be implemented also when quasi-solitons exchange energy through Raman interaction.

Chapter 8

Cascade Model for Raman term

In the previous chapters we have demonstrated that a simple cascade mechanism allows the formation of rogue waves in the generalized nonlinear Schrödinger equation with third-order dispersion. In this chapter we show that a similar mechanism generates rogue waves when the Raman term is considered (while $\beta_3 = 0$). Section 8.1 introduces quasi-solitons for the the gNLSE with Raman term. The energy transfer is calculated in section 8.2. In section 8.3 we discuss the initial conditions given as input for the cascade model. In section 8.4 we present the traces and PDFs generated by the cascade model and compare them with the gNLSE results. Finally, section 8.5 is dedicated to the effect of "calm before the storm" for the Raman case.

8.1 Quasi-solitons

Our starting point to study RWs with Raman interaction is the gNLSE

$$\partial_z u + \frac{i\beta_2}{2}\partial_t^2 u - i\gamma |u|^2 u + i\gamma T_R u \partial_t |u|^2 = 0, \qquad (8.1)$$

where T_R is the Raman term (see chapter 1 Eq. (1.18)), which is responsible for the pulse self-frequency shift, a linear change of the pulse frequency with the propagation distance [27].

To implement a cascade model we need to describe pulses of light in term of quasi-solitons. The solution of Eq. (8.1), similarly to the case with TOD, can be approximated as a soliton-like pulse [26]

$$u(z,t) = \sqrt{P}\text{sech}\left[\frac{t-q}{T}\right] \times \exp\left\{i\left(\frac{\beta_2}{2}\Omega^2 + \frac{\gamma P}{2}\right)z - i\Omega t - iC\frac{t^2}{2T^2}\right\}, \qquad (8.2)$$

where P, T and C represent the amplitude, duration and chirp. The other two parameters are the temporal shift q of the pulse envelope and the frequency shift Ω of the pulse spectrum. The distance-dependence of the parameters can be obtained using the momentum method [26, 87, 88]. This gives

$$\frac{dT}{dz} = \beta_2 \frac{C}{T}, \quad \frac{dC}{dz} = \left(\frac{4}{\pi^2} + C^2 \right) \frac{\beta_2}{T^2} + \frac{4\gamma P}{\pi^2},$$
$$\frac{dq}{dz} = \beta_2 \Omega, \quad \frac{d\Omega}{dz} = -\frac{8}{15} \frac{T_R \gamma P}{T^2} z. \tag{8.3}$$

The equations can be solved for $C = 0$, resulting in

$$u(z,t) = \sqrt{P} \operatorname{sech}\left[\frac{t-q}{T} \right] \exp\left[i \left(\frac{\beta_2}{2} \Omega^2 + \frac{\gamma P}{2} \right) z - i\Omega t \right], \tag{8.4}$$

with T, Ω and q given by

$$T = \sqrt{\frac{|\beta_2|}{\gamma P}}, \tag{8.5}$$

$$\Omega = -\frac{8}{15} \frac{T_R \gamma P}{T^2} z, \tag{8.6}$$

$$q = t_0 - \frac{4}{15} \frac{T_R \gamma \beta_2 P}{T^2} z^2, \tag{8.7}$$

where t_0 is the quasi-soliton initial temporal shift. Note that because Ω increases linearly with z the temporal shift q of the quasi-soliton changes quadratically with the distance. In Fig. 8.1 we compare the intensity $|u(z,t)|^2$ of a pulse against the theoretical prediction for the temporal shift Eq. (8.7). The simulation has been run for soliton peak power $P = 10\text{W}$ and Raman term $T_R = 0.0005\text{ps}$. As we can see the theoretical prediction for the temporal shift q is in good agreement with the numerical results.
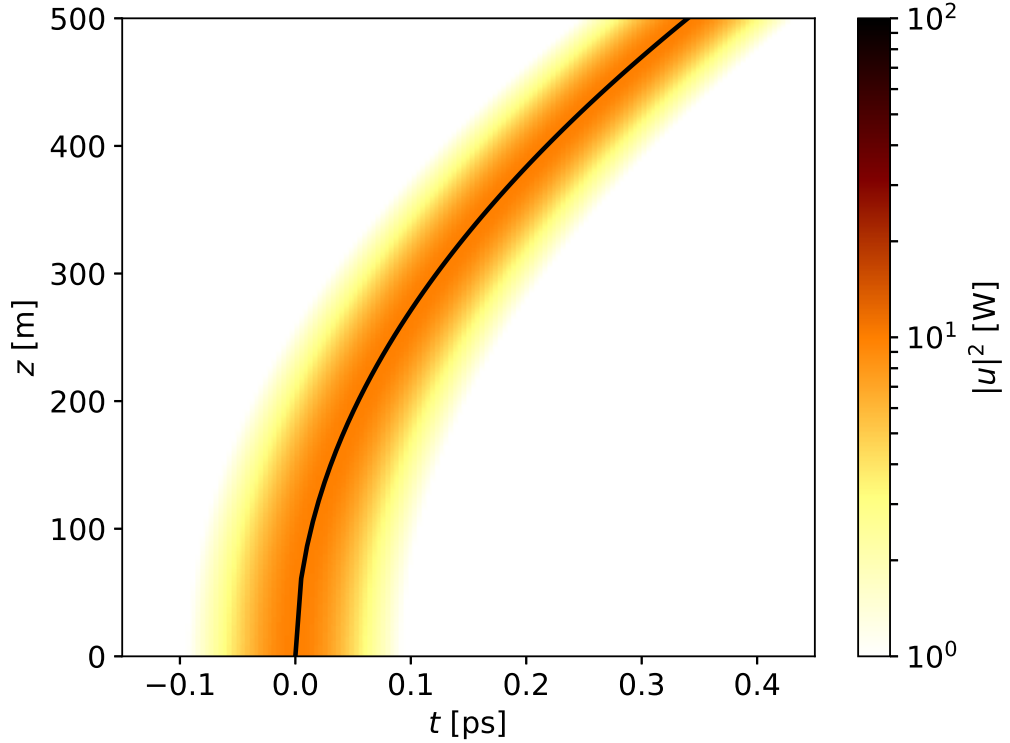
Figure 8.1: Intensity $|u(z,t)|^2$ of a soliton with peak power $P = 10$W and Raman term $T_R = 0.0005$ps as function of the time t and distance z in a selected time frame of $\Delta t = 0.6$ps and distance range $\Delta z = 0.5$km. The black line represents the theoretical prediction (8.7) for the soliton temporal shift.

8.2 Energy transfer

Another ingredient of our cascade model is the energy transfer between quasi-solitons. Fig. 8.2(a) shows a representative result for the collision of two pulses for Raman term $T_R = 0.05$ps and peak powers of 100W and 25W respectively. The intensity $|u(z,t)|^2$ is plotted as function of the time t and distance z. The initial phase difference between the two pulses is $\phi = 0.27\pi$ and the collision corresponds to the maximum energy transfer $\Delta E_1/E_2$ of $\sim 20\%$ plotted in Fig. 8.2(b). As for the case with TOD, we observe an energy transfer form the smaller to the larger quasi-soliton. Fig. 8.2 shows $\Delta E_1/E_2$ as function of the phase difference ϕ for various initial powers P_2. In comparison with the TOD case (cf. Fig. 5.2), $\Delta E_1/E_2$ cannot be approximated with a $\sin^2(\phi)$ and for $P_1 \gg P_2$ it becomes independent of ϕ.
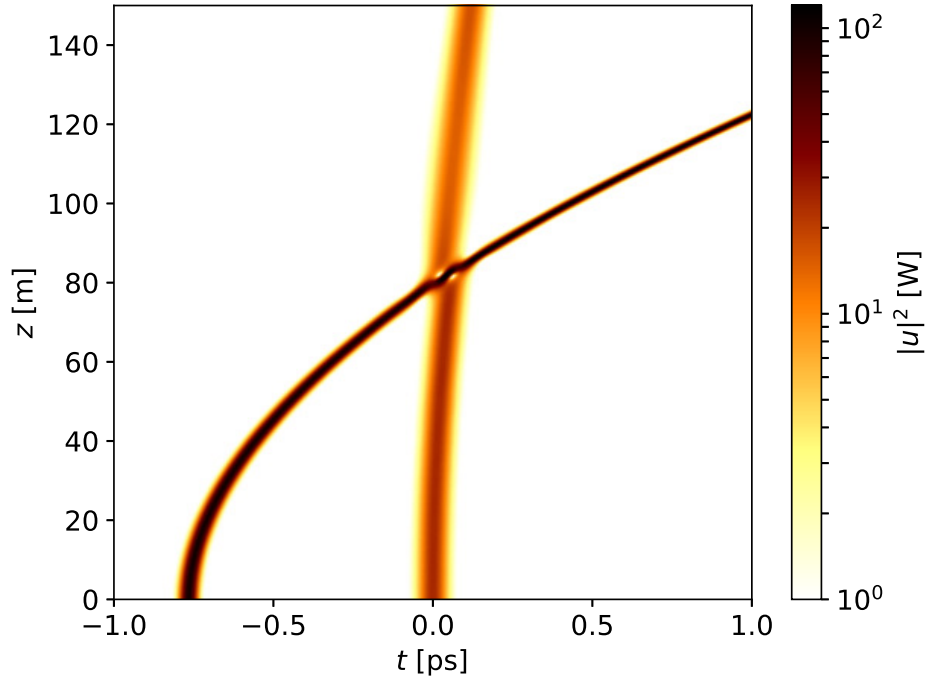
(a)
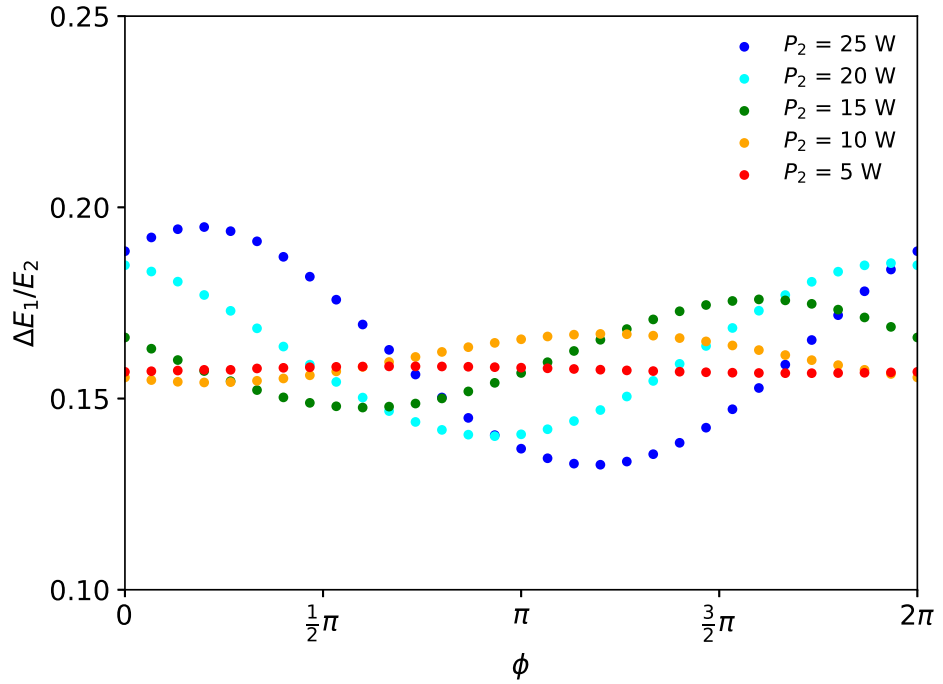
(b)

Figure 8.2: (a) Two soliton collision using Eq. (8.1) with $T_R = 0.0005$ps. The intensity $|u(z,t)|^2$ is plotted as function of the time t and distance z. The phase difference ϕ corresponds to the maximum energy transfer $\Delta E_1/E_2$. (b) Energy transfer $\Delta E_1/E_2$ as function of the phase difference ϕ for various initial powers P_2. The power P_1 is kept at the constant value of 100W.

Following the same procedure used in Sec. 5.3, $\Delta E_1/E_2$ can be written as

$$\frac{\Delta E_1}{E_2} = \frac{1}{|\, v_1^{-1} - v_2^{-1} \,|} \sum_{n=0}^{\infty} \epsilon_{\beta_2,T_R,\gamma,P_1,\Omega_1,P_2,\Omega_2}(n) \cos\left[n(\phi - \phi_0)\right]. \qquad (8.8)$$

For scattering in presence of RWs, $P_1 \gg P_2$, the energy transfer is ϕ independent and the series (8.8) can be stopped at zero order. Thus we can write

$$\frac{\Delta E_1}{E_2} = \frac{\epsilon_{\beta_2,T_R,\gamma,P_1,\Omega_1,P_2,\Omega_2}(0)}{|v_1^{-1} - v_2^{-1}|}. \qquad (8.9)$$

The parameter $\epsilon_{\beta_2,T_R,\gamma,P_1,\Omega_1,P_2,\Omega_2}(0)$ depends on seven quantities, the individual power and frequency shift of each quasi-soliton and the three fiber parameters. In order to devise a tractable model, as done for the TOD, $\epsilon_{\beta_2,T_R,\gamma,P_1,\Omega_1,P_2,\Omega_2}(0)$ is replaced with an effective ϵ_{eff} that describes the average properties of the interaction of a many quasi-soliton system. Our effective energy transfer becomes

$$\frac{\Delta E_1}{E_2} = \begin{cases} K & \text{for} \quad \frac{\epsilon_{\mathrm{eff}}}{|v_1^{-1}-v_2^{-1}|} > K\,, \\ \frac{\epsilon_{\mathrm{eff}}}{|v_1^{-1}-v_2^{-1}|} & \text{for} \quad \frac{\epsilon_{\mathrm{eff}}}{|v_1^{-1}-v_2^{-1}|} \le K\,. \end{cases} \qquad (8.10)$$

The cut-off K has been introduced because the term $1/|v_1^{-1} - v_2^{-1}|$ in the energy transfer diverges for $v_1 = v_2$ and can produce the unphysical result $\Delta E_1/E_2 > 1$. This artifice is necessary for the Raman case because at $z = 0$ all quasi-solitons have velocity $v^{-1} = \frac{dq}{dz} = 0$ and when two pulses scatter for the first time at a point $z \to 0$ we have $|v_1^{-1} - v_2^{-1}| \to 0$. As for the case with TOD, we calculate ϵ_{eff} and K minimizing the relative variance $r(\epsilon_{\mathrm{eff}}, K)$ of the PDFs (cf. Sec. 6.3). Unlike for the TOD case, we choose a distance $z = 300$m to calculate $r(\epsilon_{\mathrm{eff}}, K)$, that because, as we will see later, the process of RWs formation is faster for the Raman term than for TOD. The optimized values for ϵ_{eff} and K are $\epsilon_{\mathrm{eff}} = (0.85 \pm 0.03)$ps/m and $K = 0.099 \pm 0.004$. Note that the energy transfer in the Raman case (Eq. (8.10)) differs from the energy transfer in the TOD case (Eq. (6.4)). Such difference depends on the value of the coefficients $\epsilon(n)$ of Eq. (8.8). Unfortunately we do not know how to calculate the $\epsilon(n)$ analytically therefore we cannot give an explanation for their values, we can only consider the $\epsilon(n)$ as input parameters of our model to be determined empirically.

8.3 Initial conditions: PDF(P)

As initial condition for the cascade model we computed the PDF of the soliton peak power P, integrating the gNLSE with Raman term up to a distance $z = 100$m. We approximated the resulting initial PDF(P) with the distribution

$$\rho(P) = \frac{a}{\log(1 + \exp(ab))} \frac{1}{1 + \exp(a(P - b))}, \qquad (8.11)$$

where $a = (0.314 \pm 0.002)$W^{-1} and $b = (65 \pm 3)$W are fitting parameters. The initial PDF(P) and its fit are shown in Fig. 8.3(a). Our effective model aims to describe the soliton part of the gNLSE, hence to put more emphasis on the peaks rather than the background the fit has been performed taking the log of the data and the log of the fitting function (8.3). As shown in Fig. 8.3(a), the fit is in good agreement with the data on the tails ($P > 60$W) but we see differences towards low powers. Despite Eq. (8.11) not being a perfect approximation for the initial PDF(P), as shown in Fig. 8.3(b), the cascade model generates a PDF$(|u|^2)$ that is in good agreement with the gNLSE results.

8.4 Traces and PDFs

In Fig. 8.4(a) and (b) we show a representative result — a selected 10ps time range out of the full $\sim 2.5 \times 10^5$ ps — of $|u(z,t)|^2$ calculated using the gNLSE with Raman term and the cascade model respectively. As initial condition for the cascade, we generated a list of quasi-solitons by randomly choosing the power levels P in accordance with the statistics found in Eq. (8.11). The phases ϕ are drawn randomly from a uniform distribution in the interval $[0, 2\pi]$ and the quasi-solitons trajectories are calculated accordingly to Eq. (8.7) . The density of quasi-solitons is $\rho = 1/\Delta T = 4.5/ps$, namely the inverse of the average time between two peaks observed in the correlation function. In the gNLSE quasi-solitons emerge around 100m, to mimic this the cascade model only generates data from 100m onwards. In Fig. 8.4 we observe a behavior similar to the TOD case, colliding quasi-solitons that exchange energy. Most collisions are *inelastic* and energy is transferred from the quasi-soliton with less energy to the one with more energy leading to a cascade of incremental gains for the more powerful quasi-soliton. Initial differences in energy of quasi-solitons become exacerbated over time and larger and larger quasi-solitons emerge. These accumulate

the energy of the smaller ones to the point that the smaller ones eventually vanish into the background.
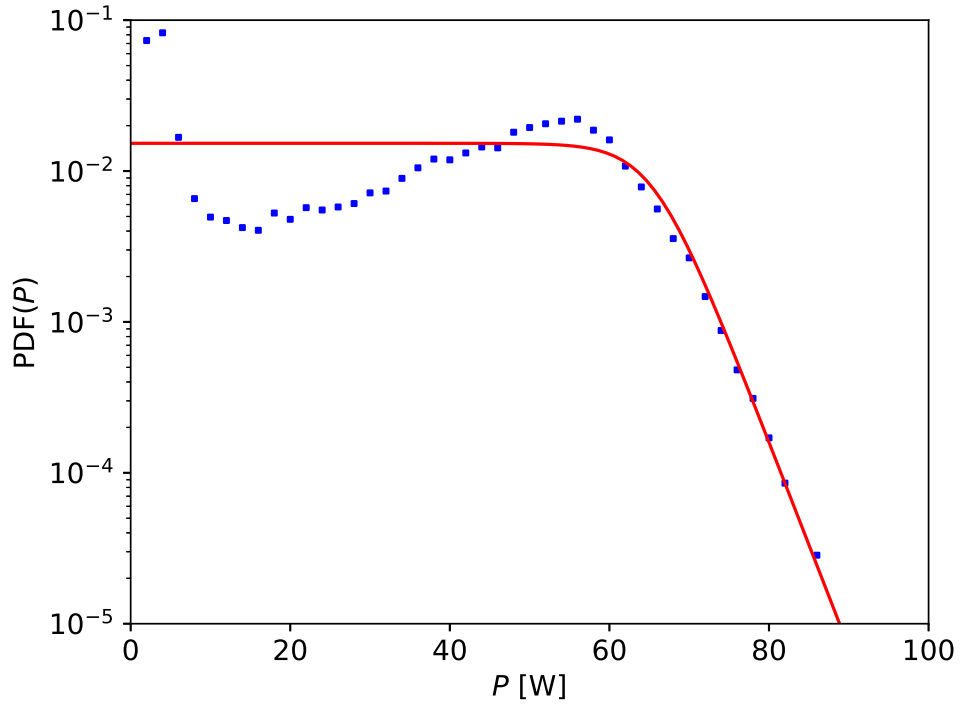
(a)
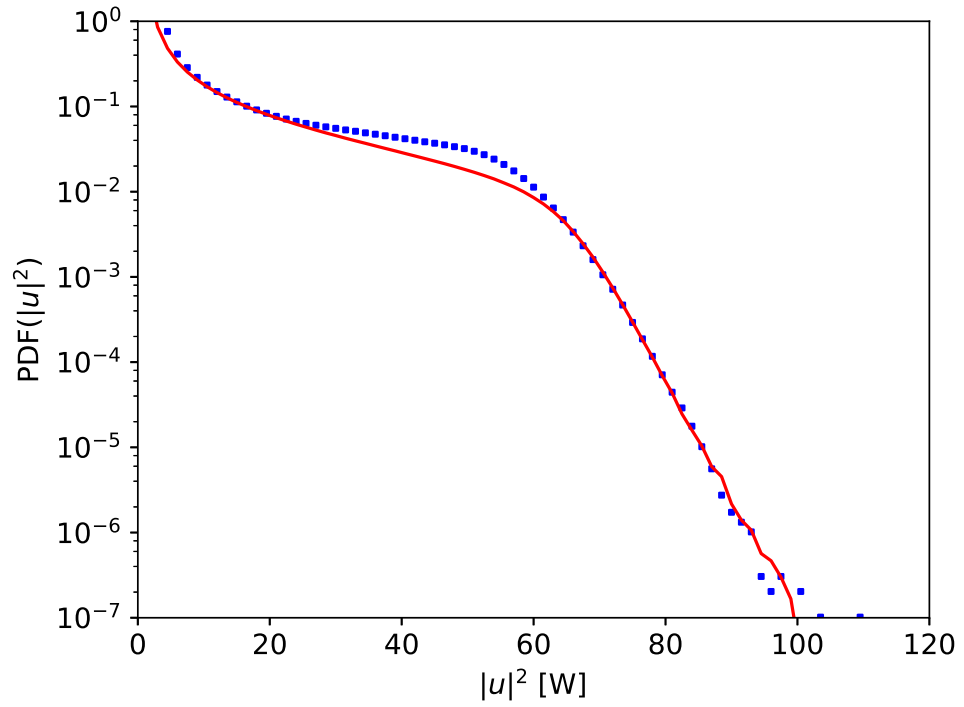
(b)

Figure 8.3: (a) Probability density function of the peak power PDF(P) for $T_R = 0.0005$ps at 100m. The blue squares denote the data while the solid (red) line shows the fit with Eq. (8.11). (b) PDFs of the intensity $|u|^2$ for the NLSE+Raman term (blue squares) and the cascade model (red line) at $z = 100$m.

For the TOD case, the group velocity of a quasi-soliton depends on the peak power. Raman quasi-solitons change their group velocity not only because of the change in peak power but also because of the self-frequency shift dependence on the distance as predicted by Eq. (8.6). This spontaneous acceleration of quasi-solitons allows the system to create rogue waves at higher rate than in the TOD case. Indeed, for the Raman case, we observe peak powers exceeding 1000W already at 500m rather than at 1500m like for the TOD (cf. Fig. 3.4).

The probability density function (PDF) for the complete set of $\sim 55 \times 10^3$ pulses propagating over 500m is shown in Fig. 8.5 for selected distances. The results are very similar to the TOD case, after 100m, the PDF shows a roughly exponential distribution, but the characteristic L-shape of a fully-developed RW PDF appears already at 400m rather than at 1000m (cf. Fig. 3.2). Starting with an average power of 10W after 500m there is a probability of $\sim 5 \times 10^{-5}$ to find a RW with power 1000W. In Fig. 8.5 we compare the PDFs for the CM and the gNLSE. The agreement for the PDFs is not as good as for the TOD case, but the cascade model can still capture the essence of the emergence of rogue waves. The disagreement is more pronounced at early stages, then at 500m the two model show similar results. Such behavior is presumably due to the quasi-soliton acceleration in the Raman case. Indeed, because the dynamics is accelerated, small differences in the initial conditions produce large differences at long distances. After a certain distance the process of RW formation has stabilized, acceleration is not important anymore in energy exchange and the gNLSE and CM produce again similar PDFs. Note that Eq. (8.10) is an approximation of the real energy transfer and therefore the two quasi-soliton scattering is not modeled in all its details. Our results can only be improved with a better theory of the two quasi-soliton scattering, which has not beed developed yet [22–25].
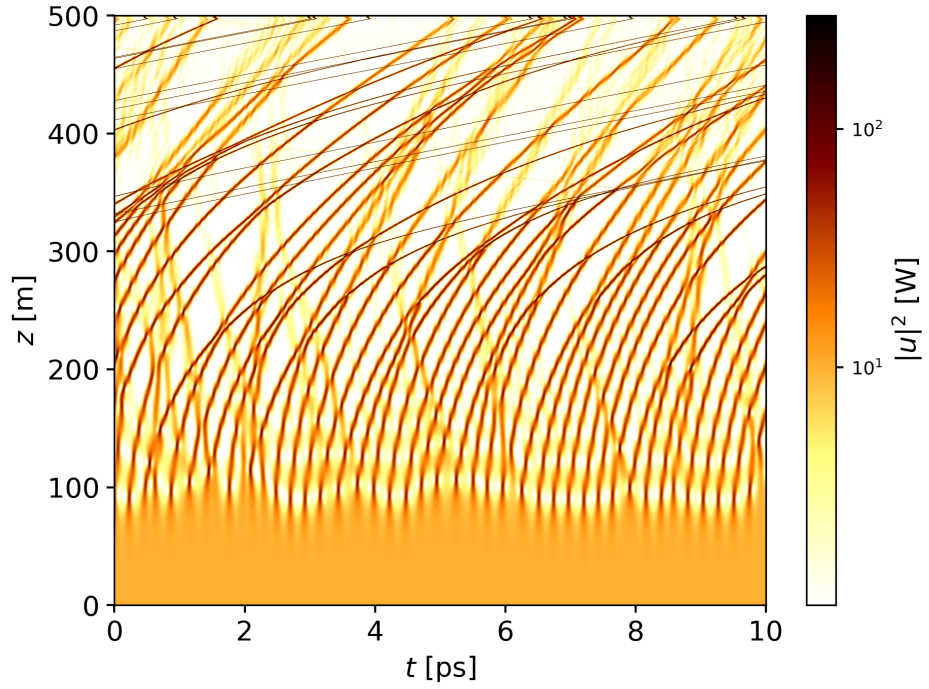
(a)
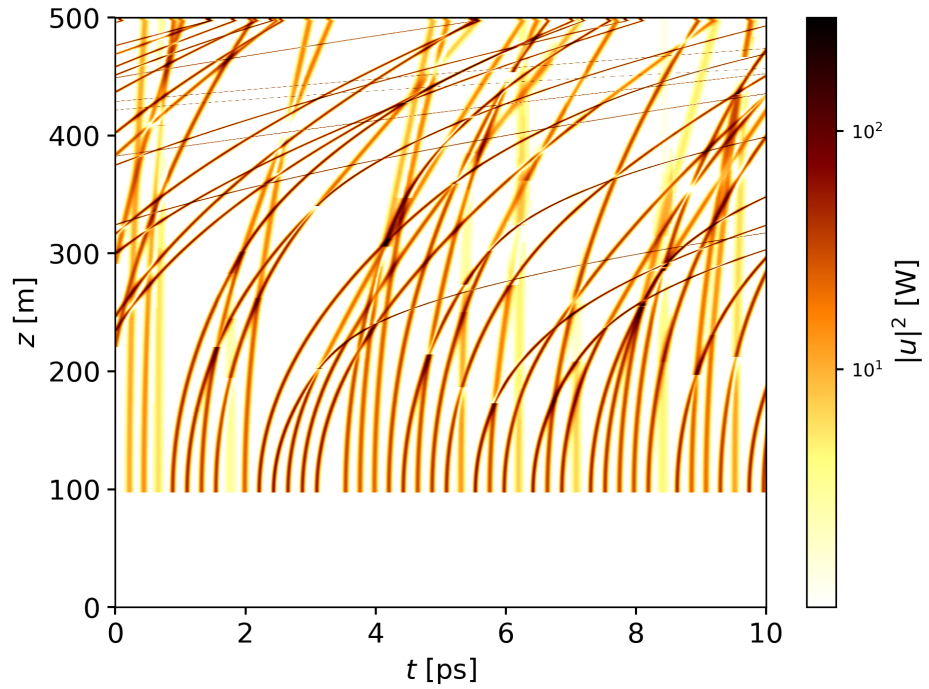
(b)

Figure 8.4: (a) Intensity $|u|^2$ of the NLSE+Raman term as function of the time t and distance z in a selected time frame of $\Delta t = 10$ps and distance range $\Delta z = 0.5$km. (b) Intensities $|u|^2$ as computed from the effective cascade model with Raman term using the same shading/color scale as in (a). Note that we start the effective model at $z_0 = 100$m to mimic the effects of the modulation instability in (a).
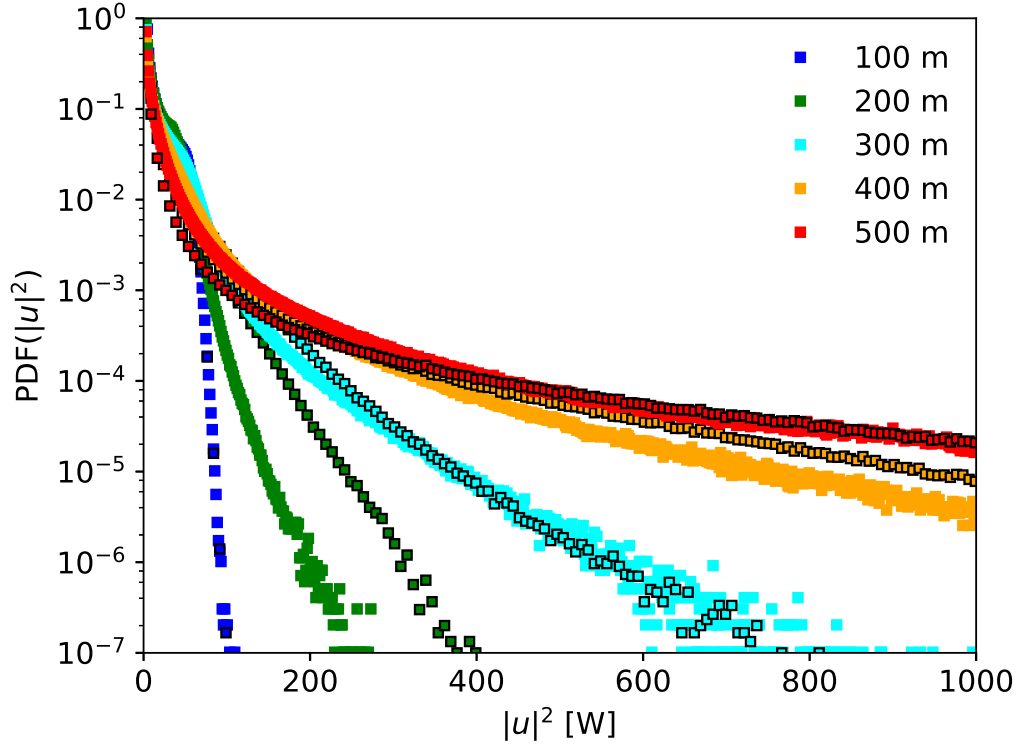
Figure 8.5: PDFs of the intensity $|u|^2$ for the NLSE+Raman term (colored squares) and the cascade model (colored squares with black edges). The PDFs have been computed at distances $z = 100$m, 200m, 300m, 400m and 500m.

8.5 Calm before the storm for Raman interaction

In chapter 7 we saw that in an optical fiber with TOD, RWs are preceded by a time period of reduced power values. We observe the same "calm before the storm" phenomenon for the Raman interaction, at list for the gNLSE calculation. In Fig. 8.6 we can see an asymmetry in the normalized power $|u(\Delta t)|^2/\langle|u(\Delta t)|^2\rangle$ relative to the RW event at $\Delta t = 0$ ($\Delta t < 0$ denotes events before the RW). The average includes all RWs, defined here as large power events above a threshold of 150W. Fig. 8.6 (a) and (b) correspond, respectively, to the gNLSE and CM results. In both models at $z = 200$m the period of calm lasts about $\Delta t = 0.75$ps and the intensity is reduced of more than 60%. At $z = 300$m the two models behave differently. For the gNLSE case we can still observe a clear asymmetry with "missing energy" preceding the RW.
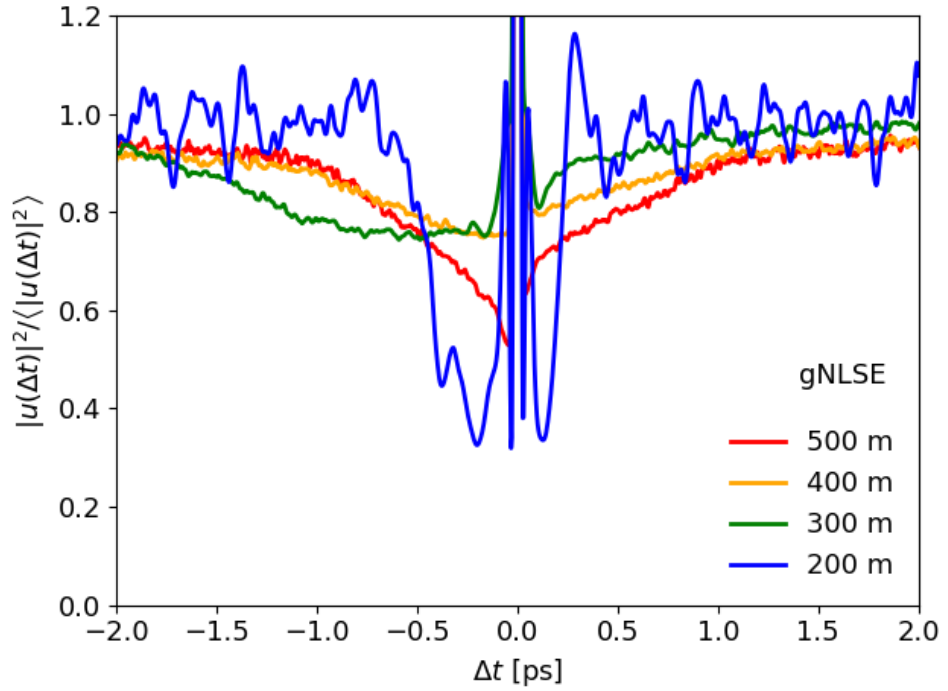
(a)
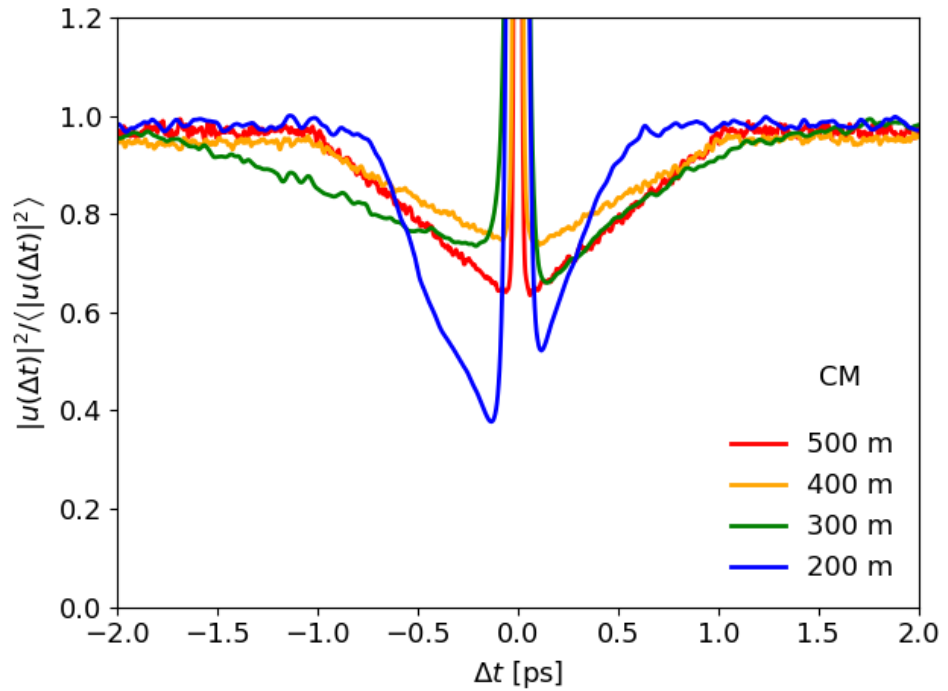
(b)

Figure 8.6: Normalized averaged powers $|u(\Delta t)|^2/\langle|u(\Delta t)|^2\rangle$ for times Δt in the vicinity of a RW event at $\Delta t = 0$, computed at distances 200m, 300m, 400m and 500m. Panel (a) and (b) correspond respectively to the gNLSE and CM when Raman interaction is considered. In both panels, we identify RWs as corresponding to powers equal to or larger than 150W.

In the CM case the intensity before the RW peak is actually shallower than after the event, though the depth lasts for a longer time and therefore there is more "missing energy" on the left than on the right of the event. From $z = 400\text{m}$ in both cases the normalized intensity starts to became symmetric around the RW.

Summary

In this chapter, we used the cascade model to study rogue waves in the case of Raman interaction. The key points of the chapter are:

- The gNLSE with Raman term has quasi-soliton solution. The optical field of such pulses can be approximated by

$$u(z, t) = \sqrt{P} \operatorname{sech}\left[\frac{t - q}{T}\right] \exp\left[i\left(\frac{\beta_2}{2}\Omega^2 + \frac{\gamma P}{2}\right)z - i\Omega t\right],$$

  with $T = \sqrt{\frac{|\beta_2|}{\gamma P}}$, $\Omega = -\frac{8}{15}\frac{T_R \gamma P}{T^2}z$ and $q = t_0 - \frac{4}{15}\frac{T_R \gamma \beta_2 P}{T^2}z^2$.

- The cascade model for Raman interaction is implemented using an effective energy transfer

$$\frac{\Delta E_1}{E_2} = \begin{cases} K & \text{for} \quad \frac{\epsilon_{\text{eff}}}{|v_1^{-1} - v_2^{-1}|} > K, \\[2ex] \frac{\epsilon_{\text{eff}}}{|v_1^{-1} - v_2^{-1}|} & \text{for} \quad \frac{\epsilon_{\text{eff}}}{|v_1^{-1} - v_2^{-1}|} \leq K, \end{cases}$$

  where the effective coupling ϵ_{eff} and the cut-off K are calculated numerically.

- The cascade model require initial conditions that are taken from the gNLSE integration. The initial probability density function of the peak power can be modeled as

$$\rho(P) = \frac{a}{\log(1 + \exp(ab))} \frac{1}{1 + \exp(a(P - b))},$$

  where $a = 0.314 \pm 0.002\text{W}^{-1}$ and $b = 65 \pm 3\text{W}$ are fitting parameters. The density of quasi-solitons was measured to be $\rho = 1/\Delta T = 4.5/ps$.

- The full gNLSE integration and the cascade model with Raman term produce long-tail PDFs. Although the agreement between the two methods is not perfect, the cascade model can still capture the essence of the emergence of rogue waves.

- As for the TOD case, when Raman interaction is considered rogue waves are preceded by a time period of reduced power values.

In the next chapter, we propose an experiment to comprehend the underling physics governing quasi-soliton energy transfer.

Chapter 9

Experimental proposal for soliton interaction

In the previous chapters we have shown that quasi-solitons exchange energy in the gNLSE with TOD or Raman term. In this chapter we propose an experimental setup to study collision-induced soliton amplification. In an optical fiber with anomalous dispersion ($\beta_2 < 0$), we replace a small region of the fiber with a normal dispersion fiber ($\beta_2 > 0$). We show that solitons colliding in this region are able to exchange energy. In section 9.1 we describe the experimental setup. The analytical model used for the simulation is introduced in section 9.2. In section 9.3 we discuss the numerical results obtained from the simulation, especially we will focus on the energy transfer between solitons. Section 9.4 explains how our device can be exploited for soliton amplification in optical fiber systems. Finally, in section 9.5 we propose a fit for the energy transfer function.

9.1 Experimental setup

Energy transfer in pairwise soliton collisions usually requires the additional presence of TOD [78, 90] or Raman term [62–64, 92] in the NLSE. In this chapter, we describe a dispersion map that leads to inelastic soliton collisions without any such additions. Consider a fiber with standard *anomalous* dispersion in which two solitons, with different group velocities, propagate as stable pulses and eventually collide. The trick is now to replace the section of the fiber, where the soliton collision takes place, with a section of *normal* dispersion fiber (cf. Fig. 9.1). In the normal dispersion regime,
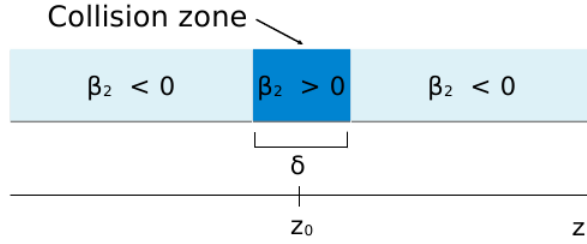
91

Figure 9.1: Schematic representation of the optical fiber used for the thought experiment. The horizontal fiber is indicated in blue. The light blue region corresponds to the anomalous-dispersion fiber ($\beta_2 < 0$) while the normal-dispersion fiber ($\beta_2 > 0$) of length δ is indicated in dark blue. The light propagation direction is indicated by a thin horizontal line including the point of collision z_0.

the solitons are unstable, hence able to exchange energy under collision. Keeping this normal dispersion section short avoids excessive pulse-width broadening which would otherwise destroy the solitons. We optimize the dispersion map to maximize energy transfer between the solitons while keeping the disturbance of the soliton shape as small as possible. Hence two stable solitons emerge into the anomalous dispersion regime and continue to propagate.

9.2 The model

To model the situation proposed above, we use the NLSE [26] with a dispersion map $\beta_2(z)$

$$\partial_z u + \frac{i\beta_2(z)}{2}\partial_t^2 u - i\gamma|u|^2 u = 0. \tag{9.1}$$

Here $u(z,t)$ is the pulse envelope, z is the distance of propagation, t is the time in the frame moving with the average group velocity of the carrier wave and γ the non-linear coefficient. The dispersion $\beta_2(z)$ is equal to a constant $\beta_2 > 0$ in the region $\left[z_0 - \frac{\delta}{2}, z_0 + \frac{\delta}{2}\right]$ and equal to $-\beta_2$ elsewhere; δ denotes the length of the normal ($\beta_2 > 0$) fiber symmetrically around the point of collision z_0. We start with an initial condition consisting of two solitons at $z \ll z_0$, such that we can write initially

$$u(z,t) = \sqrt{P_1}\operatorname{sech}\left(\frac{t - t_1}{T_1}\right)e^{-i\Omega_1 t} + \sqrt{P_2}\operatorname{sech}\left(\frac{t - t_2}{T_2}\right)e^{-i\Omega_2 t + i\phi}. \tag{9.2}$$

The two pulses have a relative phase difference ϕ, and are characterized by power P_i, temporal shift t_i and frequency shift Ω_i for each pulse $i = 1, 2$. From these initial

conditions we can calculate their inverse velocity $v_i^{-1} = \beta_2 \Omega_i$, period $T_i = \sqrt{\frac{|\beta_2|}{\gamma P_i}}$ and energy $E_i = 2 P_i T_i$. Note that Eq. (9.1) can be derived from Maxwell's equations assuming that the linear polarization P_L is space dependent (see section 1.2), but we do not get extra terms, beside the standard NLSE terms, because the Maxwell's equations contain only time derivatives of P_L.

9.3 Numerical results

Fig. 9.2 (a) and 9.2 (b) show representative results for the collision of two solitons for the experimental setup described in Fig. 9.1. The intensity $|u|^2$ is plotted as function of time t and distance z. The initial conditions in both collisions are identical apart from the relative phase ϕ between the two solitons, in (a) $\phi = 0.13\pi$ and in (b) $\phi = 1.87\pi$. The initial power and frequency are $P_1 = 100\text{W}$, $\Omega_1 = -10\text{THz}$, $P_2 = 70\text{W}$ and $\Omega_2 = -6\text{THz}$. The length δ of the optical fiber with normal dispersion is 0.6m. The optical fiber specifications are $|\beta_2| = 0.01\text{ps}^2\text{m}^{-1}$ and $\gamma = 0.003\text{W}^{-1}\text{m}^{-1}$.

In Fig. 9.2, a first soliton (100W) collides with a second soliton (70W). After the collision both solitons emerge with peak power different from the initial one. In Fig. 9.2 (a) energy is transferred from the second to the first soliton, the emerging pulses have peak power of $\sim 138\text{W}$ and $\sim 24\text{W}$ respectively, the first soliton has gained 38W in amplitude. In Fig. 9.2 (b) we observe the opposite behavior, the emerging pulses have peak power of $\sim 50\text{W}$ and $\sim 73\text{W}$ respectively, although in this case the second soliton gains just 3W and half of the power of the first soliton is radiated. In Fig. 9.3 (b) we show the maximum peak power of Fig. 9.2 (a) in order to highlight details of the process. The initial peak value is 100W, then after the collision it oscillates and slowly dampens to the value 138W when away from the collision region. This peak power mostly corresponds to the value of the first soliton.
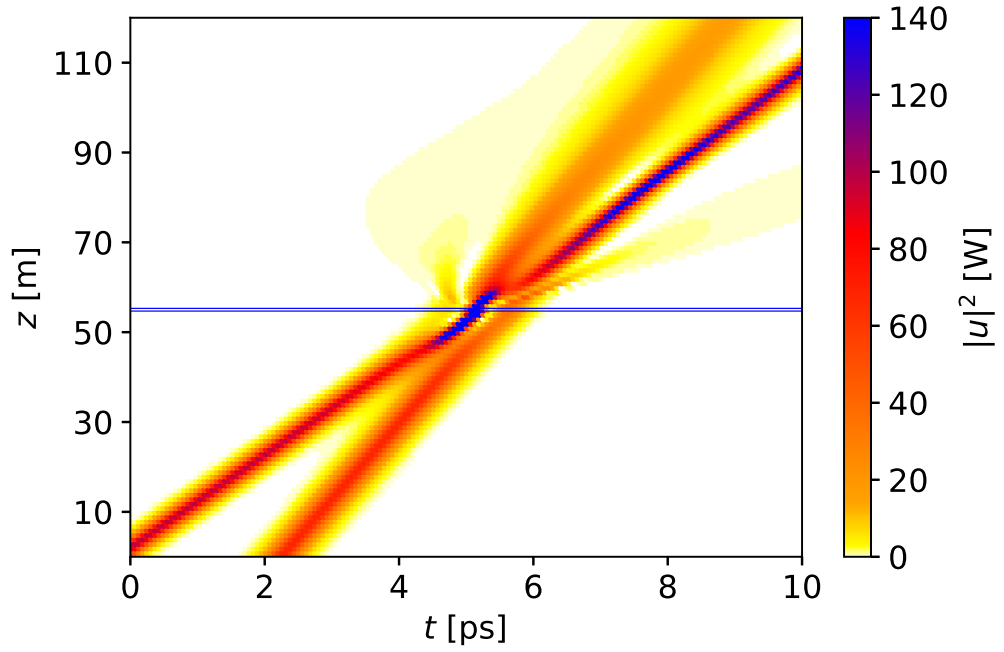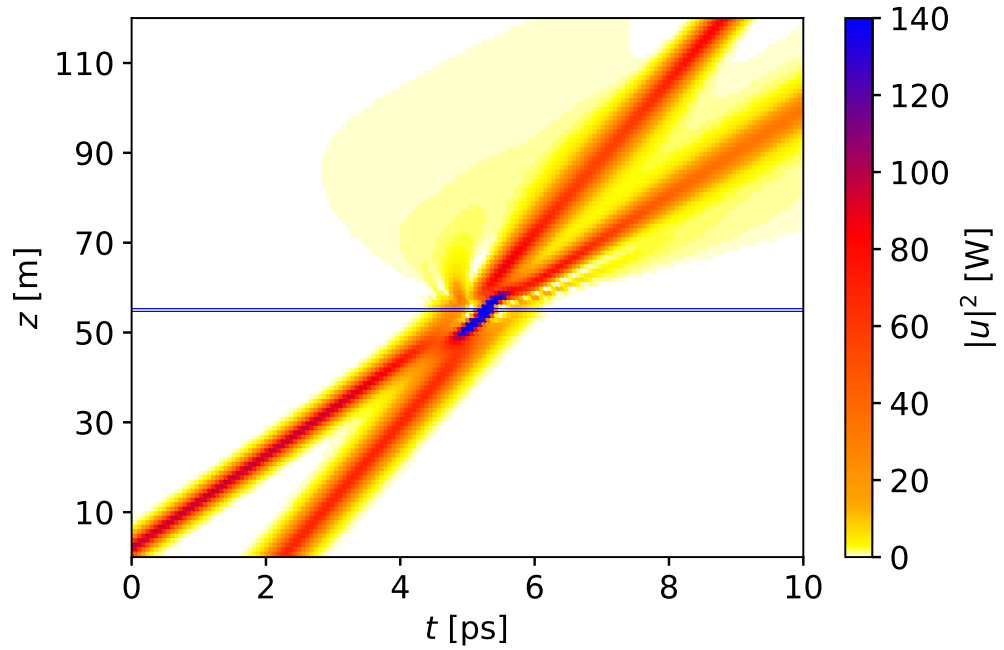
Figure 9.2: Two soliton collision for the experimental setup described in Fig. 9.1. The intensity $|u|^2$ is plotted as function of time t and distance z. The phase difference ϕ corresponds to (a) the maximum and (b) minimum energy transfer $\Delta E_1/E_2$ plotted in Fig. 9.3 (a). The horizontal blue line indicates the point of collision z_0 in the normal-dispersion fiber.
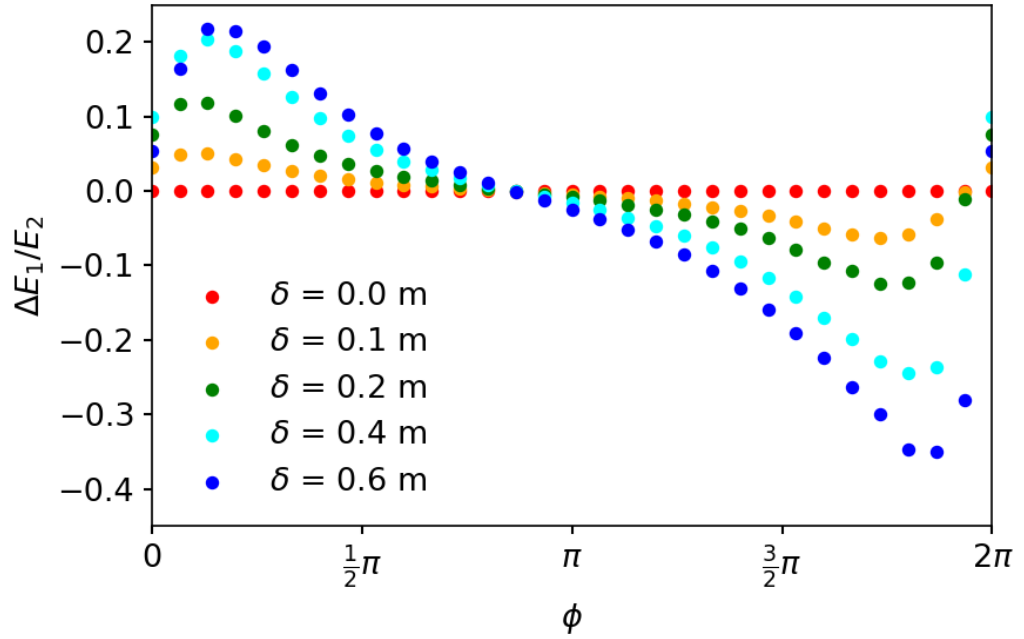
(a)
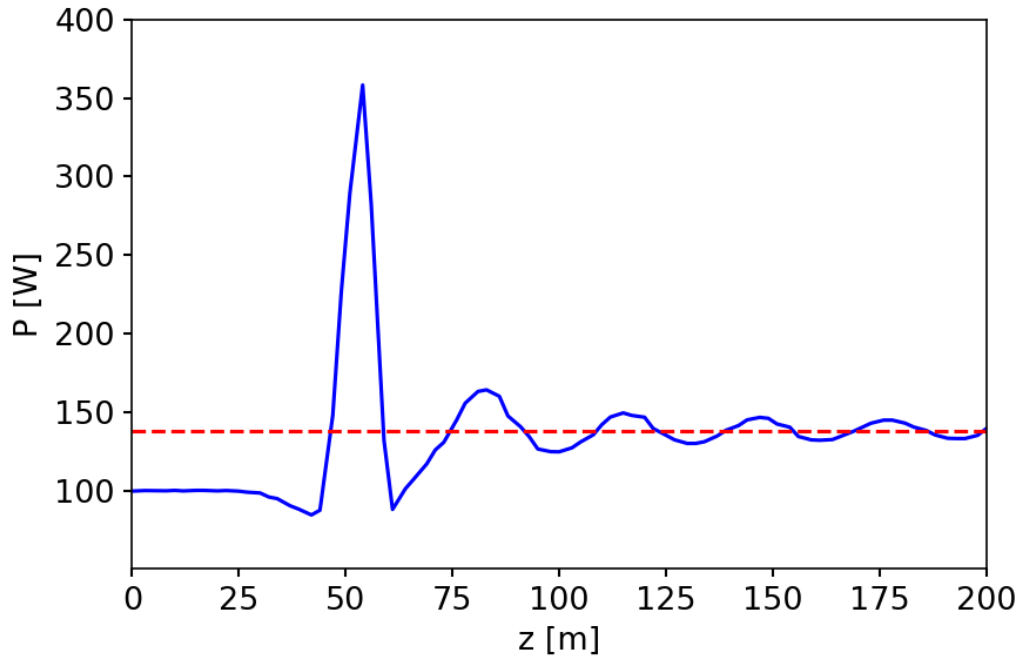
(b)

Figure 9.3: (a) Energy transfer $\Delta E_1/E_2$ as function of the phase difference ϕ for various lengths δ of the normal-dispersion fiber. (b) Maximum peak power (continuous blue line) as function of the distance z, calculated for the intensities in Fig. 9.2 (a). The dotted red line indicates the average power of 138W after the collision.

The numerical experiment confirms our hypothesis, instability leads to soliton energy exchange. We note that energy transfer occurs without TOD and Raman term [90, 92]. The artificial instability, due to the change of sign in the second order dispersion term, is sufficient to mimic the effect of higher order terms for the two soliton collision.

To determine the influence of the phase difference ϕ and the length δ on the energy transfer, we studied collisions varying these two parameters. For each value of ϕ and δ, we calculate the percentage of energy transfer $\Delta E_1/E_2$, from soliton 2 to soliton 1. Fig. 9.3 (a) shows the result of these calculations. The energy transfer changes with ϕ, it can be positive or negative meaning that energy can go from the second soliton to first one and vice versa. The local maximum and minimum are at $\phi = 0.13\pi$ and $\phi = 1.87\pi$ respectively. The maximum value of $\Delta E_1/E_2$ corresponding to the collision in Fig. 9.2 (a) is $\sim +22\%$, the minimum corresponding to the collision in Fig. 9.2 (b) is $\sim -35\%$. This asymmetry towards the minimum is an indication of energy loss and can be understood as energy that is radiate during the scattering process. The energy transfer increases with δ and it is null when δ is zero, confirming that the unstable region is fundamental for the process to occur.
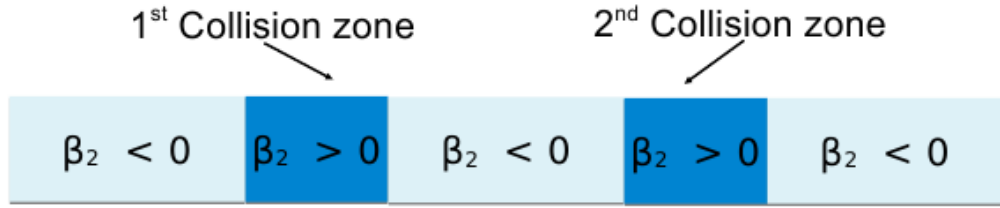
Figure 9.4: Experimental setup for two consecutive amplifications. One normal-dispersion segment is placed at every point of collision. The colors are chosen as in Fig. 9.1.

9.4 Optical amplification

The above results show that the system in Fig. 9.1 is an amplification device. Particularly, assembling many of such devices in series, a soliton can be amplified several times. For example, with three initial solitons and two devices in series as in Fig. 9.4 , we get the amplification shown in Fig. 9.5 (a).

In this case a first soliton (100W) collides with a second (70W) and then a third soliton (70W) absorbing energy at every collision. The first soliton emerges with an amplitude of ∼138W from the first collision and an amplitude of ∼178W from the second collision as shown in Fig. 9.5 (b). The initial phase differences are chosen so that the energy transfer is maximized at every scattering. In principle, there is no limit to the number of amplification devices that can be assembled and the early soliton can be amplified at every collision as long as it has a certain phase difference with the other colliding pulses.
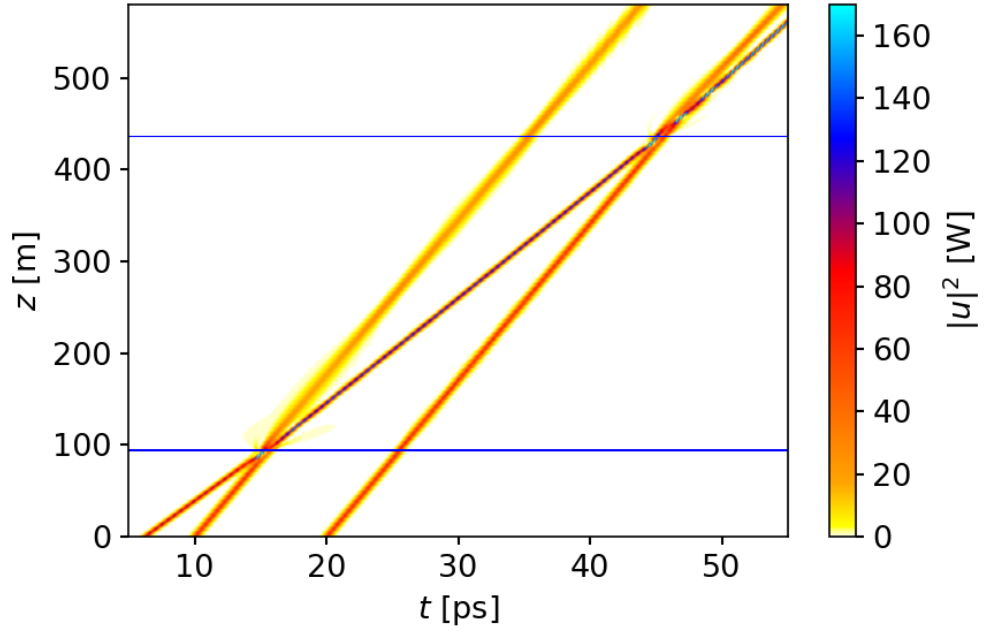
(a)
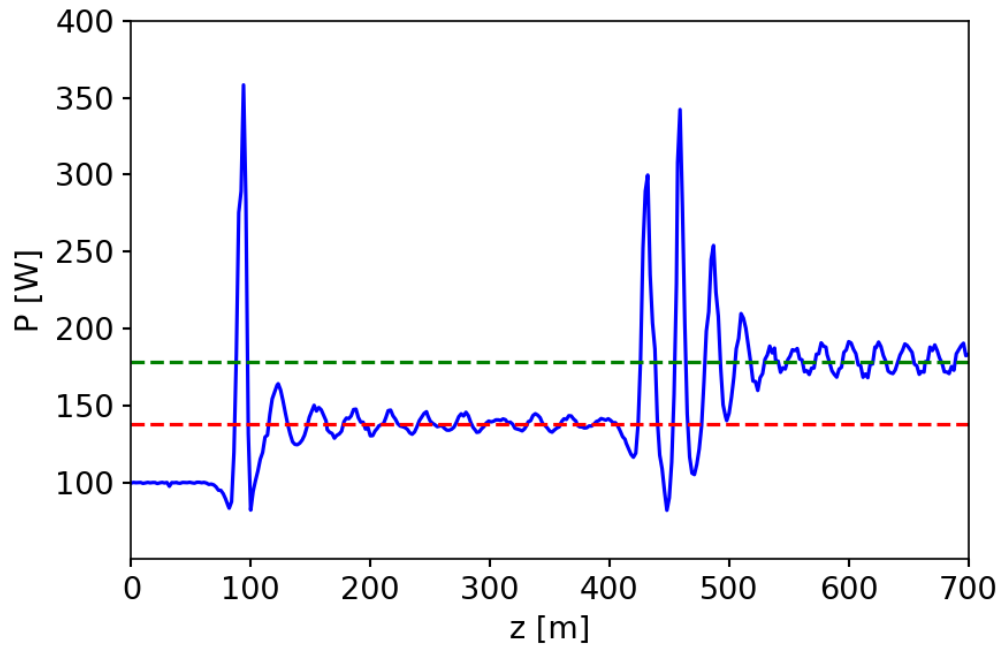
(b)

Figure 9.5: (a) Intensity $|u|^2$ plotted as function of time t and distance z for a three soliton collision process. An early soliton (starting at $z = 0$ m and $t = 4$ ps) is amplified twice in consecutive collisions. The horizontal blue lines indicate the points of collision in the normal-dispersion fiber. (b) Maximum peak power (continuous blue line) as function of the distance z, calculated for the collisions in (a). The dotted red and green lines indicate the average power of 138W and 178W after the first and second collision respectively.
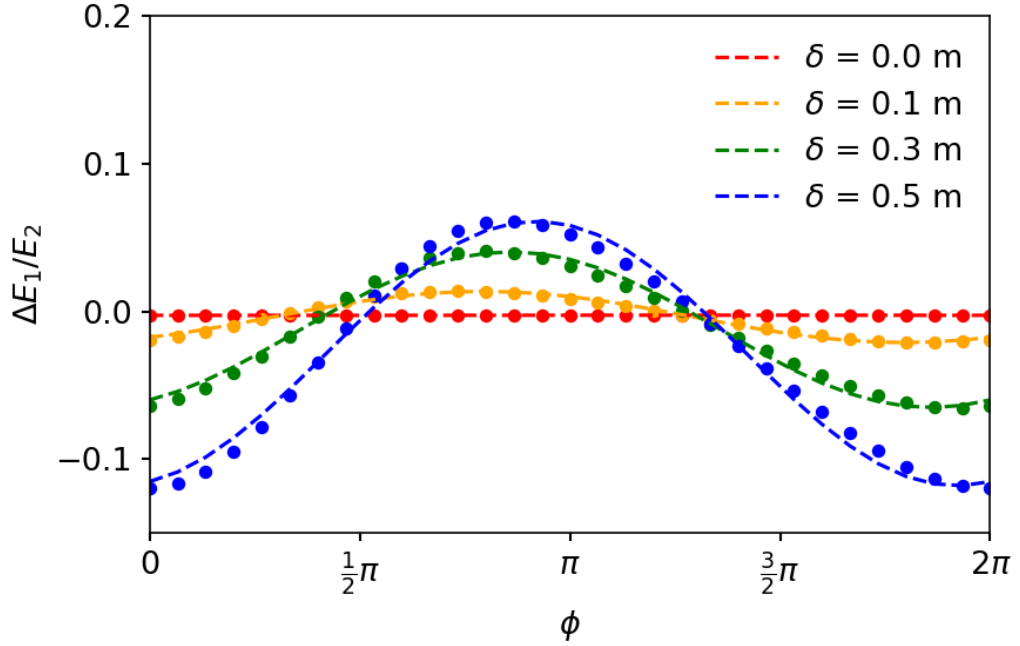
Figure 9.6: Energy transfer $\Delta E_1/E_2$ as function of the phase difference ϕ and the length δ. The data points represents result of the simulations while the lines denote the fit according to Eq. (9.3).

9.5 Fit for the energy transfer function

For the collisions in Fig. 9.2 and 9.3 we used two solitons with initial powers $P_1 = 100\text{W}$ and $P_2 = 70\text{W}$. When $P_2 \ll P_1$, the energy transfer can be approximated as

$$\triangle E_1 = \epsilon_L + \epsilon_T \sin\left(\phi - \phi_0\right), \tag{9.3}$$

where ϵ_L, ϵ_T and ϕ_0 are coefficients to be fitted. Fig. 9.6 shows a representative result for $P_1 = 100\text{W}$ and $P_2 = 10\text{W}$. The data points represent results of the simulations while the lines denote a fit with (9.3). The fit coefficients depend on the parameters

$$\{\delta, \beta_2, \gamma, P_1, \Omega_1, P_2, \Omega_2\}. \tag{9.4}$$

A dimensional analysis shows that ϵ_L and ϵ_T can be written in the form

$$\epsilon_L = g_1\gamma\delta^{\lambda_1}|\beta_2|^{\lambda_1-1}\left(\Delta\Omega\right)^{2\lambda_1-3}P_1^{\eta_1}P_2^{2-\eta_1}, \qquad (9.5)$$

$$\epsilon_T = g_2\gamma\delta^{\lambda_2}|\beta_2|^{\lambda_2-1}\left(\Delta\Omega\right)^{2\lambda_2-3}P_1^{\eta_2}P_2^{2-\eta_2}. \qquad (9.6)$$

The coefficients g_1 and g_2 are dimensionless. Note that λ_1, η_1, λ_2 and η_2 are dimensionless by construction and $\Delta\Omega = |\Omega_1 - \Omega_2|$. In order to fit Eq. (9.5) and (9.6), we have calculated the energy transfer for a number of initial conditions by varying the set of parameters (9.4). We find the following values for the fit coefficients $g_1 = -2.74 \pm 0.08$, $\lambda_1 = 1.67 \pm 0.02$, $\eta_1 = 1.417 \pm 0.007$, $g_2 = 3.01 \pm 0.19$, $\lambda_2 = 1.13 \pm 0.04$ and $\eta_2 = 1.529 \pm 0.015$. Fig. 9.7 and 9.8 show the fits of ϵ_L and ϵ_T using Eq. (9.5) and (9.6). The six dimensional fits are projected into two dimension at constant values $\delta = 0.5$m, $|\beta_2| = 0.02$ps^{2}m^{-1}, $\gamma = 0.002$W^{-1}m^{-1}, $P_1 = 100$W, $\Omega_1 = -10$THz, $P_2 = 10$W and $\Omega_2 = -5$THz. The multidimensional fit and the numerical results are in an overall good agreement. While a fit using rational exponents such as $\lambda_1 = \lambda_2 = \eta_1 = \eta_2 = 1.5$ (or $\lambda_1 = \eta_1 = \eta_2 = 1.5$ and $\lambda_2 = 1$) is possible, the results are much worse.

Figure 9.7: Functional dependence of ϵ_L on each of the six parameters given by Eq. (9.4). The data points represents numerical results of Eq. (9.1) while the red lines denote the fit (9.5), the pink region indicates the 68% confidence level on the fit.
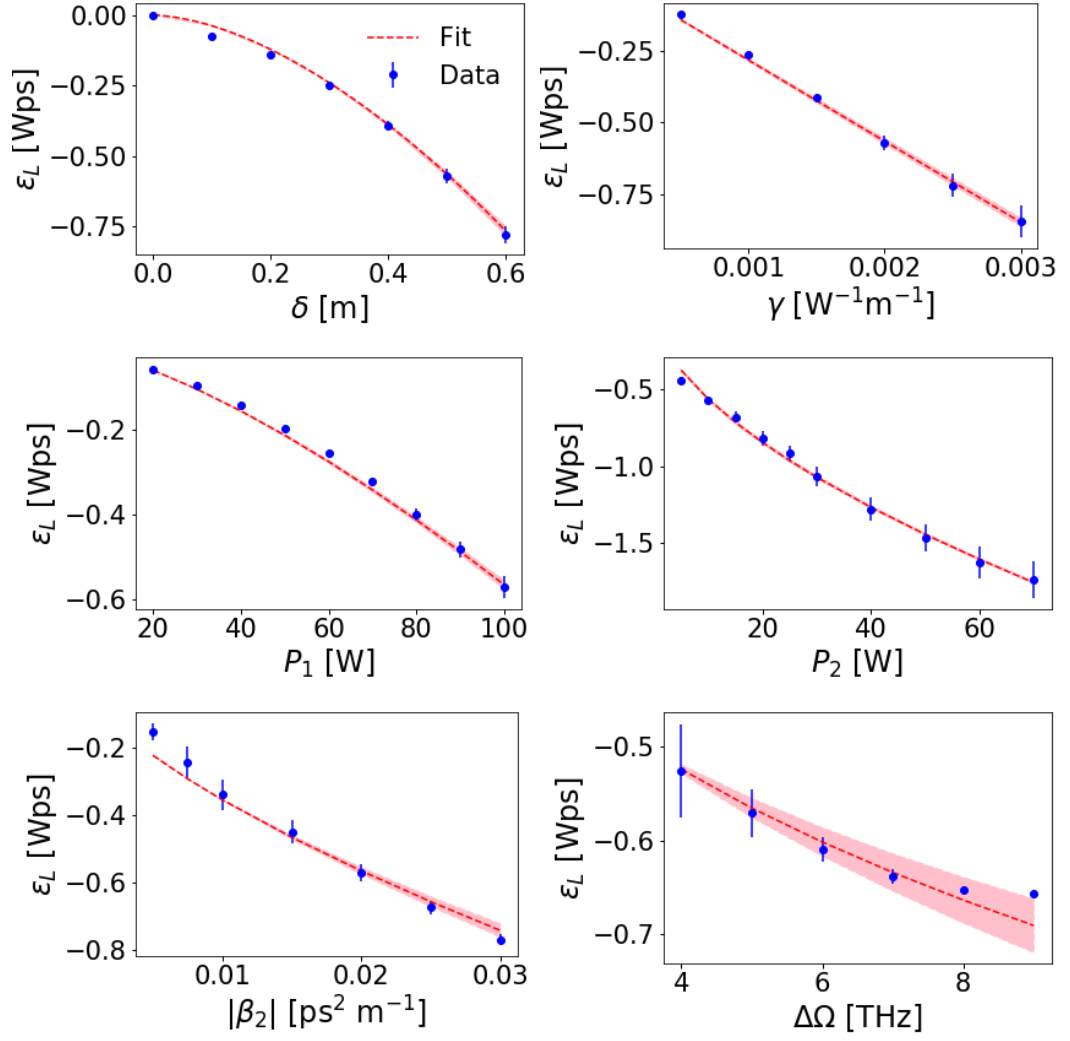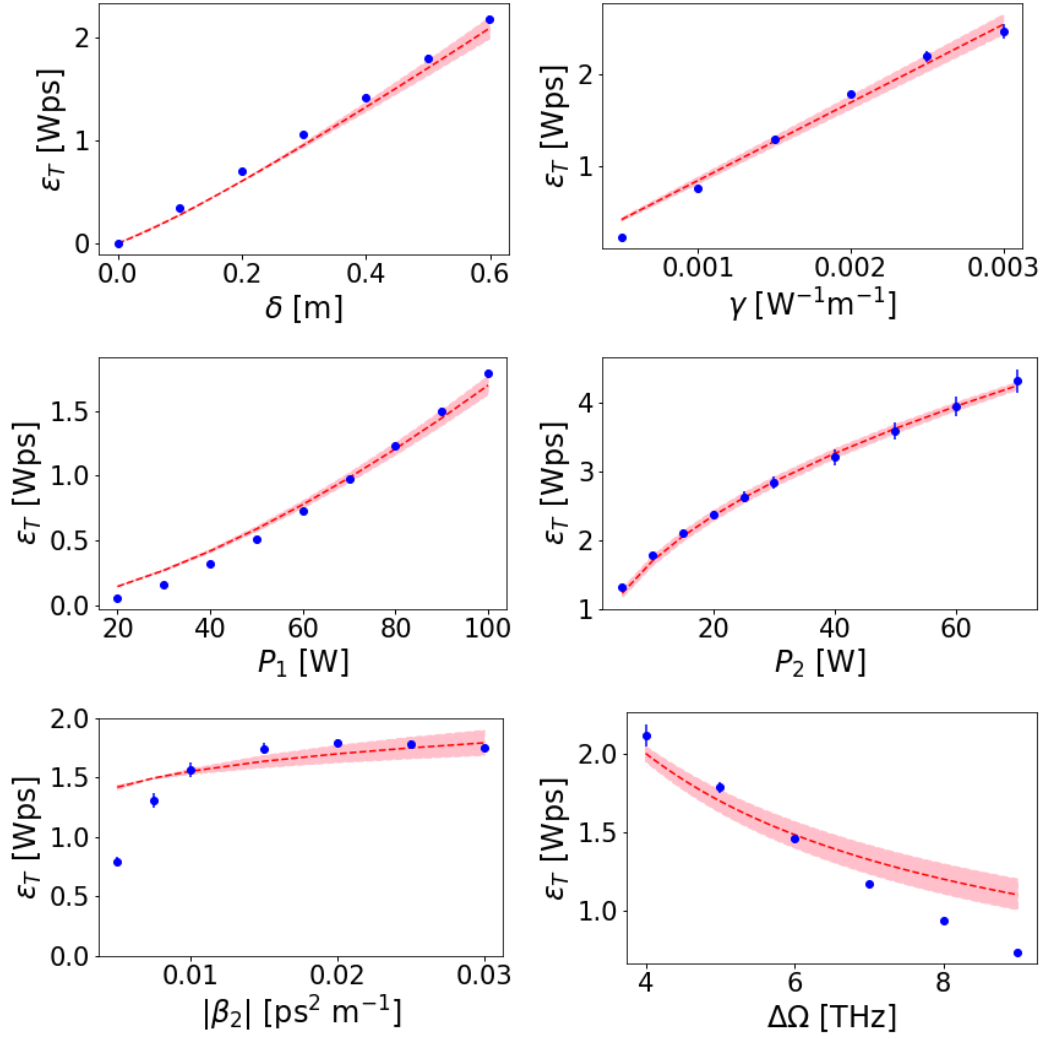
Figure 9.8: Functional dependence of ϵ_T on each of the six parameters given by Eq. (9.4). The data points represents numerical results of Eq. (9.1) while the red lines denote the fit (9.6), the pink region is as in Fig. 9.7, indicating the 68% confidence levels.

Summary

In this chapter, we proposed an experimental setup to study the underling physics governing soliton energy transfer. The main points of the chapter are:

- The experimental setup consists in a dispersion map between an optical fiber with anomalous dispersion ($\beta_2 < 0$) and a normal dispersion fiber ($\beta_2 > 0$). This can be modeled as

$$\partial_z u + \frac{i\beta_2(z)}{2}\partial_t^2 u - i\gamma|u|^2 u = 0,$$

  where the dispersion $\beta_2(z)$ is equal to a constant $\beta_2 > 0$ in the region $\left[z_0 - \frac{\delta}{2}, z_0 + \frac{\delta}{2}\right]$ and equal to $-\beta_2$ elsewhere.

- Our numerical experiment indicates the energy transfer between two unstable bright solitons in the normal-dispersion regions of a fiber. The energy gain that can exceed 20% for each collision.

- The width δ of the normal dispersion region is important for the process to occur, as well as the phase difference ϕ between the two solitons.

- The device in Fig. 9.1 can be exploited for soliton amplification in optical fiber systems.

We want to highlight that the device in Fig. 9.1 can be built in a real world laboratory and our predictions for the energy transfer (Fig. 9.3 (a)) can be verified experimentally.

Conclusions

In this work we have examined several aspects of rogue wave formation and quasi-soliton interaction in optical fibers. Our results emphasize the crucial role played by quasi-soliton interactions in the energy exchange underlying the formation of RWs via the proposed cascade mechanism. While interactions are known to play an important role in RW generation [62–65, 93–99], the elucidation of the full cascade mechanism including its resonance-like quasi-soliton pair scattering and details such as the "calm before the storm", might be essential ingredients of any attempt at RW predictions [78, 100]. In addition, these features are quite different from linear focusing of wave superpositions [17–21] and allow the experimental and observational distinction of both mechanisms.

RWs emerge when β_3 is large enough and their appearance is very rapid in a short range $0.8 \lesssim \beta_3/2.64 \times 10^{-42}\mathrm{s}^3\mathrm{m}^{-1} \lesssim 1$. Though, in chapter 6, we could analytically estimate a transition value of $\beta_3 \approx 0.9 \times (2.64 \times 10^{-42})\mathrm{s}^3\mathrm{m}^{-1}$ using stability arguments, the full analytical dependency of ϵ_{eff} on the other parameters remains unknown. We attempted to calculate the energy transfer analytically but, because of the non-linearity of the problem, standard perturbative approaches fail to give a solution [101].

We find that simulations of the gNLSE with $\beta_3 = 0$ but including an added Raman term also affirm the essential role of quasi-soliton collisions and are also well described by the cascade model. Unfortunately a quasi-soliton solution is not known for the complete gNLSE (all terms considered at the same time) [102, 103], therefore we could not verify the cascade model in the more general case. This front requires more analytical research which it is not an easy task given the intrinsic not integrability of the problem.

Up to now, we have used the term RW only loosely to denote high-energy quasi-solitons as shown in Figs. 3.4 and 3.2. Indeed, a strict definition of a RW is still an

open question and qualitative definitions such as *a pulse whose amplitude* (or energy or power) *is much higher than surrounding pulses* are common [5]. Our results now suggest, in agreement with recent work [5], a quantifiable operational definition at least for *normal* waves in optical fibers described by the gNLSE: a large amplitude wave is *not* a RW if it occurs as frequently as expected for the PDF at $\beta_3 = 0$ (cp. Fig. 3.2). We emphasize that both high spatial and temporal resolution are required to obtain reliable statistics for RWs in optical fibers.

We find that RWs are preceded by short periods of reduced wave amplitudes. This "calm before the storm" has been observed previously [15] in ocean and in optical multifilament RWs, but not yet in studies of optical fibers. We remark that we first noticed the effect in our cascade model, before investigating it in the gNLSE as well. This highlights the usefulness of the cascade model for qualitatively new insights into RW dynamics.

Last, we showed that a suitable dispersion engineering for NLSE even without TOD or Raman term could destabilize the solitons and lead eventually to the formation of RWs. Our numerical experiment indicates the energy transfer between two unstable bright solitons in the normal-dispersion regions of a fiber. We find that the width δ of the normal dispersion region is crucial for the process to occur, as well as the phase difference ϕ between the two solitons. Our experimental proposal can have fundamental implications in the field of soliton interaction and rogue wave generation [42, 90] and the device in Fig. 9.1 can be exploited for soliton amplification in optical fiber systems. We highlight that the device in Fig. 9.1 can be built in a real world laboratory and our predictions for the energy transfer (Fig. 9.3 (a)) can be verified experimentally. In this regard we finish quoting the physicist Richard Feynman [104]:

> "It doesn't matter how beautiful your theory is, it doesn't matter how smart you are. If it doesn't agree with experiment, it's wrong."

Bibliography

[1] J. M. Dudley, F. Dias, M. Erkintalo, and G. Genty, Instabilities, breathers and rogue waves in optics, Nature Photonics **8**(10), 755–764 (2014). 1, 19

[2] G. Genty, B. Kibler, J. Fatome, and C. Finot, Optical rogue waves: Physics and impact, Optical Fiber (2011). 2, 15

[3] J. Laurie, U. Bortolozzo, S. Nazarenko, and S. Residori, One-dimensional optical wave turbulence: Experiment and theory, Physics Reports **514**(4), 121–175 (may 2012).

[4] S. Nazarenko, *Wave Turbulence*, volume 825 of *Lecture Notes in Physics*, Springer Berlin Heidelberg, Berlin, Heidelberg, 2011.

[5] N. Akhmediev, B. Kibler, F. Baronio, M. Belić, W.-P. Zhong, Y. Zhang, W. Chang, J. M. Soto-Crespo, P. Vouzas, P. Grelu, C. Lecaplain, K. Hammani, S. Rica, A. Picozzi, M. Tlidi, K. Panajotov, A. Mussot, A. Bendahmane, P. Szriftgiser, G. Genty, J. Dudley, A. Kudlinski, A. Demircan, U. Morgner, S. Amiraranashvili, C. Bree, G. Steinmeyer, C. Masoller, N. G. R. Broderick, A. F. J. Runge, M. Erkintalo, S. Residori, U. Bortolozzo, F. T. Arecchi, S. Wabnitz, C. G. Tiofack, S. Coulibaly, and M. Taki, Roadmap on optical rogue waves and extreme events, Journal of Optics **18**(6), 063001 (2016). 2, 15, 21, 53, 73, 105

[6] N. Akhmediev, J. M. Dudley, D. R. Solli, and S. K. Turitsyn, Recent progress in investigating optical rogue waves, Journal of Optics **15**(6), 060201 (jun 2013). 1, 2, 15

[7] K. Hammani, C. Finot, J. M. Dudley, and G. Millot, Optical rogue-wave-like extreme value fluctuations in fiber Raman amplifiers, Optics Express **16**(21), 16467 (2008). 1, 19, 20, 67

[8] L. Draper, "Freak" ocean waves, Oceanus **10**, 13–15 (1964). 1, 19

[9] L. Draper, Severe wave conditions at sea, J. Inst. Navig. **24**, 273–277 (1971).

[10] J. Mallory, Abnormal waves in the south-east coast of South Africa, Int. Hydrog. Rev. **51**, 89–129 (1974). 1, 19

[11] R. El Koussaifi, A. Tikan, A. Toffoli, S. Randoux, P. Suret, and M. Onorato, Spontaneous emergence of rogue waves in partially coherent waves: A quantitative experimental comparison between hydrodynamics and optics, Physical Review E **97**(1), 012208 (jan 2018). 2, 19

[12] M. Onorato, *Rogue and Shock Waves in Nonlinear Dispersive Media*, volume 926 of *Lecture Notes in Physics*, Springer International Publishing, Cham, 2016.

[13] S. Residori, M. Onorato, U. Bortolozzo, and F. T. Arecchi, Rogue waves: a unique approach to multidisciplinary physics, Contemporary Physics **58**(1), 53–69 (jan 2017).

[14] M. Onorato, S. Residori, U. Bortolozzo, A. Montina, and F. Arecchi, Rogue waves and their generating mechanisms in different physical contexts, Physics Reports **528**(2), 47–89 (2013). 2, 19, 22

[15] S. Birkholz, C. Brée, A. Demircan, and G. Steinmeyer, Predictability of Rogue Events, Physical Review Letters **114**(21), 213901 (2015). 2, 20, 21, 67, 69, 70, 73, 105

[16] K. Hammani, B. Kibler, C. Finot, and A. Picozzi, Emergence of rogue waves from optical turbulence, Physics Letters A **374**(34), 3585–3589 (2010). 2

[17] M. Onorato, A. R. Osborne, M. Serio, and L. Cavaleri, Modulational instability and non-Gaussian statistics in experimental random water-wave trains, Physics of Fluids **17**(7), 078101 (2005). 2, 21, 104

[18] R. Höhmann, U. Kuhl, H.-J. Stöckmann, L. Kaplan, and E. J. Heller, Freak Waves in the Linear Regime: A Microwave Study, Phys. Rev. Lett. **104**, 093901 (2010). 21

[19] H. Degueldre, J. M. Jakob, T. Geisel, and R. Fleischmann, Random focusing of tsunami waves, Nature Physics **12** (2016).

[20] Mohammed F. Saleh, Claudio Conti and F. Biancalana, Anderson localisation and optical-event horizons in rogue-soliton generation, (2017).

[21] A. Safari, R. Fickler, M. J. Padgett, and R. W. Boyd, Generation of Caustics and Rogue Waves from Nonlinear Instability, Physical Review Letters **119**(20), 203901 (nov 2017). 2, 104

[22] V. Karpman and V. Solov'ev, A perturbational approach to the two-soliton systems, Physica D: Nonlinear Phenomena **3**(3), 487–502 (1981). 2, 15, 41, 45, 48, 85

[23] A. V. Buryak and N. N. Akhmediev, Internal friction between solitons in near-integrable systems, Phys. Rev. E **50**(4), 3126–3133 (1994).

[24] B. Frisquet, B. Kibler, and G. Millot, Collision of Akhmediev Breathers in Nonlinear Fiber Optics, Physical Review X **3**(4), 041032 (dec 2013).

[25] D. R. Martinez, M. M. M. Otero, M. L. A. Carrasco, and M. D. I. Castillo, Waveguide properties of the asymmetric collision between two bright spatial solitons in Kerr media., Optics express **20**(24), 27411–27418 (nov 2012). 2, 15, 45, 85

[26] G. P. Agrawal, *Nonlinear Fiber Optics*, Academic Press, Oxford UK, 2013. 5, 6, 7, 8, 10, 11, 13, 14, 15, 16, 17, 31, 35, 77, 78, 92

[27] F. M. Mitschke and L. F. Mollenauer, Discovery of the soliton self-frequency shift, Optics Letters **11**(10), 659 (1986). 11, 77

[28] N. Akhmediev and M. Karlsson, Cherenkov radiation emitted by solitons in optical fibers, Phys. Rev. A **51**(3), 2602–2607 (1995). 11, 30, 37, 40, 57

[29] F. DeMartini, C. H. Townes, T. K. Gustafson, and P. L. Kelley, Self-Steepening of Light Pulses, Physical Review **164**(2), 312–323 (1967). 11

[30] V. E. Zakharov and A. B. Shabat, Exact theory of two-dimensional self-focusing and one dimensional self-modulation of waves in nonlinear media, Sov. Phys. JETP **34**, 62–69 (1972). 11

[31] V. E. Zakharov, Studies in Applied Mathematics . 11

[32] M. Remoissenet, *Waves Called Solitons*, Springer, 1999. 13

[33] R. H. Mollenauer, L. F. Stolen and J. P. Gordon, Experimental Observation of Picosecond Pulse Narrowing and Solitons in Optical Fibers, Phys. Rev. Lett. **45**(1095) (1980). 15

[34] Y. Kivshar and G. Agrawal, *Optical Solitons*, Academic Press, 2003. 15

[35] R. R. Alfano, The Ultimate White Light, Scientific American **295**(6), 86–93 (2006). 15, 21, 30

[36] A. Hasegawa, Generation of a train of soliton pulses by induced modulational instability in optical fibers, Optics Letters **9**(7), 288 (1984). 15, 21, 30

[37] R. A. Fisher and W. K. Bischel, Numerical studies of the interplay between self-phase modulation and dispersion for intense plane-wave laser pulses, Journal of Applied Physics **46**(11), 4921–4934 (1975). 15

[38] W. H. Press, B. P. Flannery, S. A. Teukolsky, and W. T. Vetterling, *Numerical Recipes in C*, Cambridge University Press, Cambridge, 2nd edition, 1992. 55, 58

[39] W. H. Press, B. P. Flannery, S. A. Teukolsky, and W. T. Vetterling, *Numerical Recipes in FORTRAN*, Cambridge University Press, Cambridge, 2nd edition, 1992. 15

[40] M. Eberhard, Massively Parallel Optical Communication System Simulator, https://github.com/Marc-Eberhard/MPOCSS. 16, 28, 30

[41] T. R. Taha and M. I. Ablowitz, Analytical and numerical aspects of certain nonlinear evolution equations. II. Numerical, nonlinear Schrödinger equation, Journal of Computational Physics **55**(2), 203–230 (1984). 17

[42] D. R. Solli, C. Ropers, P. Koonath, and B. Jalali, Optical rogue waves, Nature **450**(7172), 1054–1057 (2007). 19, 20, 21, 22, 24, 25, 105

[43] M. Taki, A. Mussot, A. Kudlinski, E. Louvergneaux, M. Kolobov, and M. Douay, Third-order dispersion for generating optical rogue solitons, Physics Letters A **374**(4), 691–695 (2010). 19, 23, 24, 25, 27

[44] S. Perkins, Dashing Rogues, Science News **170**(21), 328 (2006). 19

[45] M. Erkintalo, Rogue waves: Predicting the unpredictable?, Nature Photonics **9**(9), 560–562 (2015). 19

[46] M. Hopkin, Sea snapshots will map frequency of freak waves., Nature **430**(6999), 492 (2004). 19

[47] A. Chabchoub, T. Waseda, B. Kibler, and N. Akhmediev, Experiments on higher-order and degenerate Akhmediev breather-type rogue water waves, Journal of Ocean Engineering and Marine Energy **3**(4), 385–394 (nov 2017).

[48] A. N. Ganshin, V. B. Efimov, G. V. Kolmakov, L. P. Mezhov-Deglin, and P. V. E. McClintock, Energy cascades and rogue waves in superfluid 4He, Journal of Physics: Conference Series **150**(3), 32056 (2009).

[49] A. Toffoli, D. Proment, H. Salman, J. Monbaliu, F. Frascoli, M. Dafilis, E. Stramignoni, R. Forza, M. Manfrin, and M. Onorato, Wind Generated Rogue Waves in an Annular Wave Flume, Physical Review Letters **118**(14), 144503 (apr 2017). 19

[50] C. Kharif and E. Pelinovsky, Physical mechanisms of the rogue wave phenomenon, European Journal of Mechanics - B/Fluids **22**(6), 603 – 634 (2003). 19

[51] M. Onorato, A. R. Osborne, M. Serio, L. Cavaleri, C. Brandini, and C. T. Stansberg, Observation of strongly non-Gaussian statistics for random sea surface gravity waves in wave flume experiments., Phys. Rev. E **70**(6 Pt 2), 067302 (2004). 19

[52] T. A. A. Adcock, P. H. Taylor, and S. Draper, Nonlinear dynamics of wave-groups in random seas: unexpected walls of water in the open ocean, Proceedings of the Royal

Society A: Mathematical, Physical and Engineering Science **471**(2184), 20150660 (2015). 19, 21

[53] J. M. Dudley, F. Dias, M. Erkintalo, and G. Genty, Instabilities, breathers and rogue waves in optics, Nature Publishing Group **8**(10), 755–764 (2014). 19

[54] A. Chabchoub, N. Hoffmann, M. Onorato, G. Genty, J. M. Dudley, and N. Akhmediev, Hydrodynamic supercontinuum., Phys. Rev. Lett. **111**(5), 054104 (2013). 19

[55] D. R. Solli, C. Ropers, and B. Jalali, Active control of rogue waves for stimulated supercontinuum generation., Phys. Rev. Lett. **101**(23), 233902 (2008). 19

[56] M. Erkintalo, G. Genty, and J. M. Dudley, Rogue-wave-like characteristics in femtosecond supercontinuum generation, Optics Letters **34**(16), 2468 (2009).

[57] B. Kibler, C. Finot, and J. M. Dudley, Soliton and rogue wave statistics in supercontinuum generation in photonic crystal fibre with two zero dispersion wavelengths, The European Physical Journal Special Topics **173**(1), 289–295 (2009).

[58] K. Tai, A. Hasegawa, and A. Tomita, Observation of modulational instability in optical fibers., Phys. Rev. Lett. **56**(2), 135–138 (1986).

[59] F. Baronio, B. Frisquet, S. Chen, G. Millot, S. Wabnitz, and B. Kibler, Observation of a group of dark rogue waves in a telecommunication optical fiber, Physical Review A **97**(1), 013852 (jan 2018).

[60] J. Liu, Weak-light rogue waves, breathers, and their active control in a cold atomic gas via electromagnetically induced transparency, Physical Review A **93**(6), 063836 (2016).

[61] P. Suret, R. E. Koussaifi, A. Tikan, C. Evain, S. Randoux, C. Szwaj, and S. Bielawski, Single-shot observation of optical rogue waves in integrable turbulence using time microscopy, Nature Communications **7** (2016). 19

[62] A. Armaroli, C. Conti, and F. Biancalana, Rogue solitons in optical fibers: a dynamical process in a complex energy landscape?, Optica **2**(5), 497 (2015). 19, 27, 91, 104

[63] C. Brée, G. Steinmeyer, I. Babushkin, U. Morgner, and A. Demircan, Controlling formation and suppression of fiber-optical rogue waves, Optics Letters **41**(15), 3515 (2016).

[64] A. Demircan, S. Amiranashvili, C. Br?e, C. Mahnke, F. Mitschke, and G. Steinmeyer, Rogue wave formation by accelerated solitons at an optical event horizon, Applied Physics B **115**(3), 343–354 (2014). 73, 91

[65] G. Genty, C. de Sterke, O. Bang, F. Dias, N. Akhmediev, and J. Dudley, Collisions and turbulence in optical rogue wave formation, Physics Letters A **374**(7), 989–996 (2010). 27, 104

[66] V. V. Voronovich, V. I. Shrira, and G. Thomas, Can bottom friction suppress 'freak wave' formation?, Journal of Fluid Mechanics **604**, 263–296 (2008).

[67] N. Akhmediev, A. Ankiewicz, and M. Taki, Waves that appear from nowhere and disappear without a trace, Physics Letters A **373**(6), 675–678 (2009).

[68] N. Akhmediev, J. M. Soto-Crespo, and A. Ankiewicz, Extreme waves that appear from nowhere: on the nature of rogue waves, Physics Letters A **373**(25), 2137–2145 (2009).

[69] J. M. Dudley, G. Genty, and B. J. Eggleton, Harnessing and control of optical rogue waves in supercontinuum generation, Optics Express **16**(6), 3644 (mar 2008). 19

[70] S. Randoux, P. Walczak, M. Onorato, and P. Suret, Intermittency in integrable turbulence., Phys. Rev. Lett. **113**(11), 113902 (2014). 20

[71] P. Walczak, S. Randoux, and P. Suret, Optical rogue waves in integrable turbulence., Phys. Rev. Lett. **114**(14), 143903 (2015). 20

[72] J. Kasparian, P. Béjot, J.-P. Wolf, and J. M. Dudley, Optical rogue wave statistics in laser filamentation, Optics Express **17**(14), 12070 (2009). 20

[73] A. Montina, U. Bortolozzo, S. Residori, and F. T. Arecchi, Non-Gaussian statistics and extreme waves in a nonlinear optical cavity., Phys. Rev. Lett. **103**(17), 173901 (2009). 20

[74] C. Bonatto, M. Feyereisen, S. Barland, M. Giudici, C. Masoller, J. R. R. Leite, and J. R. Tredicce, Deterministic optical rogue waves., Phys. Rev. Lett. **107**(5), 053901 (2011). 20

[75] C. Lecaplain, P. Grelu, J. M. Soto-Crespo, and N. Akhmediev, Dissipative rogue waves generated by chaotic pulse bunching in a mode-locked laser., Phys. Rev. Lett. **108**(23), 233901 (2012). 20

[76] J. Peng, N. Tarasov, S. Sugavanam, and D. Churkin, Rogue waves generation via nonlinear soliton collision in multiple-soliton state of a mode-locked fiber laser, Optics Express **24**(19), 21256 (sep 2016). 20

[77] S. Randoux and P. Suret, Experimental evidence of extreme value statistics in Raman fiber lasers., Optics letters **37**(4), 500–2 (2012). 20

111

[78] M. Eberhard, A. Savojardo, A. Maruta, and R. A. Römer, Rogue wave generation by inelastic quasi-soliton collisions in optical fibres, Optics Express **25**(23), 28086 (2017). 21, 91, 104

[79] N. Akhmediev and E. Pelinovsky, Editorial – Introductory remarks on "Discussion & Debate: Rogue Waves – Towards a Unifying Concept?", The European Physical Journal Special Topics **185**(1), 1–4 (2010). 21, 53

[80] V. Ruban, Y. Kodama, M. Ruderman, J. Dudley, R. Grimshaw, P. V. E. McClintock, M. Onorato, C. Kharif, E. Pelinovsky, T. Soomere, G. Lindgren, N. Akhmediev, A. Slunyaev, D. Solli, C. Ropers, B. Jalali, F. Dias, and A. Osborne, Rogue waves – towards a unifying concept?: Discussions and debates, The European Physical Journal Special Topics **185**(1), 5–15 (2010). 21, 53

[81] B. Kibler, J. Fatome, C. Finot, G. Millot, F. Dias, G. Genty, N. Akhmediev, and J. M. Dudley, The Peregrine soliton in nonlinear fibre optics, Nature Physics **6**(10), 790–795 (2010). 21

[82] A. Chabchoub, N. P. Hoffmann, and N. Akhmediev, Rogue wave observation in a water wave tank., Phys. Rev. Lett. **106**(20), 204502 (2011).

[83] B. Kibler, J. Fatome, C. Finot, G. Millot, G. Genty, B. Wetzel, N. Akhmediev, F. Dias, and J. M. Dudley, Observation of Kuznetsov-Ma soliton dynamics in optical fibre., Scientific reports **2**, 463 (2012). 21

[84] J. Wang, Q. Ma, S. Yan, and A. Chabchoub, Breather Rogue Waves in Random Seas, Physical Review Applied **9**(1), 014016 (jan 2018). 22

[85] F. J. Harris, *Time domain signal processing with the DFT*, Academic Press, San Diego USA, 1987. 28

[86] M. Miyagi and S. Nishida, Pulse spreading in a single-mode fiber due to third-order dispersion, Applied Optics **18**(5), 678 (1979). 35

[87] Z. Chen, A. J. Taylor, and A. Efimov, Soliton dynamics in non-uniform fiber tapers: analytical description through an improved moment method, Journal of the Optical Society of America B **27**(5), 1022 (2010). 35, 78

[88] J. Santhanam and G. P. Agrawal, Raman-induced spectral shifts in optical fibers: general theory based on the moment method, Optics Communications **222**(1-6), 413–420 (2003). 35, 78

[89] Y. Nagashima, *Elementary Particle Physics*, volume 1, Wiley-Vch, Weinheim, 2010. 48

[90] N. Akhmediev, J. M. Soto-Crespo, and A. Ankiewicz, Could rogue waves be used as efficient weapons against enemy ships?, The European Physical Journal Special Topics **185**(1), 259–266 (2010). 53, 91, 96, 105

[91] G. Weerasekara, A. Tokunaga, H. Terauchi, M. Eberhard, and A. Maruta, Soliton's eigenvalue based analysis on the generation mechanism of rogue wave phenomenon in optical fibers exhibiting weak third order dispersion, Optics Express **23**(1), 143 (2015). 53

[92] F. Luan, D. V. Skryabin, A. V. Yulin, and J. C. Knight, Energy exchange between colliding solitons in photonic crystal fibers, Optics Express **14**(21), 9844 (2006). 91, 96

[93] A. Mussot, A. Kudlinski, M. Kolobov, E. Louvergneaux, M. Douay, and M. Taki, Observation of extreme temporal events in CW-pumped supercontinuum., Optics express **17**(19), 17010–5 (2009). 104

[94] A. Slunyaev and E. Pelinovsky, Role of Multiple Soliton Interactions in the Generation of Rogue Waves: The Modified Korteweg–de Vries Framework, Phys. Rev. Lett. **117**(21), 214501 (2016).

[95] Y.-H. Sun, Soliton synchronization in the focusing nonlinear Schrödinger equation, Physical Review E **93**(5), 052222 (2016).

[96] V. Zakharov, A. Pushkarev, V. Shvets, and V. Yan'kov, Soliton turbulence, Pis'ma v Zhurnal Eksperimental'noi i Teoreticheskoi Fiziki **48**(2), 79–82 (1988).

[97] U. Bortolozzo, J. Laurie, S. Nazarenko, and S. Residori, Optical wave turbulence and the condensation of light, Journal of the Optical Society of America B **26**(12), 2280 (2009).

[98] A. Picozzi, J. Garnier, T. Hansson, P. Suret, S. Randoux, G. Millot, and D. Christodoulides, Optical wave turbulence, Physics Reports **542**(1), 1–132 (2014).

[99] A. Demircan, S. Amiranashvili, C. Brée, C. Mahnke, F. Mitschke, and G. Steinmeyer, Rogue events in the group velocity horizon, Scientific Reports **2** (2012). 104

[100] M. Eberhard, A. Savojardo, A. Maruta, and R. A. Römer, Inelastic quasi-soliton collision driven Rogue Wave generation cascade mechanism in optical fibres, http://dx.doi.org/10.17036/5067df69-bf43-4bea-a5ff-f0792001d573 (2016). 104

[101] A. Peleg, M. Chertkov, and I. Gabitov, Inelastic interchannel collisions of pulses in optical fibers in the presence of third-order dispersion, J. Opt. Soc. Am. B **21**(1) (2004). 104

[102] A. Ankiewicz, J. M. Soto-Crespo, M. A. Chowdhury, and N. Akhmediev, Rogue waves in optical fibers in presence of third-order dispersion, self-steepening, and self-frequency shift, Journal of the Optical Society of America B **30**(1), 87–94 (2013). 104

[103] U. Bandelow and N. Akhmediev, Persistence of rogue waves in extended nonlinear Schrödinger equations: Integrable Sasa–Satsuma case, Physics Letters A **376**(18), 1558–1561 (2012). 104

[104] R. P. Feynman, *The Character of Physical Law*, Penguin Press Science, 1965. 105